1-1-2009

An interferometric study of free convection in a window with a heated between-panes blind

Fabio Almeida
ryerson

AN INTERFEROMETRIC STUDY OF FREE CONVECTION IN A WINDOW WITH A HEATED BETWEEN-PANES BLIND

By

Fabio Almeida

B.Eng., Ryerson University, 2006

A thesis

Presented to Ryerson University

In partial fulfillment of the

Requirements for the degree of

Master of Applied Science

in the Program of

Mechanical Engineering

Toronto, Ontario, Canada, 2008

Author Declaration

I hereby declare that I am the sole author of this thesis or dissertation.

I authorize Ryerson University to lend this thesis or dissertation to other institutions or individuals for the purpose of scholarly research.

I further authorize Ryerson University to reproduce this thesis or dissertation by photocopying or by other means, in total or in part, at the request of other institutions or individuals for the purpose of scholarly research.

Borrower

Ryerson University requires the signatures of all persons using or photocopying this thesis. Please sign below, and give address and date.

Abstract

AN INTERFEROMETRIC STUDY OF FREE CONVECTION IN A WINDOW WITH A HEATED BETWEEN-PANES BLIND

Fabio Almeida

Master of Applied Science

2009

Mechanical Engineering

Ryerson University

An experimental study has been conducted to examine free convection in a window with an enclosed aluminum Venetian blind. The unique feature of this experiment was that the blind slats were heated electrically to simulate absorbed solar radiation. Centre-glass convective heat transfer measurements and temperature field visualization were obtained using a laser Mach-Zehnder interferometer. Measurements were made for three plate (glazing) spacings, three blind slat angles, three blind heat fluxes, and two plate temperature differences. It was found that a recently proposed simplified model, called the Reduced Slat Length (RSL) model, closely predicted the experimental results when the flow appeared to be laminar and steady. Under these conditions, the temperature field and lateral heat transfer was dominated by conduction. Under some conditions, evidence of highly unsteady/turbulent flow was observed. As expected, the RSL model performed poorly under these conditions.

Acknowledgements

The author would like to acknowledge Dr. D. Naylor for his guidance and advice through the duration of this research and during the writing of this thesis.

The author would also like to thank the Engineering Support staff, especially Alan Machin and Joseph Amenkrah, for their time and effort to help build the experimental apparatus and for their willingness to teach their knowledge throughout the duration of this project.

The author is most grateful to Dr. M. Collins and Dr. J. Wright of the University of Waterloo for their consultation and for making key measurements of the apparatus. And the collaboration of Dr. Oosthuizen at Queens University was greatly appreciated.

Finally, the author would like to acknowledge the support of the Solar Buildings Research Network.

Table of Contents

List of Tables

List of Figures

Nomenclature

A	enclosure aspect ratio
A_{pf}	projected fenestration area
c_p	specific heat
d	fringe spacing
E_t	incident total irradiance
G	Gladstone-Dale constant
Gr_{crit}	Critical Grashof number
g	gravity
H	enclosure height
k	thermal conductivity
n^*	subcavity fraction width
N	inward-flowing fraction of absorbed radiation
Nu	Nusselt number
P	absolute pressure
Pr	Prandtl number
q''	average heat flux
q_s	total solar heat gain
Q	instantaneous heat flow
R	gas constant of air
Ra	Rayleigh number
S	slat pitch
T	temperature
U	U-factor
w	error quantity
W	width
x, y	cartesian coordinates
Z	length of model in light beam direction

Greek Symbols

β	volumetric expansion coefficient
δ	error difference
Δ	change/difference
ε	fringe shift order
ε_P	paint emissivity
ε_S	absorbed solar radiation
λ	vacuum wavelength of laser
μ	dynamic viscosity
ρ	density
τ	transmitted solar radiation
ϕ	blind angle
Ψ	fringe misalignment

Subscipts

B	blind slat
C	cold wall
H	hot wall
in	indoor
G	full enclosure
out	outdoor
s	wall surface
REF	reference
M	mean

Superscripts

$'$	modified subcavity

Abbreviations

ASHRAE American Society of Heating, Refrigerating and Air-Conditioning Engineers

CSA Canadian Standards Association

IGU insulating glazing unit

MZI Mach-Zehnder Interferometer

NFRC National Fenestration Rating Council

SHGC solar heat gain coefficient

Chapter 1: Introduction

1.1 Introduction

Due to higher energy costs and an increased awareness of our environment, there has been an increased focus to produce energy efficient fenestration systems. Fenestration systems, such as windows, can have a substantial impact on the heating and cooling costs of a building through heat loss and gain to the outdoors. Therefore, the understanding and improvement of double glazed window insulating capabilities is an area of great interest.

It is common to describe the thermal performance of window systems with the overall heat transfer coefficient referred to as the U-factor. The U-factor is usually divided into the heat transfer contributions from the center glass region (cg), edge glass region (eg), and the frame (f) of the window. It is defined as the area-weighted average of each component (ASHRAE 2005):

$$U = \frac{U_{cg}A_{cg} + U_{eg}A_{eg} + U_f A_f}{A_{pf}} \tag{1.1}$$

The subscript 'pf' is the fenestration unit opening in the wall. With the U-factor defined, the instantaneous energy flow through a window system is defined as:

$$Q = UA_{pf}(T_{out} - T_{in}) + SHGC(A_{pf})E_t \tag{1.2}$$

where:

Q = instantaneous heat flow

U = U-factor

T_{out} = outdoor temperature

T_{in} = indoor temperature

A_{pf} = projected fenestration area

SHGC = solar heat gain coefficient

E_t = incident total irradiance

Fenestration usually consists of glazing, framing, and shading devices, which can all have an impact on the overall U-factor. Glazing units can have multiple panes of glass which create cavities of insulating gas referred to as an insulating glazing unit (IGU). The fill gas is sometimes air, but argon and krypton gas can be used to provide better thermal insulation. The IGU can have low emissivity (low-e) coatings to improve energy efficiency and thermal comfort. Window frames can create a thermal bridge to the outside weather through conduction and, hence, a thermal break (nonmetal component in the frame) is often used to negate this effect. Shading devices include blinds, overhangs, draperies, screens, and shutters. Shading devices can greatly affect the thermal performance of the window, thermal comfort, and daylighting by controlling the amount of solar radiation entering the room and acting as another insulating layer in the IGU. Shading devices represent a difficult heat transfer problem due to their complex geometries. Therefore, there is an interest in determining their affect on window thermal performance.

Window thermal analysis programs are widely used to aid in the design and optimization of windows. The Canadian Standards Association (CSA) uses the program VISION (Wright 1992) and the National Fenestration Rating Council (NFRC) uses WINDOW (Finlayson et al. 1993) for the rating of windows. These programs have been developed to perform a one-

dimensional heat transfer analysis to determine the U-value and solar heat gain coefficient (SHGC) for a variety of windows. These programs take inputs such as the number of glazings, weather conditions, and materials (glazing type, fill gases, etc)

However, these programs do not take into consideration the effect of shading systems such as Venetian blinds. While shading devices can greatly affect window performance, there are currently no correlations available to predict their effect. Thus, it is the purpose of many researchers to understand this phenomenon in order to develop simplified correlations to use in building simulation software.

1.2 Problem Definition

The current research will focus on the effect of Venetian blinds, enclosed in a double glazed window, on the heat transfer rates through a window. The problem consists of convection in a tall vertical cavity with convection and radiation between the enclosure surfaces and blinds. The double glazed windows will be treated as isothermal vertical plates, and the blinds will be electrically heated to simulate the effect of solar heat gain. Laser interferometry will be used to obtain the temperature field and to obtain the surface convective heat transfer rates.

Figure 1.1 shows the geometry of the problem domain. The isothermal plates are held at a distant 'W_G' apart and held at constant temperatures 'T_C' and 'T_H' denoting cold wall and hot wall, respectively. The blinds of width 'W_B' are held at angle 'ϕ' to the horizontal with heat flux 'q''_B' on the slat and temperature 'T_B'. The blinds are spaced a distance 'S' from each other.

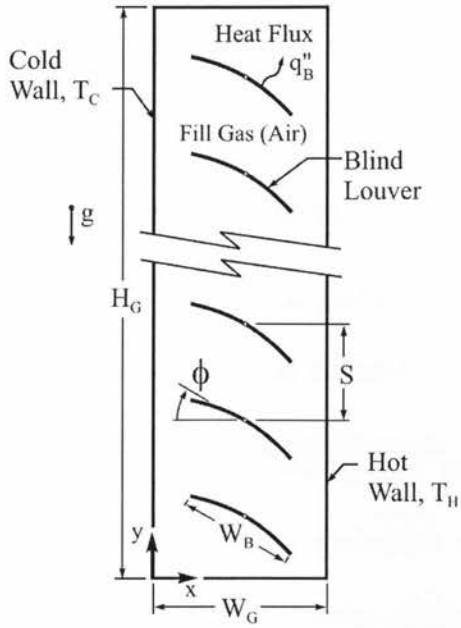

Figure 1.1: Problem geometry

1.3 Free Convection in Vertical Cavity

Most residential windows now use multiple panes of glass in order to reduce the heat transfer rate. Since the heat transfer rate can vary depending on geometry and material of the window, it is important to understand the physical properties of such geometries.

A double glazed window is essentially a vertical cavity with an enclosed fluid. In a typical empty cavity, there are two vertical walls at different temperatures, with the top and bottom walls being almost adiabatic. On the hot wall, there is upward buoyancy driven flow. On the cold wall, the flow is downward. This creates circulation in the cavity, which affects the heat transfer rates. This typical problem definition is idealized and it cannot duplicate the complexities of real world windows, which can have temperature variations along the vertical

walls and instability in the circulating fluid. Due to these complexities, many empirical correlations have been developed for different flow conditions.

1.4 Empty Cavity Flow Behavior

Batchelor (1954) was one of the first to break down empty cavity flow into different flow regimes. He found that the flow conditions can be discussed in terms of the average Nusselt number, (Nu), Rayleigh number (Ra), Prandtl number (Pr), and aspect ratio (A), which are defined as follows:

$$Nu = q'' \frac{W_G}{k \cdot \Delta T} = q'' \frac{W_G}{k(T_H - T_C)} \tag{1.3}$$

$$Ra = \frac{\rho^2 {W_G}^3 g c_P (T_H - T_C)\beta}{\mu k} \tag{1.4}$$

$$Pr = \frac{\mu c_P}{k} \tag{1.5}$$

$$A = {}^{H}/_{W_G} \tag{1.6}$$

A study by Wright et al. (2006) looked at the natural convection in an air filled tall vertical cavity. Their objective was to determine the flow patterns of air for a large range of Rayleigh numbers in order to aid in numerical simulation. The aspect ratio was held constant and the Rayleigh number was varied by adjusting the temperature difference between the cold

wall and the hot wall. Smoke flow visualization and interferometry were used to obtain the flow conditions.

The flow was dominated by conduction at Ra < $6x10^3$ corresponding to a small temperature difference. At this Rayleigh number, the flow was laminar and steady with weak buoyancy driven flow creating a weak unicellular flow along the outer perimeter of the enclosure.

Formation of co-rotating cells appeared as a secondary flow pattern at the core of the enclosure at $7x10^3$ < Ra < $9x10^3$ with the primary outer flow moving closer to the perimeter. This secondary flow became unstable at approximately Ra = 10^4. At this Ra number, the cells started to interact with other cells and the outer primary flow.

Turbulent flow in the core occurred at Ra > $1.4x10^4$, with 3D behavior becoming apparent. There was a mix of co-rotating and counter-rotating cells, with some cells merging. The interferometry photographs indicated that most of the temperature drop occurs in the boundary layer, while the core flow is well mixed, giving a relatively uniform temperature. While the core area exhibited unsteadiness, the boundary layer region stayed stable and became thinner as Raleigh number increased.

Korpela et al. (1982) determined that, for a tall vertical cavity, the onset of these secondary cells can be determined from the critical Grashof number defined as,

$$Gr_{crit} = 8000\left(1 + \frac{5}{A}\right) \tag{1.7}$$

Where,

$$A = {}^{H}/_{W_G} \tag{1.8}$$

Below this number, the flow is unicellular, and above this number, a stable co-rotating cell pattern occurs. It has been shown experimentally by Jin (2000) that the transition to unsteady flow occurs slightly higher than the theoretically predicted critical Grashof number (Eq. 1.7), effectively allowing the use of the critical Grashof number as a condition for steady flow in an empty enclosure.

One of the reasons for understanding when the flow is steady and unsteady is to aid in the numerical analysis of such problems. Lee et al. (1983) performed a numerical study to analyze the behavior of multicellular flow, based on the experimental work of Batchelor (1954), Eckert & Carlson (1961), Elder (1965), and Gill (1966); however, their work was limited to 2D laminar flows. Chait and Korpela (1989) performed a numerical study of 3D multicellular flow.

Many correlations have been developed for empty cavity flows with isothermal vertical walls, e.g., Ramanathan and Kumar (1991), Shewen et al. (1996) and ElSherbiny et al. (1982). One of the more recent correlations was developed by Wright (1996) and was designed specifically for determining the convective heat transfer in the center glass region of double-pane windows:

$$Nu = 0.0673838Ra^{1/3} \qquad Ra > 5 \times 10^4 \qquad (1.9)$$

$$Nu = 0.028154Ra^{0.4134} \qquad 10^4 < Ra < 5 \times 10^4 \qquad (1.10)$$

$$Nu = 1 + 1.75967 \times 10^{-10}Ra^{2.2984755} \qquad Ra \leq 10^4 \qquad (1.11)$$

1.5 Radiation Considerations

In fenestration systems, solar radiation (shortwave radiation) gets turned into heat (long-wave radiation) by the absorbing materials such as window glazings and blind slats. In order to understand the effect of solar radiation it is common to define a solar heat gain coefficient (SHGC). Let us consider a single pane of glass exposed to sunlight. It can be shown that the total solar heat gain (q_S) can be expressed as follows (ASHRAE 2005):

$$q_S = E_t(\tau + N\varepsilon_S) \tag{1.12}$$

where:

E_t = incident solar irradiance

τ = transmitted solar radiation

N = inward-flowing fraction of absorbed radiation

ε_S = absorbed solar radiation.

The term '$\tau + N\varepsilon_S$' is the fraction of incident irradiance that becomes heat and is called the solar heat gain coefficient (SHGC). The variables 'τ' and 'ε_S' are spectral averages but are dependent on incidence angle. While the SHGC can be calculated, an assumed value from the literature will be used in this research.

1.6 Venetian Blind Studies (Literature Review)

1.6.1 Indoor Adjacent Blind Studies

One of the first studies to look at the interaction between window and blinds was Machin et al. (1998). This study looked at the laminar free convection heat transfer between an isothermal plate and aluminum blinds. This was an experimental study looking at the interaction between a single glazing and an interior Venetian blind. The vertical plate was electrically heated to give uniform temperature distribution to simulate the outdoor temperature. Interferometric photographs were taken for each case and used to determine the local Nusselt number. Machin et al. (1998) found that the presence of the blind affects the temperature field and local heat transfer rates. There was a strong periodic variation in local Nusselt number along the vertical wall corresponding to the location of the blind. Stable laminar eddies between the blinds were present for slat angles 0° and 45°. However, for -45°, turbulent time depended eddies were observed. This study did not consider the effect of the 'day time' condition where incident solar radiation is considered.

An experimental study of the interaction of a heated blind and a window glazing was done by Naylor et al. (2000). A set of blinds was electrically heated to simulate the heat absorption from solar radiation and was placed adjacent to an isothermal plate. The experiment was done for a variety of blind angles and heat flux into the blind. Flow field visualization was obtained using a sheet of laser light, and temperature field visualization was obtained from interferometry. It was found that the blind heat flux has a strong effect on the local and average

heat transfer rates. There were periodic variations in the heat transfer rates similar to Machin et al. (1998). The heat transfer rate from the blind to the window decreased as the blind flux increased. Also, the heat flux from the blind added to the unsteadiness for some scenarios. Duarte et al. (2001) did a similar study and also examined the effect of blind to plate spacing. The strength of the periodic variations of Nusselt number was greatly affected by the spacing. Duarte et al. (2001) concluded that spacing of the blind to the window glazing has a substantial impact on the convection at the indoor glazing and that this effect can be determined by properly taking into consideration the incident solar heat flux.

A coupled convection, conduction, and radiation numerical model was solved by Phillips et al. (2001). This study looked at night time conditions in order to simulate the work done by Machin et al. (1998). Numerical analysis used the 2D continuity, momentum, and energy equations solved for steady laminar flow with a grey diffuse radiation model. Boundary conditions were set to match that of the experimental work done by Machin et al. (1998). The numerical model matched the experimental work. An extension of this work was done by Shahid et al. (2005) where they looked at the thermal performance of a single and double glazed window. Numerical simulations were performed for conditions identical to Machin et al. (1998) and Phillips et al. (2001). The solution was validated against the experimental work of convection in a tall vertical cavity (ElSherbiny et al. (1982)) and conjugate heat transfer from a vertical plate to adjacent aluminum blinds (Machin et al. (1998), Phillips et al. (2001)).

Collins et al. (2002a) did a similar study to Phillips et al. (2001), but on a larger scale using seventeen louvered blinds. This numerical solution was validated with experimental results for the same geometry and conditions (Collins et al. (2002b)). The numerical model solved the governing equations for steady laminar flow. It was found that, for the center glass region, the

numerical model is in agreement with the experimental results. However, for certain conditions near the top regions of the blind assembly, there was disagreement in the convective heat flux. It was hypothesized that, under these conditions, a boundary layer was allowed to grow and affected the heat transfer rates at the top, which the numerical model did not take into consideration. In a later paper using the same model, Collins (2004) decoupled the radiation and convective heat transfer rates and performed the analysis on a larger range of Rayleigh numbers. Limited results were found due to convergence problems. It was hypothesized, that due to the high Ra numbers used in the numerical model, the flow was turbulent and/or unsteady; as such, the solution diverged because of the model assumptions.

From these studies, some simplified models and correlations have been developed. Fang (2000) developed a correlation for predicting the U-factor from experimental work for high-reflectivity Venetian blinds in single and double pane window configurations. Collins (2004) developed correlations to determine the solar heat gain and thermal gain of an interior Venetian blind. A simplified method for determining the effect of a louvered blind on the center glass U value was performed by Naylor and Collins (2005). A more detailed overview of the effect of shading devices on the heat transfer from a window can be found in Oosthuizen et al. (2005).

1.6.2 Between Pane Venetian Blind Studies

One of the earliest studies of between-pane Venetian blinds was the theoretical work of Rheault and Bilgen (1989). It was found that an automated blind system can reduce the energy loads by 36 percent for winter conditions and 47 percent for summer condition over a double pane window. In another early study, Garnet et al. (1995) used a guarded-heater plate apparatus

to measure the center-glass U-values of the window at a range of blind angles. This study did not look at the solar heat gain of the blind. It was found that, in some cases, the presence of the blinds reduced the thermal resistance of the window in comparison to the no-blind case. The conduction through the aluminum blind created a 'thermal bridge' which conducted heat through the cavity. However, for most of the cases, there was an improvement in the window performance, and an unexplained 'hump' in the center-glass U-values was found at the -60° blind angle case. The work of Garnet et al. (1995) was extended by Huang et al. (2006) to include the affects of plate spacing and low-e coatings. The findings of Huang et al. (2006) matched with the Garnet et al. (1995) study, including the 'hump' in the center-glass U-value.

A numerical study by Avedissian and Naylor (2007) was done to match the conditions of Garnet et al. (1995) and Huang et al. (2006). However, the numerical work was unable to capture the irregularity in the center-glass U-value as found in previous research. A simplified one dimensional model to reproduce the Garnet et al (1995) experimental work was developed by Yahoda and Wright (2004). The one-dimensional model treated the Venetian blind layer as a homogeneous layer with 'effective' optical properties in a series of glazing layers. The simplified model agreed with the Garnet et al. (1995) results to within 10%. Collins and Wright (2006) developed a new method to determine the center-glass U-value, SHGC, and radiative heat transfer coefficient by treating the shading layer as a diathermanous layer.

A numerical model of the Garnet el al. (1995) window experiment was performed by Naylor and Collins (2005). The conjugate convection, conduction, and radiation heat transfer was solved for steady, laminar flow with no solar irradiation of the window with 49 blinds. While the numerical results agreed closely with the Garnet et al (1995) experiment, there was some concern about the stability of the flow. Based on the predicted stream function contours, it

was shown that the presence of the blinds greatly inhibits the free convection flow. From the Grashof number, it was determined that the flow was well into the steady domain, if one assumes the presence of the blind effectively divides the empty cavity into two enclosures. However, it is a point of interest to determine under what conditions unsteady flow occur.

A recent experimental study of between-pane Venetian blinds was done by Naylor and Lai (2007). The study used seventeen unheated blinds and interferometric measurements were taken at various blind angles and Rayleigh numbers corresponding to different wall spacings. Local and average heat transfer rates and temperature field measurements were taken. The blinds were found to greatly affect the convective heat transfer within the enclosure. In the horizontal position, the aluminum blinds acted like a 'thermal bridge' by conducting heat through the enclosure, effectively increasing the heat transfer rate: whereas, in the closed position, the blinds divided the enclosure in two sections, which resulted in a reduction in the heat transfer rate. These results were used to validate the numerical model by Avedissian and Naylor (2007). They performed a 2D steady numerical simulation of free convection in a tall vertical enclosure with an internal louvered blind for night time conditions using the same parameters as Naylor et al. (2006). There was close agreement for the fully open position but the 45° position showed poor agreement with the local Nusselt number. It is hypothesized that there may be unsteadiness in the flow, even though unsteadiness was not evident in the temperature field. This is possibly due to the beam averaging effect of interferometry, which might mask small fluctuations in the temperature field. Based on the Avedissian and Naylor's (2006) results, an empirical correlation has been developed by Naylor et al. (2007).

1.7 The RSL Model

In the present study, where possible, comparisons have been made with the RSL model of Wright et al. (2008). The RSL model treats the between-the-pane Venetian blind geometry as two adjacent empty cavities with the middle wall retaining the blind temperature. Each cavity is assigned an effective subcavity width W' defined as follows:

$$W' = \frac{W_G - n^* W_B \cos\phi}{2} \tag{1.13}$$

where n* is a fraction that is determined empirically. For the present analysis, n*=0.7 was used, as recommended by Collins et al. (2008). With the subcavity width determined, the Nusselt number for that cavity was found using the correlation of Shewen et al. (1996):

$$Nu' = \left[1 + \left(\frac{0.0665 Ra^{1/3}}{1 + \left({}^{9000}/_{Ra}\right)^{1.4}}\right)^2\right]^{1/2} \tag{1.14}$$

where the subcavity Rayleigh number is defined as:

$$Ra' = \frac{g\beta\Delta T W'^3 \rho^2 c_P}{\mu k} \tag{1.15}$$

In the current study, the convective heat flux predicted by the RSL model is calculated using the measured blind temperature. An energy balance is not performed. The ΔT in equation

1.15 is measured between the blind temperature and the wall. The Nusselt number correlation applies to aspect ratios of $A \geq 40$.

1.8 Scope of Research

There is a demand to determine the behavior and effect of shading devices on the thermal performance of windows in order to have more accurate fenestration analysis programs in the future. There are many varieties of shading devices, but the Venetian blind is one of the most common and effective. Due to their aesthetics, potential for automation, and enhanced thermal performance, the between-pane Venetian blind is of major interest for engineering applications.

The objective of the current research is to determine the effect of blind angle, blind tip-to-window spacing, and absorbed solar heat flux into the blind, on the free convective heat transfer in a double glazed window with a between-panes Venetian blind. The isothermal plates will mimic the temperature difference between the outdoor glazing and the indoor glazing. The blinds will be electrically heated to mimic the absorbed solar radiation. The apparatus will use 44 blinds in order to highlight the affect of large aspect ratio on the flow stability of the cavity fluid. Interferometry will be used to determine the temperature distribution inside the enclosure, and to determine the local convective heat transfer rates at the plate surface. The primary purpose is to validate the RSL model and to obtain a set of experimental data to validate future numerical studies.

Chapter 2: Experimental Apparatus

2.1 Introduction

Experimental measurements were made using a Mach-Zehnder interferometer (MZI). An MZI is an optical instrument for measuring convective heat transfer rates. The MZI provides a full temperature field representation of the experimental domain, which can be used to determine local and average heat transfer rates.

The MZI was used to make measurements on a between-the-pane Venetian blind experimental setup. The window glazings were simulated with aluminum plates. The effect of absorbed solar radiation was simulated with electric resistors placed on the blinds. A description of the various components of the Mach-Zehnder interferometer and the experimental apparatus will be discussed next.

2.2 Interferometer

The current Mach-Zehnder interferometer used in the laboratory was built by Von Bistram. A more detailed description is found in Von Bistram's undergraduate thesis (1995). That design was based on the interferometer developed by Tarasuk (1968) at the University of Saskatchewan and the interferometer used at University of Western Ontario.

A visual representation of the Mach-Zehnder Interferometer is shown in Figure 1. The MZI works by measuring the relative change of the index of refraction of the test fluid. In the current study, the test fluid is air. Assuming an ideal gas, the change in index of refraction can

be related to temperature change to give the full temperature field of the problem domain. Using an array of optics, a collimated laser beam (a 15 mW Helium-Neon laser of wavelength $\lambda = 6.328 \times 10^{-7}$ m) is split into two separate beams. The two beams are initially in phase due to the fact that they come from the same source. One beam passes through ambient air while the other beam passes through the experimental apparatus. The heating of the experimental domain changes the air density, causing a change in index of refraction. The change of index of refraction relative to the ambient beam creates a phase shift. This phase shift appears as constructive and destruction fringes when the two beams recombine. For the MZI shown in Figure 2.1, the final recombined beam is focused in order to be photographed. The output (also known as an interferogram) was photographed on a 4" x 5" positive/negative Type 55 Polaroid Land film.

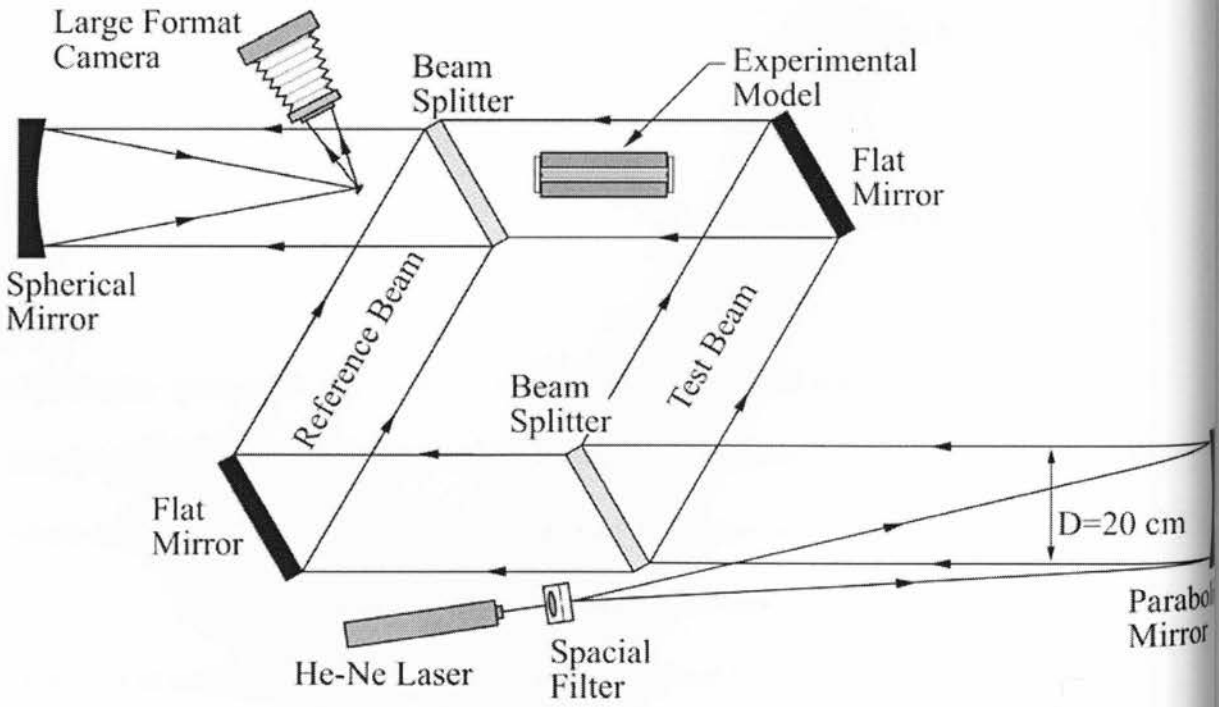

Figure 2.1: Overhead view of the Mach-Zehnder Interferometer (MZI)

The MZI technique is the preferred method of heat transfer measurement for this experiment for many reasons. The MZI is a non-intrusive technique and thus, measurements can be made without affecting the flow pattern or temperature. Also, the MZI is not affected by thermal radiation. So, the convective heat transfer rate is measured directly and the results do not have to be corrected for radiation. There is no thermal inertia, giving real time flow measurement. This feature makes it possible to capture time dependent phenomena.

However, there are some disadvantages associated with using the MZI. The MZI obtains the temperature field for a two dimensional slice of the experimental domain by spatially averaging the temperature field along the path of the laser. This averaging makes it difficult to capture turbulence. Also, this characteristic makes the accuracy of two dimensional results susceptible to three dimensional effects. The optical equipment used in the MZI is expensive, fragile, and any imperfections in the optics (i.e., dust, scratches… etc) can affect the results. Also, the results are sensitive to vibration, which makes obtaining accurate results more difficult.

To minimize the effect of vibrations the entire MZI apparatus was placed on top of a 364 kg bench of size 1.205 m x 3.03 m which was elevated on a series of air filled rubber tubes. The surface of the bench has a 'peg-board' like construction with ¼-20NC tapped holes equally spaced at 25.4 mm apart. The various optics and laser are mounted to these holes.

2.3 Venetian Blind

For the experiment, 44 aluminum slats were used from a commercially available Venetian blind. The slats had a length of 52.7 mm and a flattened width of 25 mm. All the slats were coated with a white paint to give a hemispherical emissivity of $\varepsilon = 0.89$. The emissivity of

the painted surface was measured at the University of Waterloo, using a Gier-Dunkle Reflectometer.

Two electric thin film resistant heaters were affixed to each slat, in order to simulate the effect of absorbed solar radiation for summer daytime conditions. The heaters were attached to the concave (bottom) side of the each slat using pressure sensitive adhesive. Each heater had a length of 254 mm and a width of 19.05 mm and a rated resistance of 60.8 ohms (measured nominal resistance of 58.3 ohms). The resistors were 'paired' by their measured resistance in order to make each blind slat have the same overall resistance. A schematic of the resistor wiring is shown in Figure 2.2. The resistors were connected in series with the resistor directly above or below to create resistor pairs. Then each resistor pair was connected in parallel. On selected blinds, a fine 40 gauge type T thermocouple wire was attached at the midpoint of the blind slat.

All the 44 blinds where held in place by a square steel post at both ends of the blinds. The steel post had a width of 3/16" and 46 threaded holes of diameter 3/32". The center 44 holes were equally spaced at 7/8" apart in order to hold the blinds in place at the typical pitch distance for commercial Venetian blinds. The topmost and bottommost holes where used to set the acrylic end spacers. Beneath each threaded hole were two holes to allow room for wiring from the resistors and thermocouples.

A figure of the blind slat is shown in Figure 2.3. The blinds were held in place with the use of a nylon threaded rod. One end of the nylon rod was placed in the threaded hole of the steel posts and the other end was placed in a notch cut out from the ends of the blind slats. Nylon rods were used to reduce heat loss due to conduction from the ends of the blind slat.

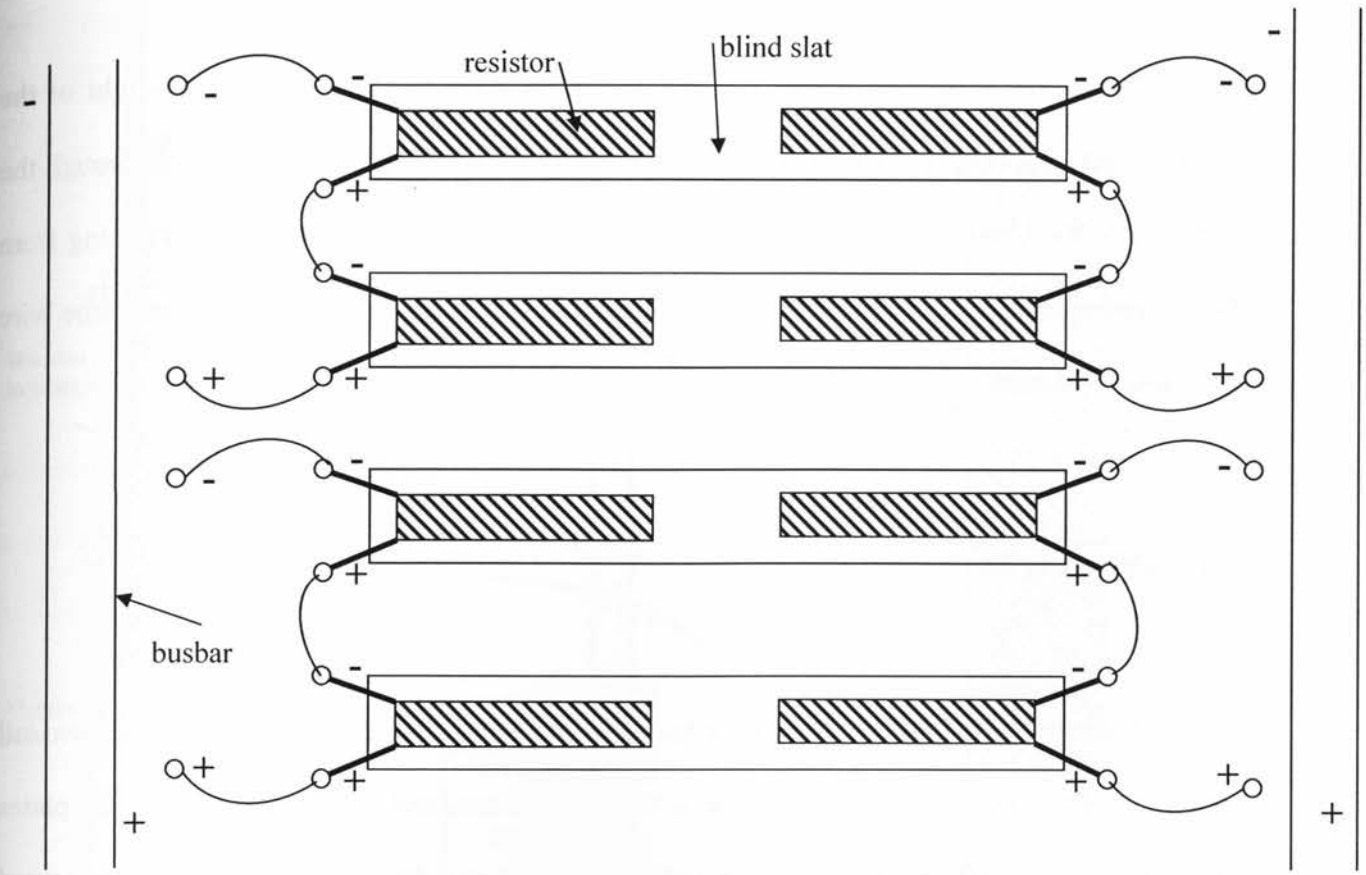

Figure 2.2: Schematic of the electric resistor wiring

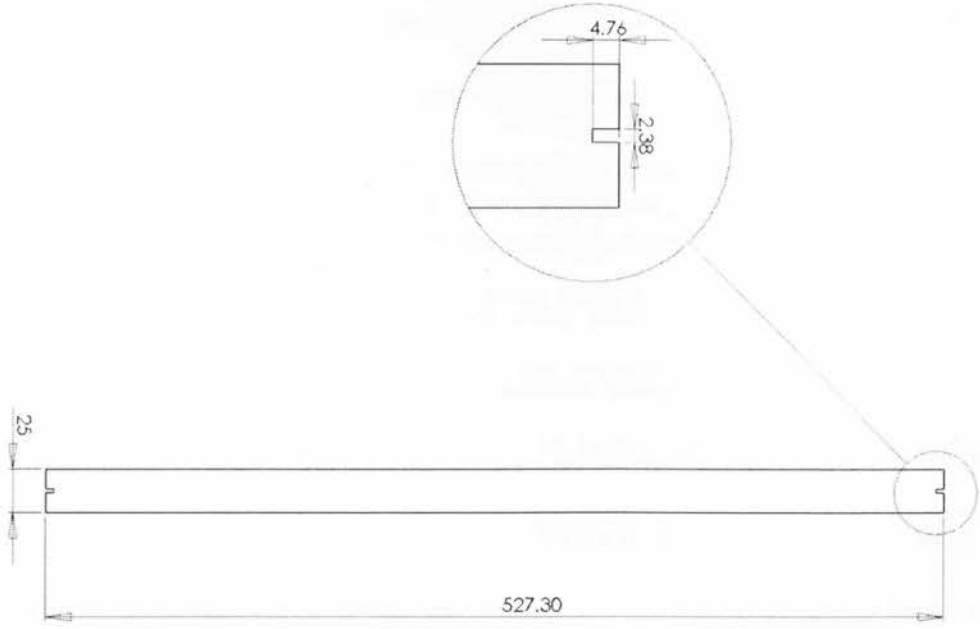

Figure 2.3: Mechanical drawing of a blind slat (dimensions are in millimeters)

During the assembly, it was noticed that the blinds "sagged" due to the weight of the resistors and long length of the blind slats. To remedy this, a fine hole was punched through the midpoint of the blind slats and nylon fishing wire was sewed through the blinds and hung from the top end spacer. Small aluminum crimps (fishing line weights) were then attached to the wire underneath the slats to prop up the slat.

2.4 Cavity

A schematic diagram of the cavity is shown in Figure 2.4. The cavity consists of two tall aluminum plates with a height of 994mm, a width of 540mm and a thickness of ¾". The plates were coated with a white paint to give an emissivity of $\varepsilon_P = 0.89$. The emissivity was measured using an infrared reflectometer at the University of Waterloo.

The dimensions of the plates were determined to optimize the performance of the interferometer and to give a larger aspect ratio than previous between-pane venetian blind studies. Ideally, the width of the plate should be small in order to give enough visible fringes. If the plate width is too large then refraction errors can be significant. However, if the plate width is too small, then end effects will create three dimensional flows and a uniform center glass region cannot be obtained. The chosen dimensions give 12.3 fringes (or 1.22 fringes per °C) across the cavity, for a wall-to-wall temperature difference of $\Delta T = 15°C$.

The plates were temperature controlled with constant temperature baths using water. Water was pumped through a series of ¼" copper tubes that were pressed up against the

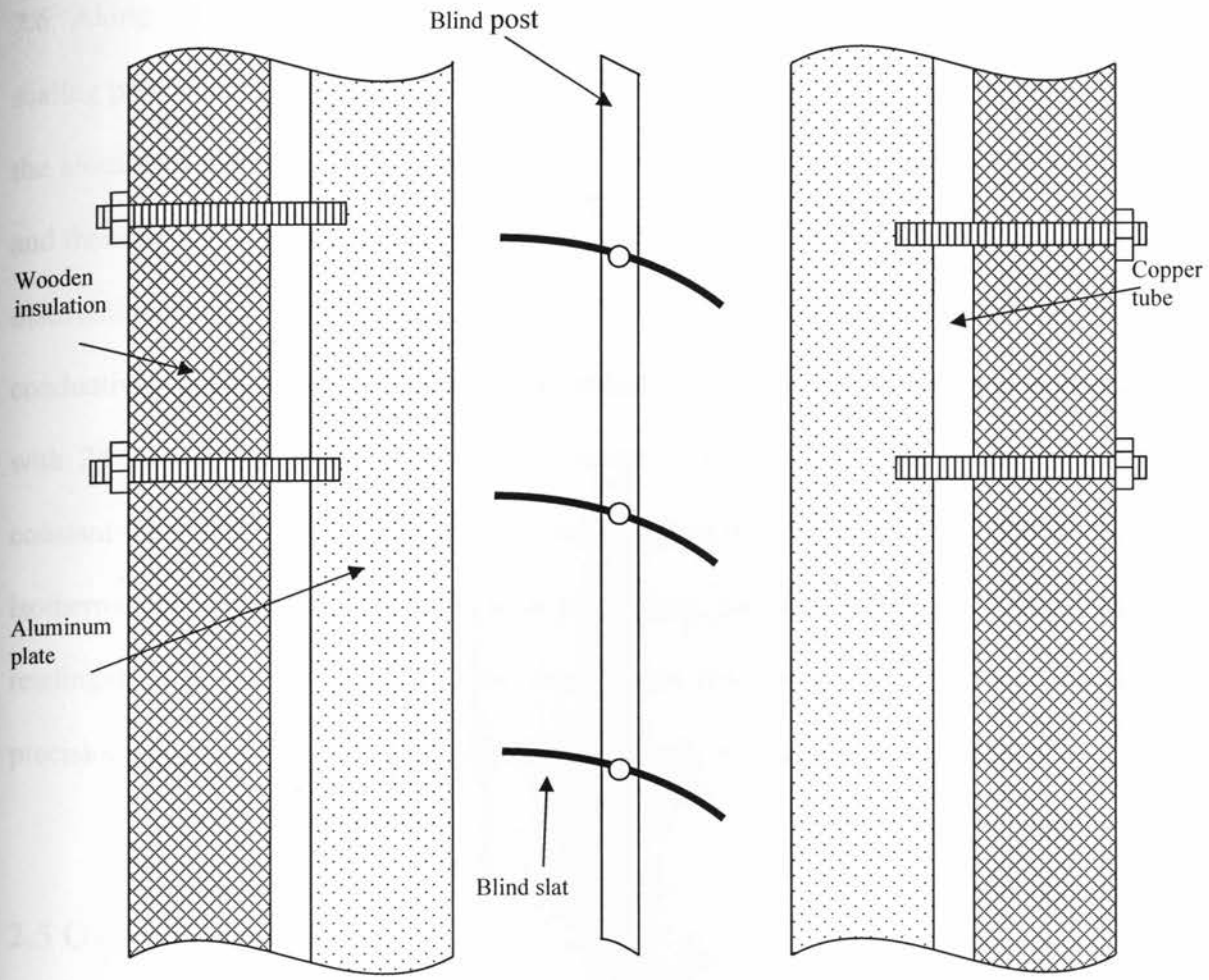

Figure 2.4: Cross-sectional view of the cavity

aluminum plates. A sketch of the cooling/heating system is shown in an exploded view of the plate assembly in Figure 2.5. The sizing of the copper tubes and the size of the constant temperature baths were carefully calculated in order to give enough cooling/heating to maintain uniform temperatures of the plates. A finite element analysis was performed to ensure the plates were sufficiently isothermal.

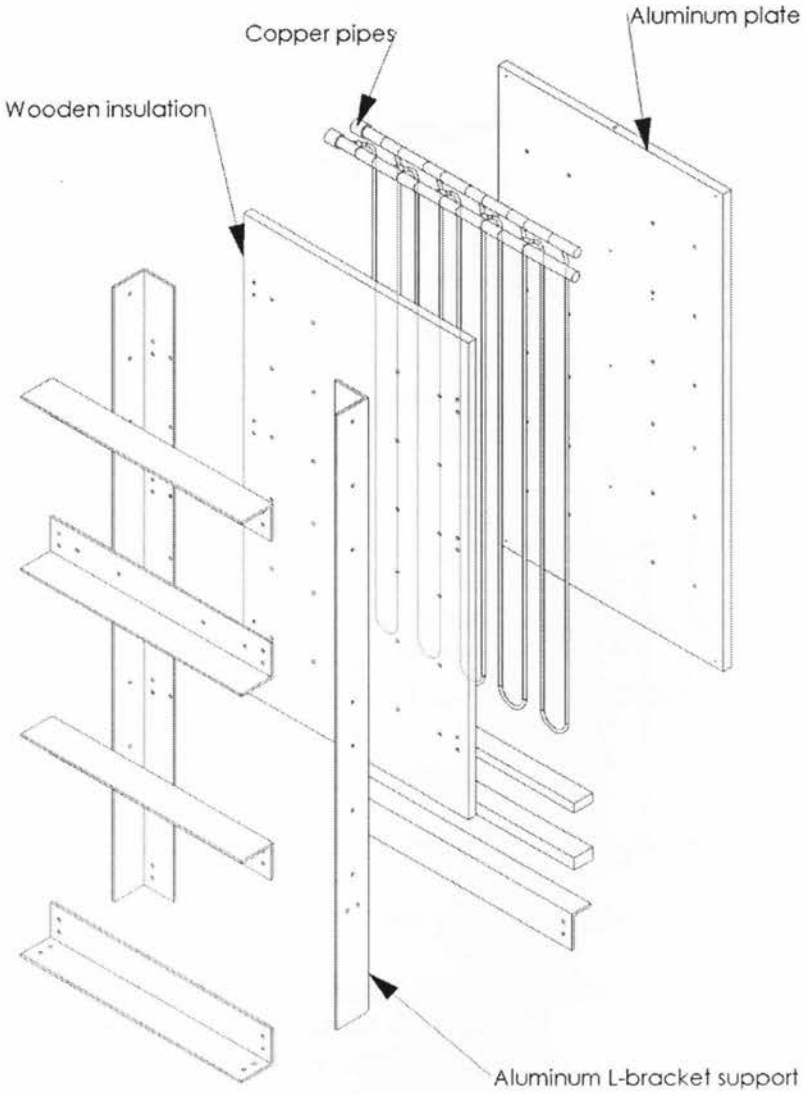

Figure 2.5: Exploded view of one plate assembly

A mechanical drawing of the front side of one of the aluminum plates is shown in Figure 2.6. Along the front surface of the plate (the surface exposed to the cavity) are leveling and scaling pins located throughout the plate. Figure 2.7 shows the drawing of the back surface of the aluminum plates. Along the back of the plate there are holes for thermocouple placement and threaded holes used for assembly. The thermocouples were used to measure the temperature distribution of the plate. The thermocouples were placed in the holes with high thermal conductivity paste to improve the thermal contact with the plate. The thermocouples were made with 24 gauge wire using a Type T connector. The thermocouples were calibrated with a constant temperature bath using a high precision glass thermometer. The plate was found to be isothermal to within 0.74°C (taken from the largest deviation of the calibrated thermocouple readings). The top and bottom of the cavity were fitted with an acrylic end spacer that was precision machined to provide gap widths of 32.7 mm, 40.7 mm, and 56.7 mm.

2.5 Overall Assembly

The overall assembly is shown in Figure 2.8. The structure stands at 155.8 cm tall, 85.4 cm wide, and 83.2 cm long. The two aluminum plates that make up the cavity are held in place by aluminum angle brackets of 76.2 mm x 76.2 mm x 4.76 mm. One plate is fixed to the base platform (which has a support leg length of 129.3 cm) and the other plate is on a movable metal plate (which has a support leg length of 128 cm) that slides on two rails.

The aluminum plates weigh approximately 27.6 kg and hang out in front of the angle bracket legs by 9.2 cm. This creates a large torque at the base of the support legs. To fix this

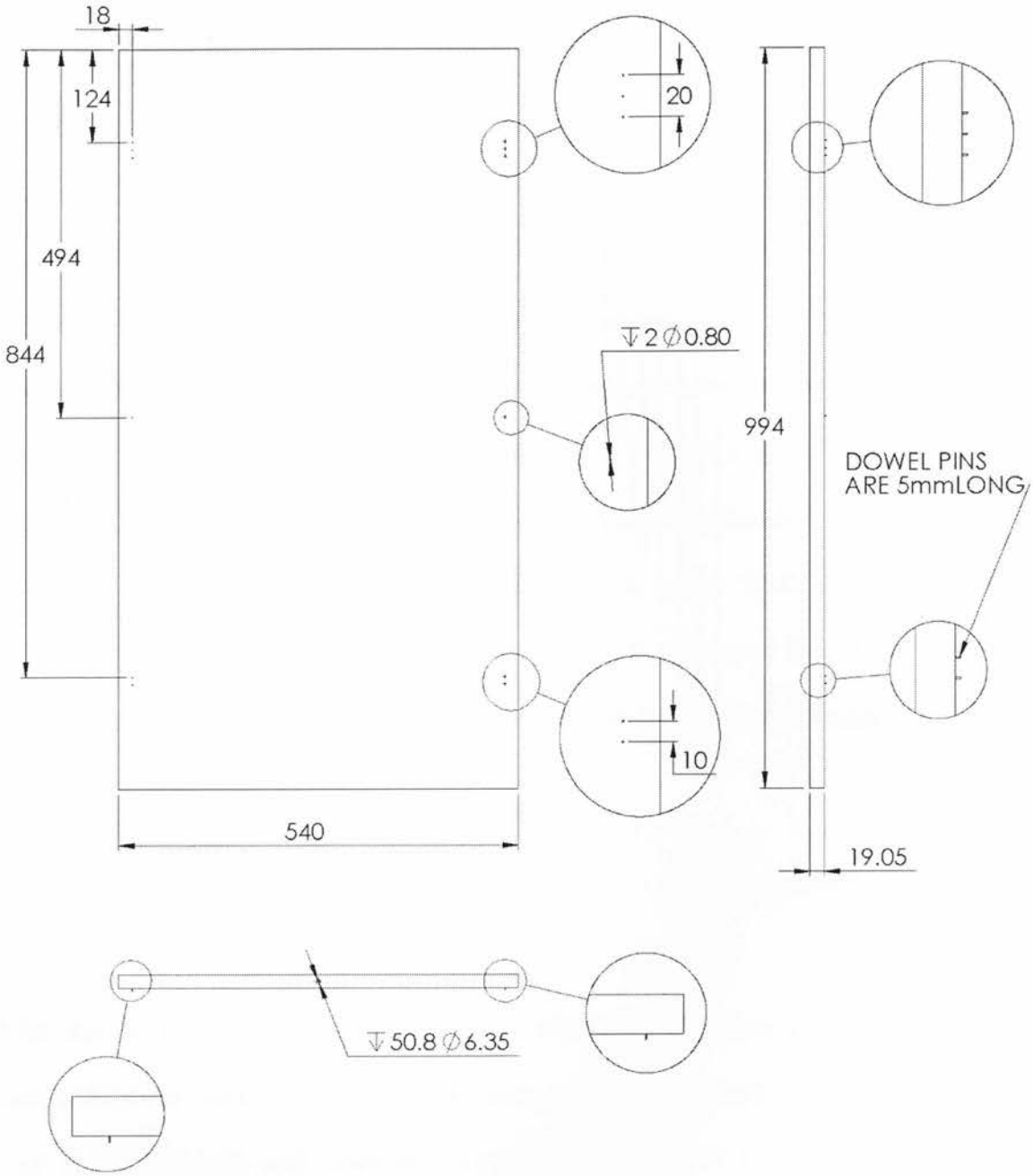

Figure 2.6: Mechanical drawing of the front side of the aluminum plate

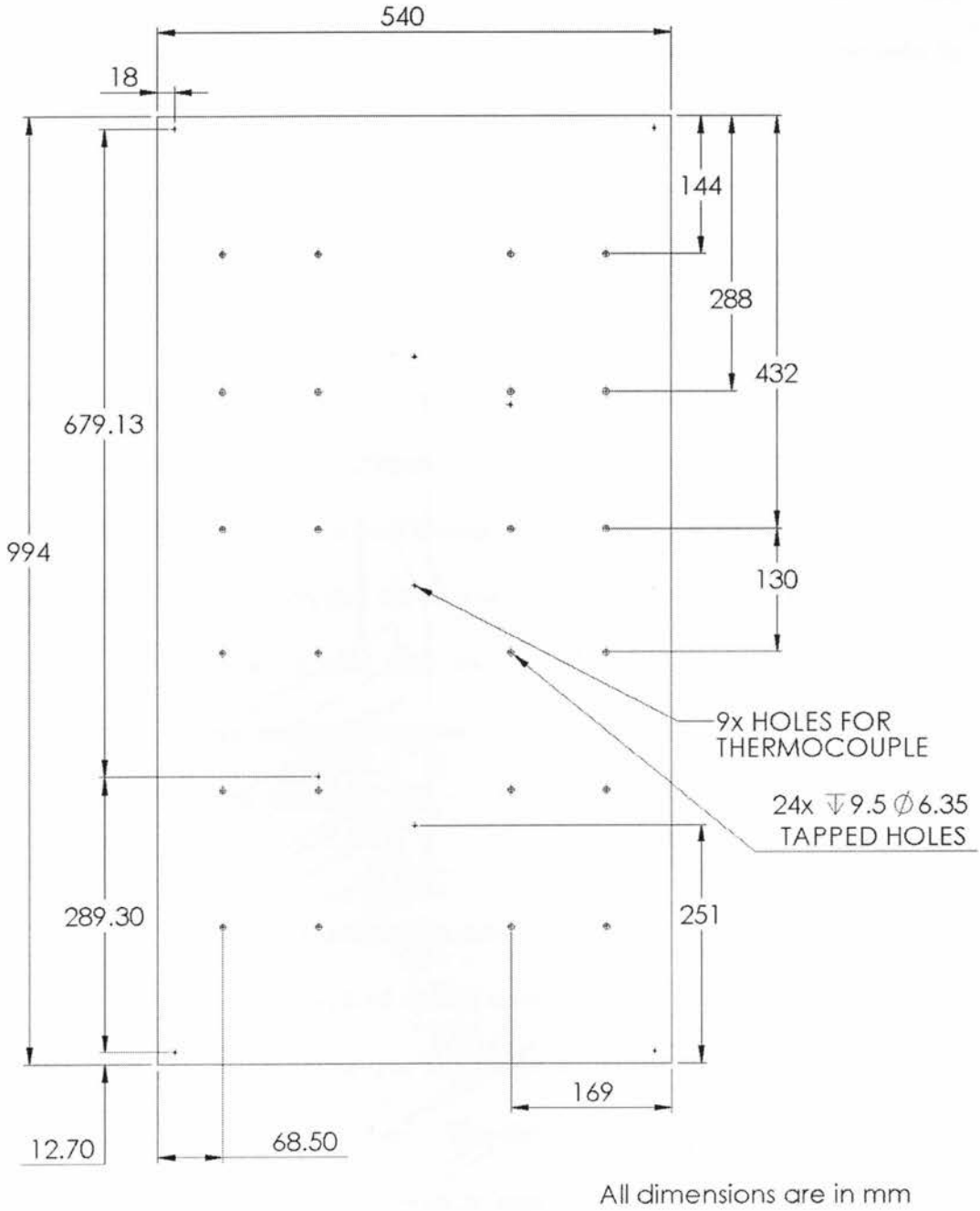

Figure 2.7: Mechanical drawing of the back side of the aluminum plate

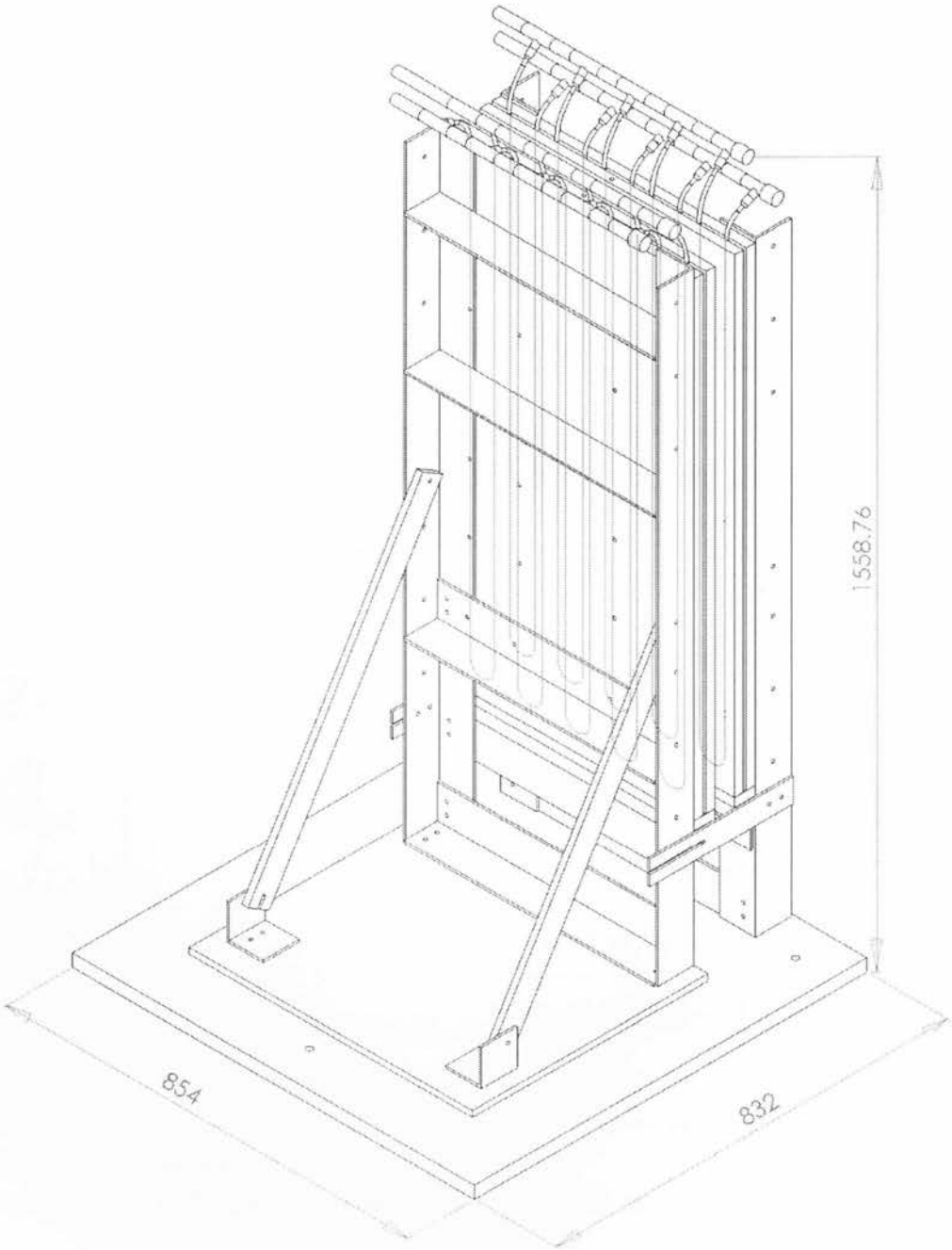

Figure 2.8: Overall mechanical drawing of the experimental apparatus

problem, the fixed plate is held in place by a 2.54 cm thick angle bracket across the support legs. On the movable plate, a triangle support was attached to the support legs, which can be seen in Figure 2.8.

Acrylic plates were pressed up against the ends of the cavity in order to create a closed structure. The plates were lined with ¾" thick weather stripping to create an air tight seal. Due to the optical imperfections of acrylic, special high quality optical windows were placed in the center glass region in order to give better interferometric results. The two plates, acrylic sheets and optical windows were all held in place using clamps.

In order to minimize the heat loss effects through the end walls and edges, the plate-to-plate temperature difference was set such that the average plate temperature is equal to ambient temperature. For example, consider a cold plate temperature of T_c = 12.5°C, a hot plate temperature of T_h = 27.5°C and an ambient temperature of 20°C. With these temperatures the wall-to-wall temperature difference would be ΔT = 15°C and the average plate temperature would be T_{avg} = 20°C.

The entire structure was placed on a movable scissors jack to allow vertical translation of the apparatus. The apparatus was lifted to allow optical access to the center glass region.

The MZI and entire experimental apparatus was located in an enclosure to create a quiescent environment to reduce natural convective errors. The room was custom made using a wood frame and a tarp covering the structure. The room is large enough to contain the entire MZI apparatus in a 3.66 m x 6.10 m x 2.44 m enclosure. The room was meant to: 1) reduce externally produced convection and 2) create a 'dark' room that is suitable for taking the interferogram images.

Chapter 3: Experimental Procedure and Analysis

3.1 Introduction

A Mach-Zehnder Interferometer (MZI) was used to make convective heat transfer measurements. The results were analyzed using image processing software to obtain local and average convective heat transfer rates. Forty-three experiments were performed for the following range of variables:

Blind angle: $\phi = 0^o$, and 45°

Plate temperature difference: $\Delta T = 0^oC$, and 15^oC

Gap width: $W_G = 32.7$ mm, 40.7 mm, and 56.7 mm

Blind heat flux: $q_B'' = 0$ W/m^2, 75 W/m^2, and 150 W/m^2

Each experiment was done twice to get both the finite and infinite fringe interferograms resulting in eighty-six photographs. A description of finite and infinite fringe interferograms will be discussed next. Also, a description of the experimental procedure and heat transfer analysis will be discussed.

3.2 Interferograms

A description of the MZI is given in Section 2.2. Referring to that description, the destructive/constructive interference pattern of the interferogram is created when the reference

beam and test beam recombine at the beam splitter. If the two beams are parallel when they recombine, the interferometer is considered to be in infinite fringe mode. In this mode, the destructive and constructive fringes correspond to lines of constant temperature. This provides temperature field visualization of the experiment domain. A figure of an infinite fringe interferogram is shown in Figure 3.1a.

When the two beams are purposely misaligned the interferometer is said to be in finite fringe mode. In this mode, the fringe pattern appears as horizontal lines in ambient air with no temperature distribution. When there is a temperature variation, the fringes will bend 'up' into increasing air temperature and bend 'down' in decreasing air temperature. A figure of a finite fringe interferogram is shown in Figure 3.1b.

Infinite fringe mode is ideal for visualization purposes. However, in this mode, the fringes are sensitive to vibrations and it is difficult to get measurements in low temperature gradient regions. Thus, for the analysis, the finite fringe mode is used due to its improved accuracy. Also, it is easier to set up than the infinite fringe mode.

3.3 Experimental Procedure

The table bed was leveled using a spirit level by inflating/deflating air filled rubber tubes that held up the optical bench. The laser was turned on and the optics aligned. The optics were individually checked to ensure that the beam was uniform and incident onto the centre of each optic.

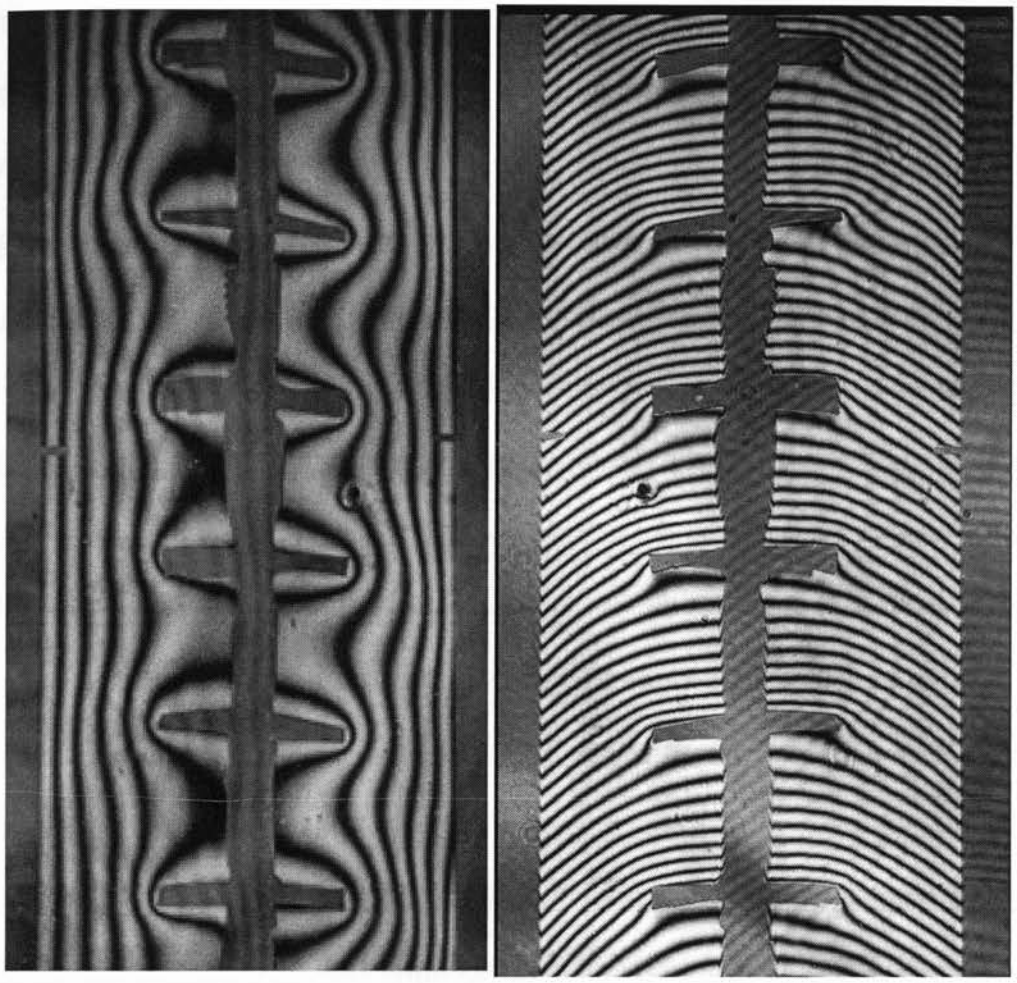

a) Infinite fringe **b) Finite fringe**

Figure 3.1: Infinite and finite fringe interferograms for $\phi = 0^o$, $q''_B = 75$ W/m^2, $\Delta T = 0^oC$.

Once the laser and optics were aligned, the model was prepared for the experiment. The blind assembly was designed to be a separate structure from the rest of the apparatus, allowing for easy disassembly of the blind. First, the blind assembly was placed in the cavity and the louvers were set to the appropriate angle. Then the acrylic sheets and optical windows were attached to the structure to create a sealed enclosure. Finally, the entire apparatus was moved into the test beam and the thermocouples were connected.

With the optics prepared, the model needed to be aligned relative to the gravity vector and the laser beam. The cavity was aligned vertically using a plum bob hanging from the

ceiling. Horizontal alignment was done using a spirit level. The test beam was aligned relative to the cavity such that the laser beam was parallel to the plate surface. This was done by looking at the shadows of two precisely placed leveling pins in the laser output. The optics were adjusted so that the two shadows of the pins coincided. An infinite or finite fringe pattern was obtained using the far-field/near-field method, as described by Tarasuk (1968).

The camera was placed in line with the laser output and was adjusted so that the image appeared in the frosted glass back. Then the desired interference pattern was set on the frosted screen of the camera, while the model was unheated.

To control the heat flux of the blinds, the electric resistors were connected to a DC power supply. Two multimeters were connected to the wiring in order to measure the voltage and the amperage. One multimeter was set in parallel with the blind wiring to measure the voltage, and another multimeter was set in series to measure the amperage. With the amperage, voltage, resistance, and louver surface area known, the blind heat flux can be determined. The blind heat flux is based on the surface area of one side of the blind slats. The voltage and amperage were incrementally adjusted until the desired heat flux was achieved within ± 0.1 W/m^2.To control the wall-to-wall temperature, each plate was connected to its own constant temperature bath. A high accuracy Platinum resistance thermometer was placed in each plate. The thermometers were operated in differential mode to provide an accurate ΔT, since the plate temperature differed from the readings on the constant temperature baths. The temperature of the constant temperature bath was iteratively adjusted until the desired plate-to-plate temperature difference was achieved within ± 0.02 K

With the apparatus and optics prepared, the model was heated to the desired temperature setting. Care was taken to bring the plate to the desired temperature due to the high thermal

mass of the plates. Once steady state was reached, all parameters from the data acquisition system, constant temperature baths, and ambient air properties were recorded.

With the parameters recorded, the lights were turned off and the interferogram was photographed on large format film (Type 55 Polaroid Land). Once the film negative dried, it was scanned using a flat bed negative scanner for analysis using in-house image processing software.

The ambient air temperature was recorded using a high precision glass calibration thermometer and ambient pressure was recorded using a mercury barometer.

3.4 Interferogram Analysis

The analysis of interferograms was the same for infinite and finite fringe interferograms. An MZI measures the changes in the index of refraction of air. Assuming the ideal gas law and constant pressure, the changes in index of refraction can be related to changes in temperature (Lai, 2004). Equation 3.1 gives the temperature for a given fringe shift ε:

$$T = \frac{T_{REF}}{1 \pm \frac{\varepsilon R \lambda T_{REF}}{GPZ}} \tag{3.1}$$

where R is the gas constant (287 J/kg•K), G is the Gladstone-Dale constant ($G = 0.226 \times 10^{-3}$ m^3/kg), P is the absolute ambient pressure (measured from a mercury barometer), Z is the length of the laser path through the experimental model (Z = 547 mm), λ is the vacuum wavelength of the light source ($\lambda = 6.328 \times 10^{-7}$ m), and T_{REF} is some known reference temperature. The fringe

temperature is determined relative to a reference temperature. For all experiments, the reference temperature used was the surface temperature of the closest plate. A plus or minus sign in the denominator is chosen based on the density gradient of the chosen fringe. If the fringe of interest is in a region of increasing index of refraction then the 'plus' sign is chosen, otherwise, the 'minus' sign is chosen.

For an infinite fringe interferogram, Equation 3.1 can be used to determine every fringe temperature to give a full temperature field if needed. For a finite fringe interferogram, Equation 3.1 can be used to determine the temperature distribution normal to the plate surface. All analysis was done using finite fringe interferograms.

3.5 Local and Average Convective Heat Transfer Rates

Using Equation 3.1 for a finite fringe interferogram, the temperature gradient normal to the plate surface can be determined. By determining the temperatures of the first two consecutive fringes and assuming a linear interpolation, the temperature gradient at the plate surface can be determined. An illustration of the temperature gradient is shown in Figure 3.1.

With the surface temperature gradient known, the convective heat transfer rate can be equated to the conductive heat transfer rate as shown in Equation 3.2:

$$q'' = -k_S \left.\frac{dT}{dy}\right|_{y=0} \tag{3.2}$$

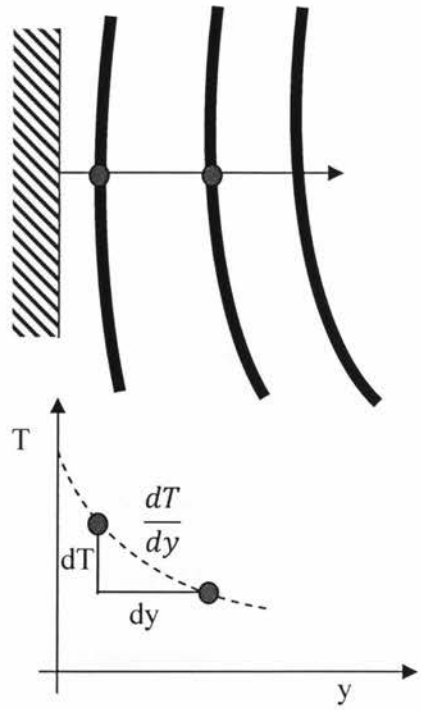

Figure 3.2: Illustration of the method used to calculate the surface temperature gradient.

where 'k_S' is the thermal conductivity of the air evaluated at the wall surface temperature, 'dT/dy' is the temperature gradient at the wall surface, 'h' is the convective heat transfer coefficient,, and q″ is the local convective heat transfer rate per unit area (heat flux).

The local convective heat flux was calculated at eighty evenly spaced intervals at the center glass region, over a distance of 89 mm. The entire process was automated using image processing software developed by the author. A description of the image processing software is explained in Appendix A. The average convective heat flux values were calculated by numerically integrating the local convective heat transfer rates using the trapezoidal rule.

CHAPTER 4: Results and Discussion

4.1 Introduction

A Mach-Zehnder laser interferometry was used to make free convective heat transfer measurements in a double glazed window with a between-the-pane heated blind. The measurements were done for a variety of parameters: cavity widths of W = 32.7 mm, 40.7 mm, and 56.7 mm, blind angles of ϕ = -45°, 0°, and 45°, blind heat fluxes of $q'' = 0$ W/m^2, 75 W/m^2, and 150 W/m^2, and glazing to glazing temperature differences of $\Delta T = 0$ °C, and 15 °C (these parameters are nominal values). Measurements were taken only at the center glass region which is at the midpoint of the 994 mm tall cavity. Analysis was done on finite fringe interferograms due to their higher accuracy compared to infinite fringe interferograms. For temperature field visualization, infinite fringe interferograms were used. All the interferograms in this chapter are in infinite fringe mode. The local convective heat transfer rates are shown for the cold wall only. The hot wall results gave a low temperature gradient in some cases and the interferometer was unable to make a measurement. To see the other results, the reader is referred to Appendix D. A detailed description of finite and infinite fringe interferograms is given in Section 3.2.

4.2 Local Convective Heat Transfer Results

4.2.1 General Behavior of the Local Convective Heat Transfer

Figure 4.1 shows the local heat flux variation along the vertical glazing for a blind angle of $\phi = 0$, a cavity width of W = 40.7mm, a blind heat flux of $q''_B = 75$ W/m^2 and a wall-to-wall temperature difference of $\Delta T = 0$ °C. Both the hot wall and cold wall heat fluxes are shown for comparison. The cavity is symmetrically heated by the blind; thus, the heat transfer is occurring from the blind and into both wall surfaces, giving a negative heat flux. The local and average convective heat transfer rates between the two walls are supposed to be identical; however, there is a discrepancy due to a slight bowing of the steel post. Also, some time varying effects were observed in the interferometer output.

There is a periodic variation of the heat flux along the glazing surface with the local minima corresponding to the location of the blind slat tips. This occurs because the aluminum blind slats are highly conductive and act as a thermal "bridge", increasing the local heat fluxes. Also because of the reduced space at the blind tip, this increases the fluid velocity which increases the convective heat transfer rates. Thus, the combination of the conductive thermal bridge and increased convective heat transfer rates contributes to the periodic variations in local heat flux.

In Figure 4.2 an infinite fringe interferogram is shown for the same experiment setup as in Figure 4.1. The constructive and destructive fringes are tightly spaced in the region around the blind tips and loosely spaced in the region between the blinds. Recalling that the fringes are

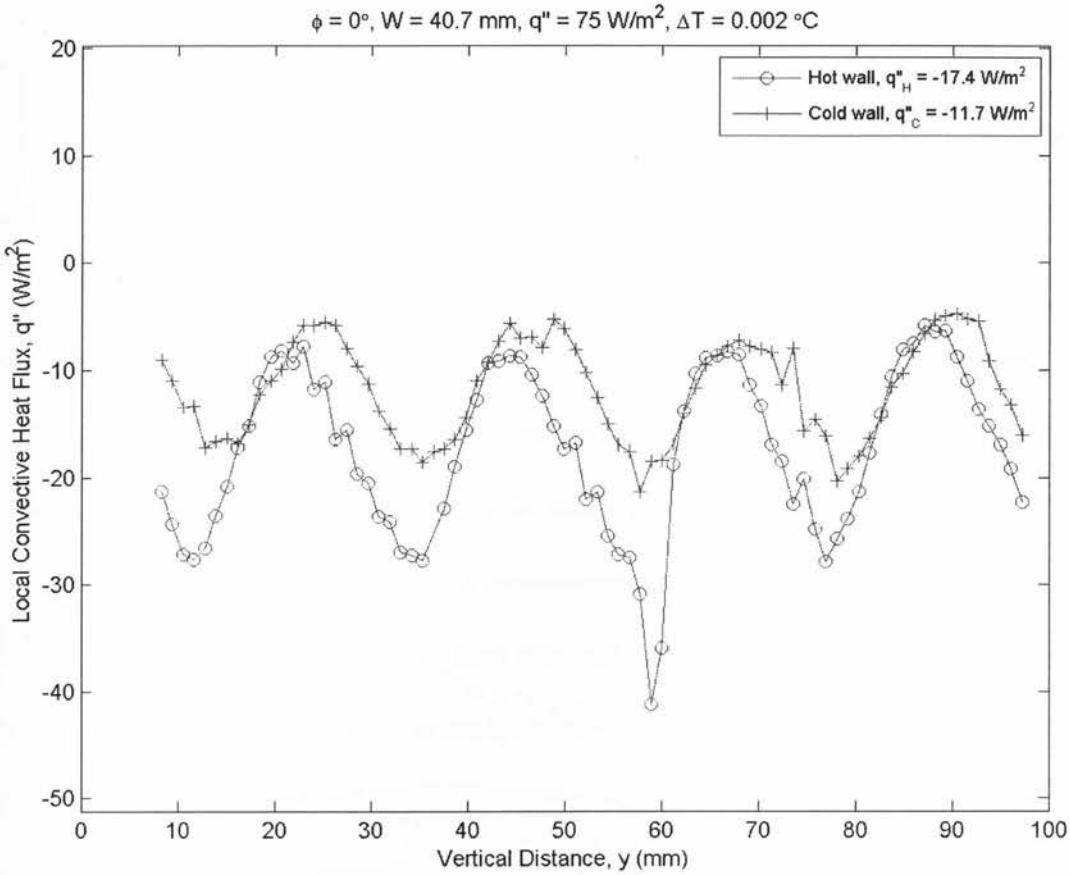

Figure 4.1: Local convective heat flux along the hot and cold walls for $\phi = 0°$, W = 40.7mm, $q''_B = 75$ W/m^2 and $\Delta T = 0$ °C.

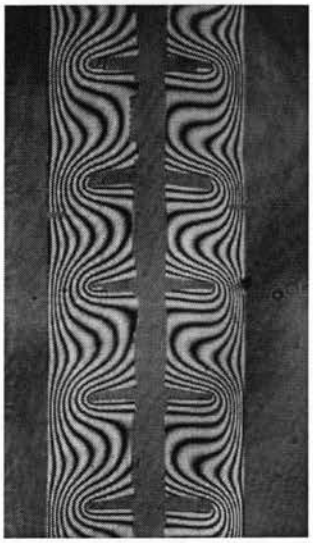

Figure 4.2: Infinite fringe interferogram for $\phi = 0°$, W = 40.7mm, $q''_B = 75$ W/m^2 and $\Delta T = 0$ °C.

lines of constant temperature, one can see that there is a larger temperature gradient in the area around the blind tips than the region between the slats. Thus, the interferogram is showing the same periodic variation of the heat transfer rate as seen in Figure 4.1

Figure 4.3 shows the hot wall and cold wall local heat flux variation for a blind angle of $\phi = 0°$, a wall to wall spacing of W = 32.7 mm, a blind heat flux of $q'' = 0$ W/m^2 and a glazing temperature difference of $\Delta T = 15$ °C. There are periodic variations of the local heat flux similar to that shown in Figure 4.1. However, in Figure 4.3, there is a temperature difference of $\Delta T = 15$ °C, making the heat flux distribution nonsymmetrical. The blind temperature is $T_b = 22.7$ °C and the hot wall and cold wall temperatures are 30.2 °C and 15.2 °C, respectfully. Thus, the heat flux exits the hot wall and enters the cold wall.

The corresponding infinite fringe interferogram is shown in Figure 4.4. As in Figure 4.2 above, there is a larger gradient of fringes around the blind tip than in the open space between the blind slats. Also, most of the temperature difference occurs in the boundary layer near the wall. This reveals the strong effect of conduction in the blind slats. In Figure 4.3, the average hot wall heat flux is $q''_H = 29.8$ W/m^2 and the average cold wall heat transfer rate is $q''_C = -30.6$ W/m^2, indicating good agreement between the two results. However, the amplitude of variation is larger for the cold wall than for the hot wall. This is due to a combination of the misalignment of the blinds and the small cavity width. In post processing, it was observed that the slat post is approximately 2.5 mm closer to one wall than the other due to a natural curvature of the post. The data in Figure 4.3 are for the smallest cavity width, which increases the sensitivity of the local heat transfer because of the narrow spacing between the blind tip and wall. It can be seen from Figure 4.4 that the blinds slightly rotated clockwise, causing the blind tip to be slightly closer to

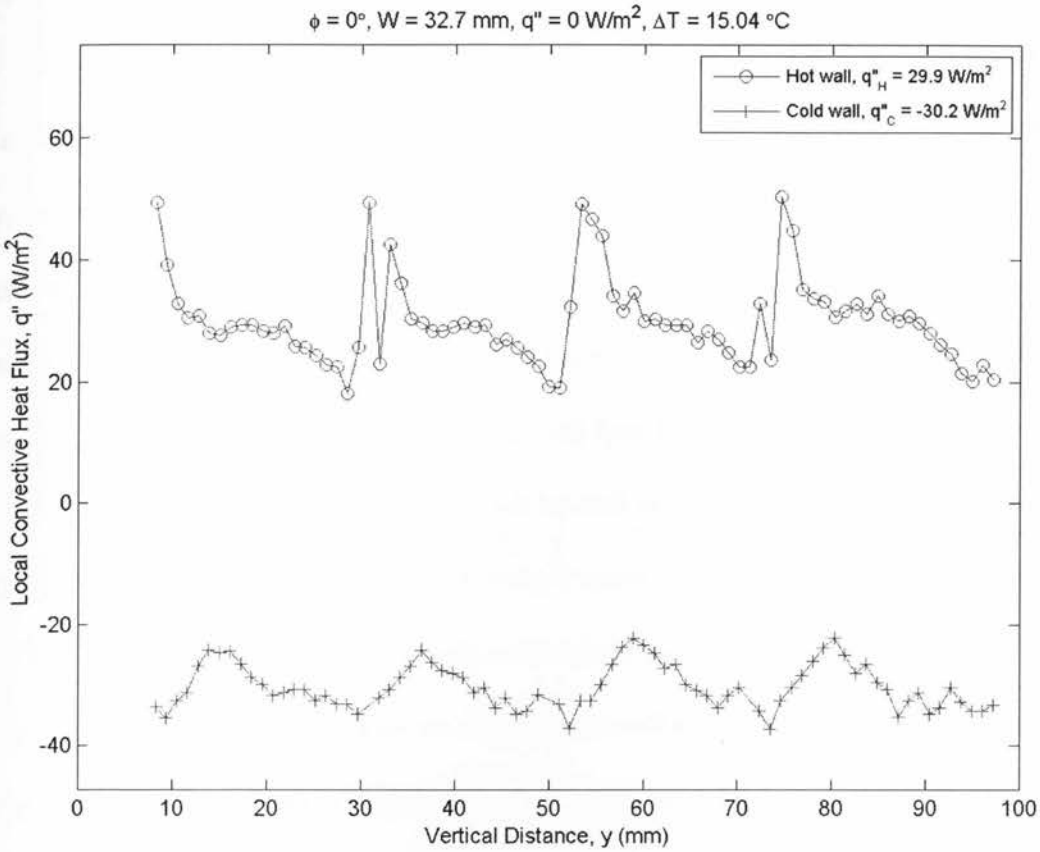

Figure 4.3: Local convective heat flux along the hot and cold walls for $\phi = 0°$, W = 32.7mm, $q''_B = 0$ W/m^2 and $\Delta T = 15$ °C.

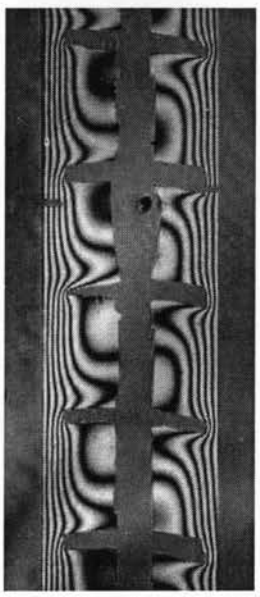

Figure 4.4: Infinite fringe interferogram for $\phi = 0°$, W = 32.7mm, $q''_B = 0$ W/m^2 and $\Delta T = 15$ °C.

the hot wall and slightly further away from the cold wall. Thus, there is greater periodic variation along the hot wall than the cold wall.

The hot and cold wall local heat transfers rates for a blind angle of ϕ = 45 °, a cavity width of W = 32.7 mm, a blind heat flux of q''_B = 150 W/m^2, and a wall-to-wall temperature difference of ΔT = 0 °C is shown in Figure 4.5. The corresponding infinite fringe interferogram is shown in Figure 4.6. Due to the blind heat flux of q''_B = 150 W/m^2, the blind slats are hotter than both of the walls. The hot blind and the approximately equal wall temperatures create a symmetrical heat transfer distribution on both of the walls.

However, the main difference from Figure 4.1 is the fact that the local heat transfer distribution on the two walls are out of phase from each other. This is due to a blind angle of 45°, causing the blind tips to be at different locations on each wall. This is seen in Figure 4.6, where the area of the largest gradient occurs at the blind tips, even though the blind tips are at different wall locations. There is a larger amplitude of variation for the cold wall than the hot wall. This is in part due to the curvature of the blinds. The blinds tips are slightly closer to the cold wall than the hot wall.

4.2.2 Effect of Wall Temperature Difference, ΔT

The effect of the wall temperature difference (ΔT) on the local heat fluxes for a blind angle of ϕ = 0°, a gap width of W = 40.7 mm, and a blind heat flux of q''_B = 150 W/m^2 along the cold wall is shown in Figure 4.7. Two cases are shown in Figure 4.7, one at ΔT = 0°C and the other at ΔT = 15°C. Again, there is a periodic variation along the wall corresponding to the location of the blinds. The ΔT = 0°C case has a blind temperature of 36.2 °C and a cold wall

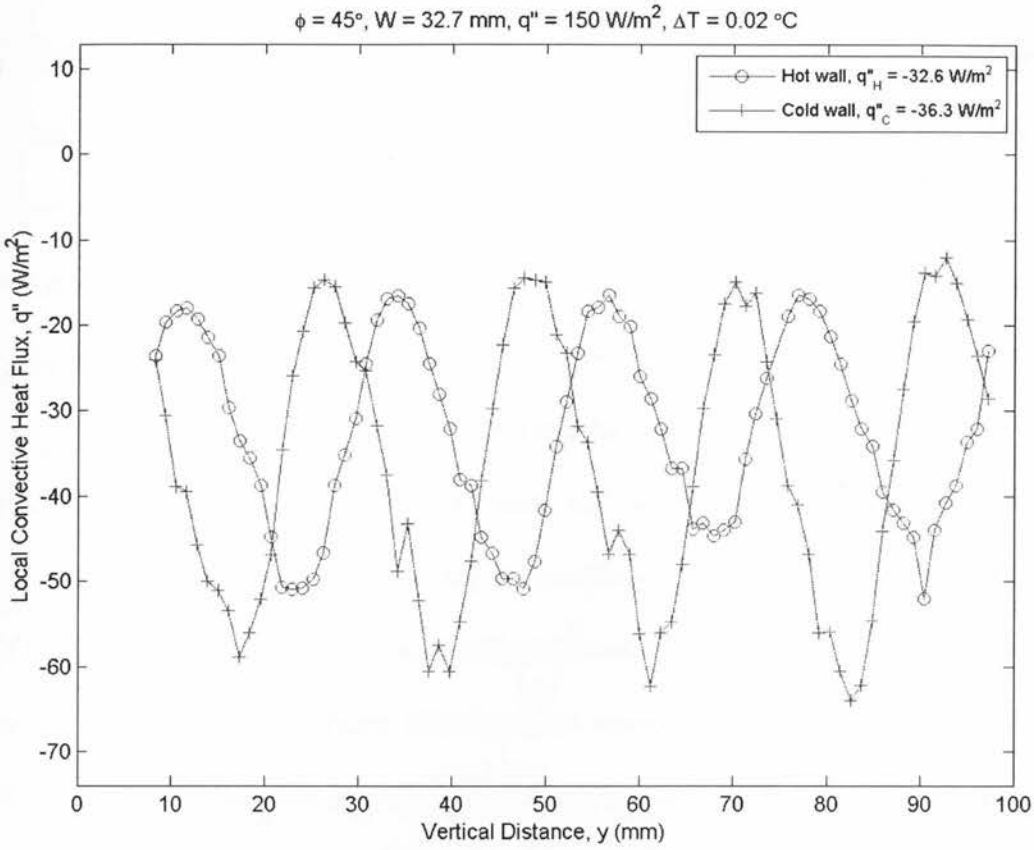

Figure 4.5: Local convective heat flux along the hot and cold walls for $\phi = 45°$, W = 32.7mm, $q''_B = 150$ W/m^2 and $\Delta T = 0$ °C.

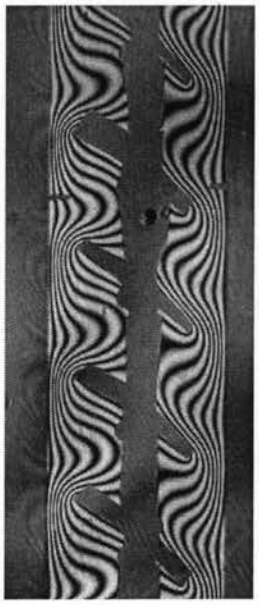

Figure 4.6: Infinite fringe interferogram for $\phi = 45°$, W = 32.7mm, $q''_B = 150$ W/m^2 and $\Delta T = 0$ °C.

temperature of 23.3 °C, giving a blind-to-wall temperature difference of 12.9 °C. For the ΔT = 15°C case, the blind temperature is 36.7 °C and the cold wall temperature is 15.9 °C, giving a blind to wall temperature difference of 20.8 °C. Thus, the ΔT = 15°C case will have a larger temperature gradient between the blind and cold wall region than the ΔT = 0°C case. The same phenomenon can be seen by comparing the infinite fringe interferograms of the two cases. Considering only the cold wall region, one can see that the temperature gradient (i.e., fringe gradient) is larger for Figure 4.8b than for Figure 4.8a.

There are periodic variations in the local heat flux distributions, as seen in previous figures. However, the peaks of these variations are out of phase. The locations of the maxima in the ΔT = 0°C case correspond approximately to the locations of the minima in the ΔT = 15°C case. This phenomenon is seen in Figures 4.8a and 4.8b which correspond to the infinite fringe interfergrams for the ΔT = 0°C case and the ΔT = 15°C case, respectively. Figure 4.8a shows that the temperature gradient is greatest between the blind tip and wall. However, Figure 4.8b has the greatest fringe gradient between the blind slats. This indicates that in Figure 4.8b there is a strong flow circulation in the area between the blind slats, increasing the convection in that region. Thus, the convection due to flow circulation is stronger than the convection/conduction combination occuring between the blind tip and wall.

Figure 4.9 shows the effect of wall-to-wall temperature difference for a blind angle of ϕ = 0 °, a gap width of W = 40.7 mm, and a blind heat flux of q''_B=75 W/m^2. For the ΔT = 0°C case, the blind-to-cold-wall temperature difference is 6.7 °C. For the ΔT = 15°C case, the blind-to-cold wall temperature is 14.5°C. In the ΔT = 0 °C case, we see similar behavior as in Figure 4.7, with periodic variations corresponding to the location of the blinds. This variation is also

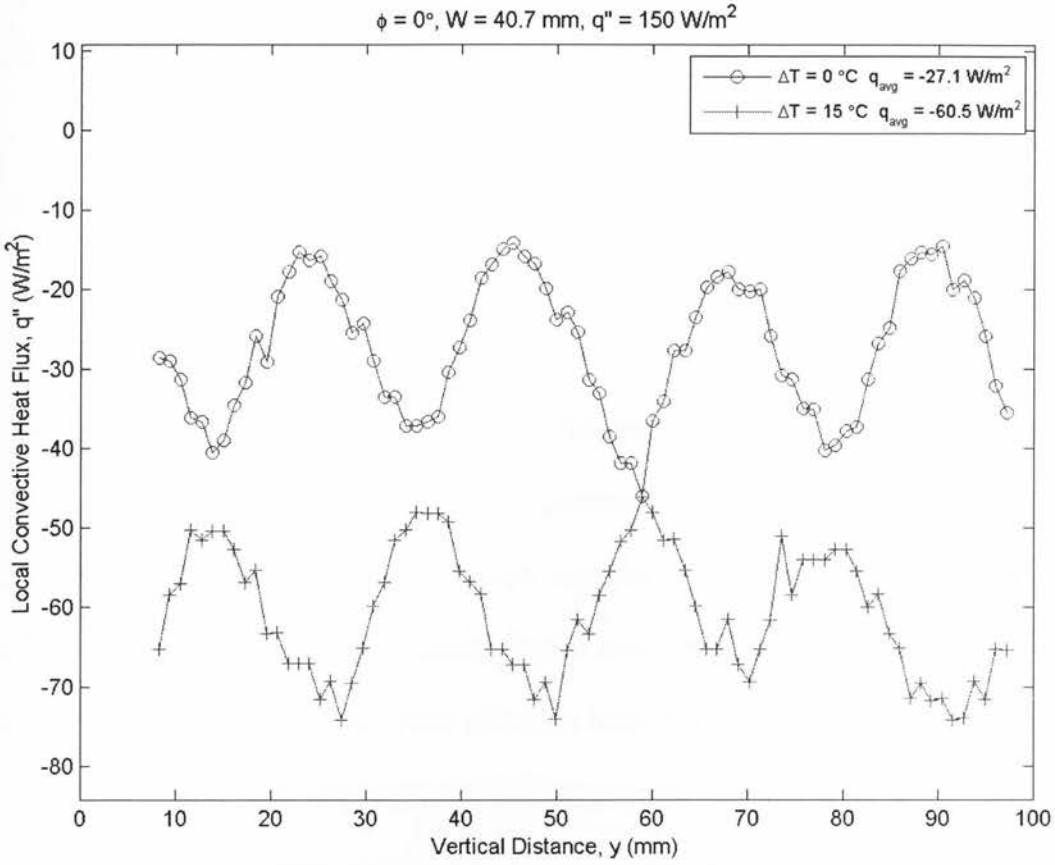

Figure 4.7: Local convective heat flux along the cold wall for $\phi = 0°$, W = 40.7mm, and $q''_B = 150$ W/m^2.

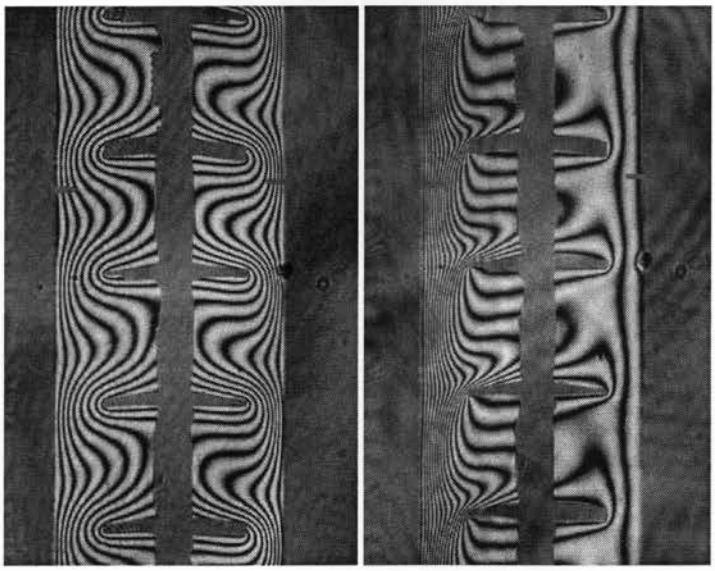

a) $\Delta T = 0°C$ b) $\Delta T = 15°C$

Figure 4.8: Infinite fringe interferogram for $\phi = 0°$, W = 40.7mm, and $q''_B = 150$ W/m^2.

seen in the interferograms in Figure 4.10a by examining a larger fringe gradient near the blind tip. Also, in Figure 4.10a, one can see that the fringes are uniformly spaced in the lateral direction, indicating that the cavity is dominated by conduction.

However, the local convective heat transfer for the $\Delta T = 15$ °C case (shown in Figure 9) does not behave as might be expected. Unlike the $\Delta T=0$°C case, the local convective heat transfer appears to be chaotic. Also, the magnitude of variation is smaller than the $\Delta T = 0$ °C case, even though there is a larger temperature difference. As was seen from Figure 4.7, the $\Delta T = 15$ °C scenerio had strong internal circulating flows which gave heat transfer peaks in the area between the blinds. As seen from previous figures, there is sometimes a conduction effect created by the blind slats which gave heat transfer peaks at the blind tip region. It is assumed that in Figure 4.9 , which has a lower blind heat flux than the case in Figure 4.7, the convection of the recirculating flow and the conduction of the blind slat are almost equal, effectively cancelling each other out and giving the 'flatter' distribution as seen in Figure 4.9.

In addition to the above mentioned effect, turbulence may also be responsible for the chaotic behaviour seen in Figure 4.9. It is possible that the flow between the blind tip and cold wall is unsteady. Looking at the boundary layer region of Figure 4.10b, one can see that there is well defined thermal bounday layer. However, this is only speculation and the true nature of the flow pattern can only be determined through flow visualization techniques.

4.2.3 Effect of Blind Heat Flux, q″

Results for a blind heat flux for a blind angle of $\phi = 0$ °, a wall to wall temperature difference of $\Delta T = 0$ °C and a cavity width of W = 32.7 mm is shown in Figure 4.11. Two cases

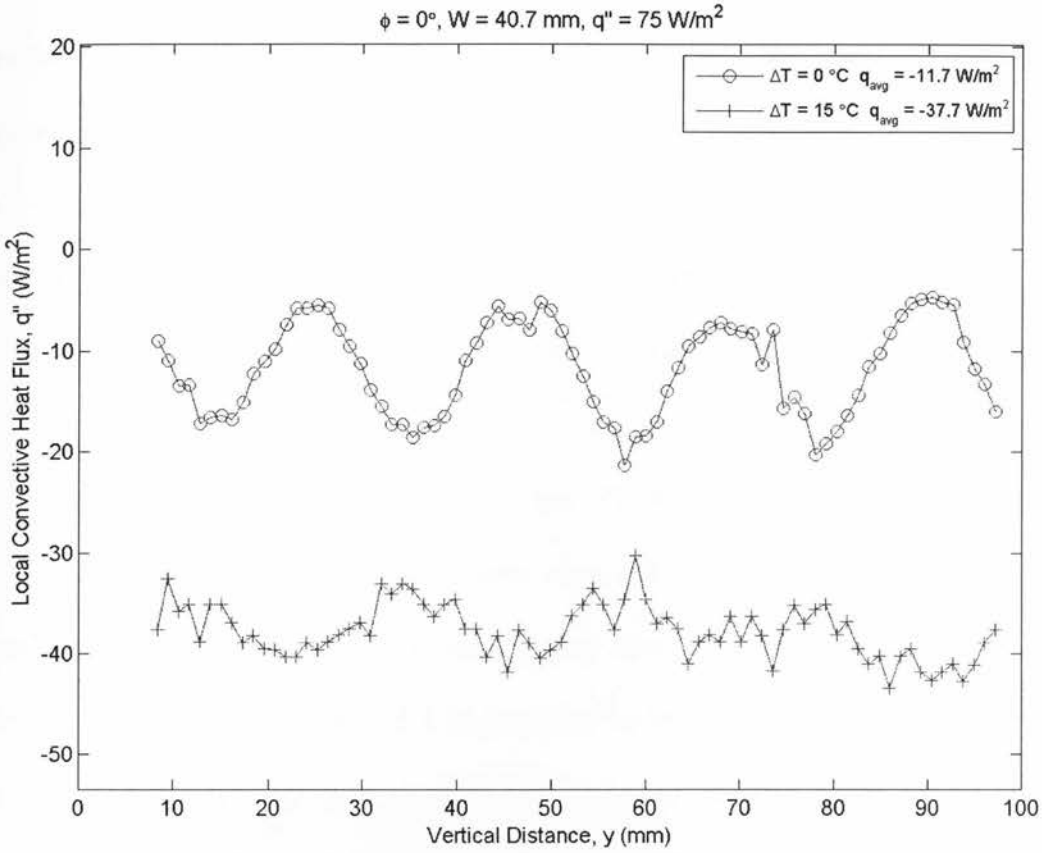

Figure 4.9: Local convective heat flux along the cold wall for $\phi = 0°$, W = 40.7mm, and $q''_B = 75\ W/m^2$.

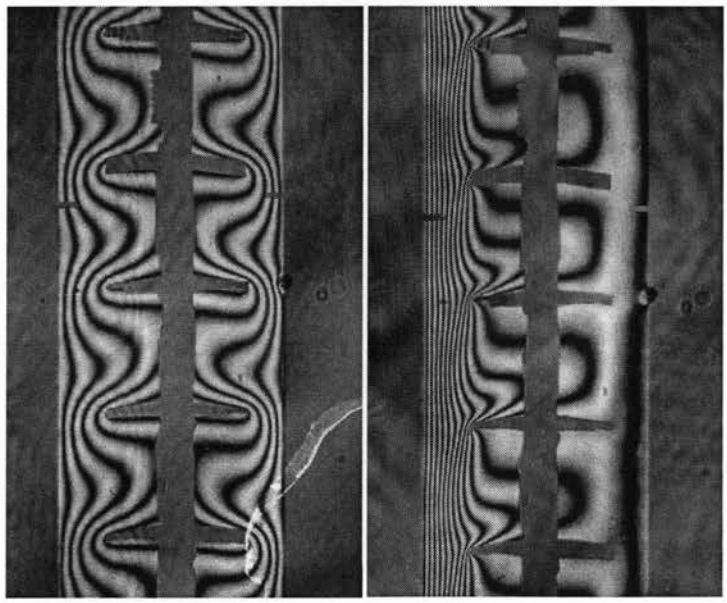

a) $\Delta T = 0°C$ b) $\Delta T = 15°C$

Figure 4.10: Infinite fringe interferogram for $\phi = 0°$, W = 40.7mm, and $q''_B = 75\ W/m^2$.

are shown. One has a blind heat flux of $q''_B = 75 W/m^2$ and the other case has a blind heat flux of $q''_B = 150 W/m^2$. The case with a blind heat flux of $q''_B = 150\ W/m^2$ has an average cold wall heat flux of $q''_C = -35.6\ W/m^2$ while the case with a blind heat flux of 75 W/m2 has an average cold wall heat flux of $q''_C = -15.3\ W/m^2$. While both cases have similar periodic variations, there is a large difference in terms of amplitude. The peaks for both cases almost overlap while the minima have a descrepency. The location of the blind slat tips correspond to the local minima of the plots.

Refering to Figures 4.12a and 4.12b, one can see that most of the temperature difference is in the boundary layer. Figure 4.12b has more total fringes than Figure 4.12a because there is a larger ΔT in the cavity. The cold wall temperature is 22 °C for both cases, but the blind temperature is 27.9 °C for the $q = 75\ W/m^2$ case and 33.8 °C for the $q = 150\ W/m^2$. There is less heat transfer in the space between the slats than there is near the slat location. At the slat location, the temperature difference between the blind and the wall becomes more evident because of the sensitivity of the heat transfer on the gap between the blind tip and wall. So, both cases approach the same heat transfer rate between the slats but there is a large difference of heat transfer rate around the blind tip.

To illustrate the effect of blind heat flux, Figure 4.13 shows results for a blind angle ϕ = 0°, a wall-to-wall temperature difference of $\Delta T = 15°C$, and a gap cavity width of W = 40.7 mm. The local heat transfer along the cold wall is shown for three cases: $q = 0\ W/m^2$, $q = 75\ W/m^2$, and $q'' = 150\ W/m^2$. The corresponding infinite fringe interferograms are shown in Figure 4.14a, 4.14b, and 4.14c, for the three heat flux cases, respectively.

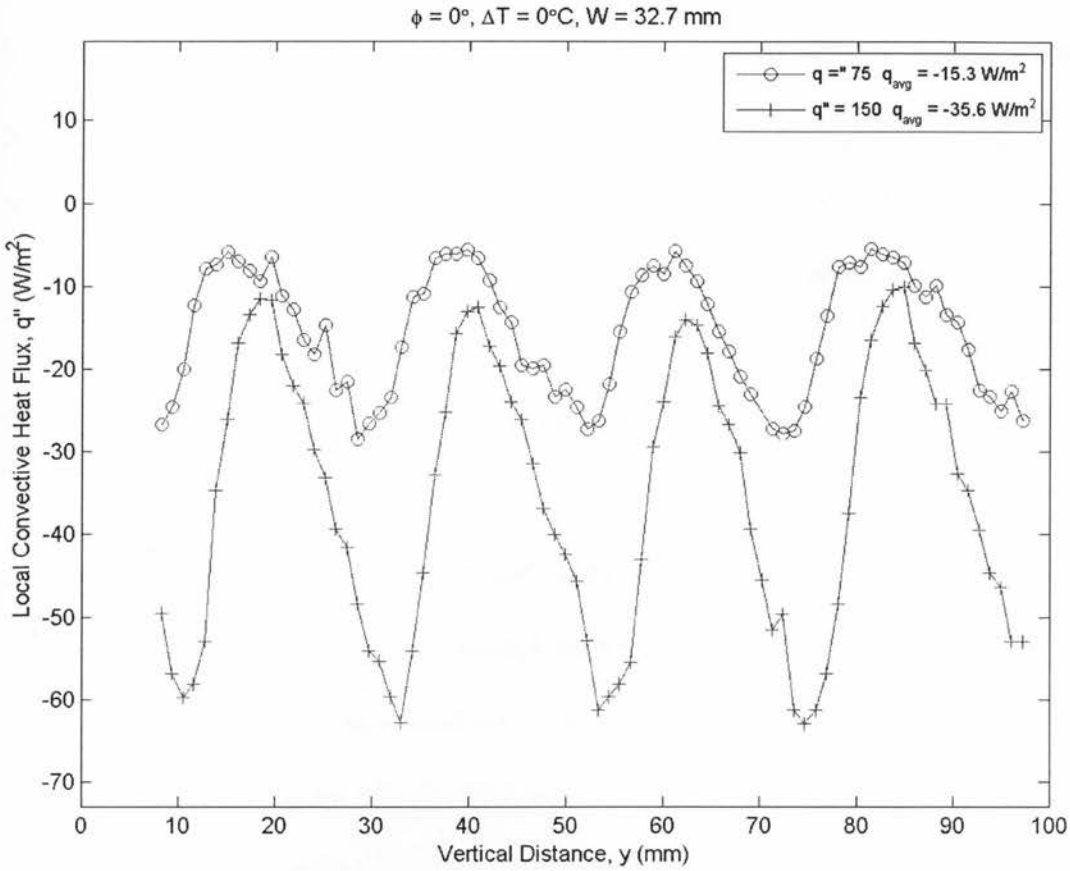

Figure 4.11: Local convective heat flux along the cold wall for $\phi = 0°$, W = 32.7mm, and $\Delta T = 0$ °C.

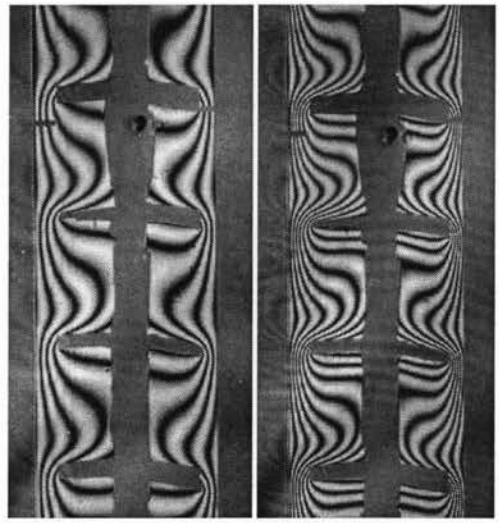

a) $q''_B = 75$ W/m^2 b) $q''_B = 150$ W/m^2

Figure 4.12: Infinite fringe interferogram for $\phi = 0°$, W = 32.7mm, and $\Delta T = 0$ °C.

First let us consider the $q''_B = 150\ W/m^2$ case, which behaves with the similar periodic variation as seen in several previous figures. The local heat transfer peaks are occuring between the blind slats. This can be seen in Figure 4.14c, which shows the greatest fringe gradient not at the blind tip but in the open space between the blind slats. This indicates a strong internal flow recirculation between the blind slat, which creates strong convective heat transfers. For the $q''_B = 75\ W/m^2$, there is also internal circulating flow which can be seen in the corresponding infinite fringe interferograms in Figure 4.14b. While not as pronounced as the $q''_B = 150\ W/m^2$ case, one can still see some small variation.

In contrast, the $q''_B = 0\ W/m^2$ case has essentially no periodic variation in local convective heat transfer. The only difference between this case and that of Figure 4.3 is that Figure 4.3 had a gap width of W=32.7mm. Here, we have a gap width of W = 40.7mm. Figure 4.3 has periodic variation of the local convective heat transfer rate, but Figure 4.13 does not. It can be assumed that for the $q''_B = 0\ W/m^2$ case, the convective effect of the internal recirculating flow and the conduction from thermal bridging effect of the blinds are in balance, giving a mostly flat distribution of the local heat transfer rates. In Figure 4.14a, one can see a uniform thermal boundary layer along both walls with the blinds having almost no effect. But most of the temperature difference is within the boundary layer between the blind tip and wall, with little temperature variation within the center portion of the cavity. Thus, the blind slats are still behaving as a thermal bridge conducting the heat away from the walls, but this is not affecting the temperature distribution along the wall surface.

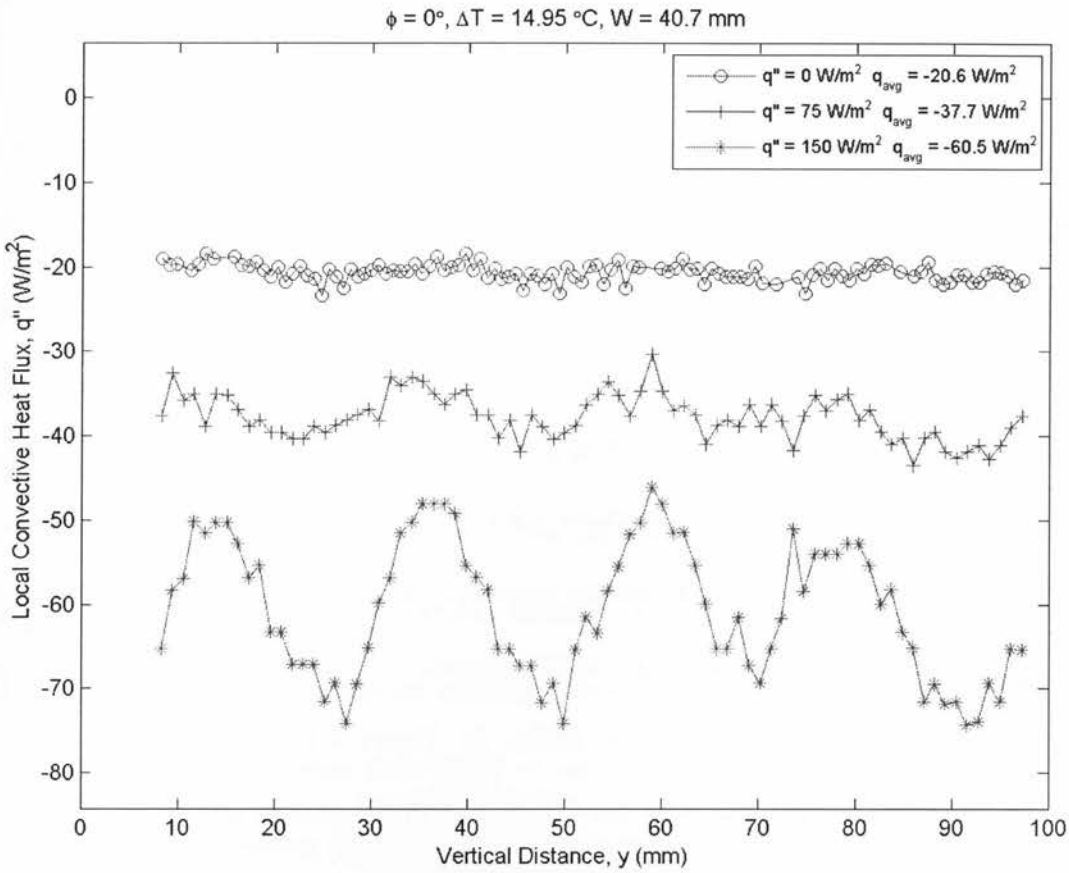

Figure 4.13: Local convective heat flux along the cold wall for $\phi = 0°$, W = 40.7mm, and $\Delta T = 15$ °C.

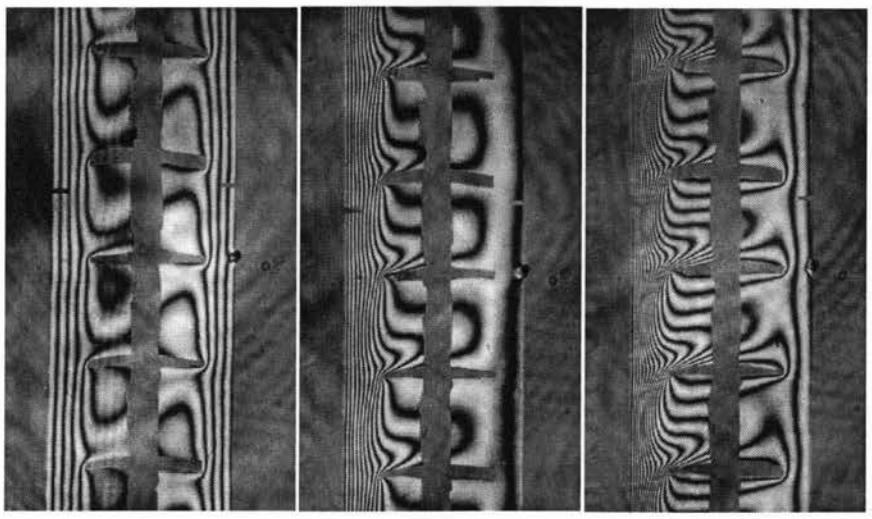

a) $q''_B = 0$ W/m^2 b) $q''_B = 75$ W/m^2 c) $q''_B = 150$ W/m^2

Figure 4.14: Infinite fringe interferogram for $\phi = 0°$, W = 40.7mm, and $\Delta T = 15$ °C.

4.2.4 Effect of Cavity Width, W

Figure 4.15 shows the effect of cavity width for a blind angle of $\phi = 0°$, a wall to wall temperature difference of $\Delta T = 0$ °C, and a blind flux of $q''_B = 150$ W/m^2. The sensitivity of the periodic variations of the local heat transfer rate to the spacing between the blind tips and the wall is clearly shown. The case with the smallest cavity width has the largest amplitude in variation. The medium spacing has a smaller periodic variation, and the largest spacing has no variation. In general, the periodic variations correspond approximately to the location of the blind tips. However, for the large and medium spacings, the locations of the peaks do not match.

The corresponding infinite fringe interferograms in Figures 4.16a and 4.16b provides some explaination for this mismatch in the peaks. In Figure 4.16a, the largest gradient, which can also be described as the area with the 'tightest' fringes, occurs just below the blind tips. While, in Figure 4.16b, the the tightest fringes are closer to the blind tip. This 'shift' of the peak heat transfer rate might be caused by a smaller secondary recirculating flow but it is not known if that is the reason. Again, flow visualization is required. Looking at Figure 4.16c, the blind slats have almost no effect on the fringes near the wall surface even with a blind heat flux of q = 150 W/m^2, and this effect can be seen in Figure 4.15 where the case with the widest spacing has little variation in the local heat transfer rate .

4.2.5 Effect of Blind Slat Angle, ϕ

The effect of blind angle is shown in Figure 4.17 for a blind heat flux of $q''_B = 0$ W/m^2, a wall-to-wall temperature difference of $\Delta T = 15$ °C and a cavity width of W = 32.7 mm. The corresponding infinite fringe interferograms are shown in Figure 4.18. The $\phi = 0°$ case has the smallest blind tip to wall distance and it has the greatest amplitude of variation and the largest average cold wall heat transfer rate of the three cases.

The $\phi = 45°$ case and the $\phi = -45°$ case do not have the same average wall heat flux because of the effect of blind slat curvature. In the $\phi = 45°$ case, the blind slat curves towards the wall; while, in the $\phi = -45°$ case the blind tip curves away. Therefore, the $\phi = 45°$ case has a smaller blind tip to wall distance than the $\phi = -45°$ case. As been discussed previously, the closer blind tip to wall spacing gives a larger amplitude in the variation of the local convective heat flux. Figure 4.18 illustrates the effect of blind curvature on the blind tip to wall spacing.

For these experiments, it was difficult to measure the amount of curvature in the slats due to two factors: 1) the electric heaters on the under surface of the blind slat tended to flatten the blind and 2) the length of the blind and added weight from the electric heaters caused the blinds to sag, further flattening the blind.

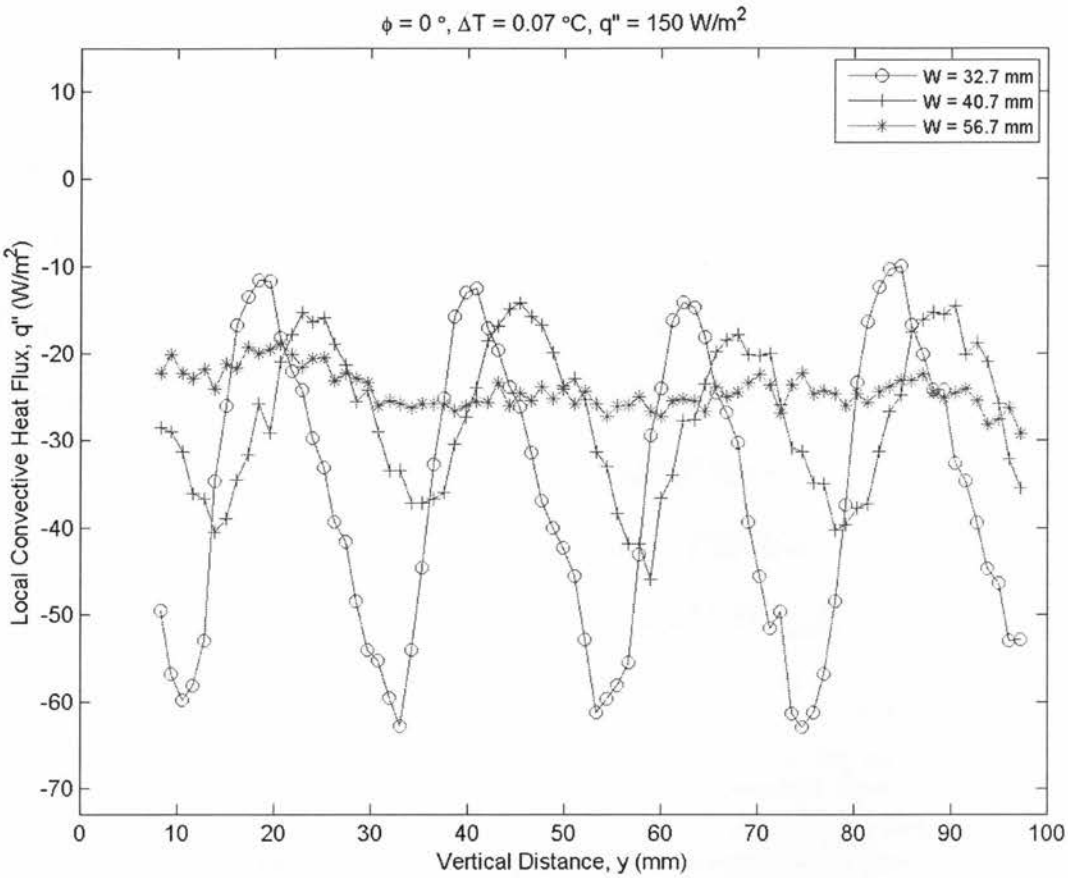

Figure 4.15: Local convective heat flux along the cold wall for $\phi = 0°$, $\Delta T = 0$ °C and $q''_B = 150$ W/m^2.

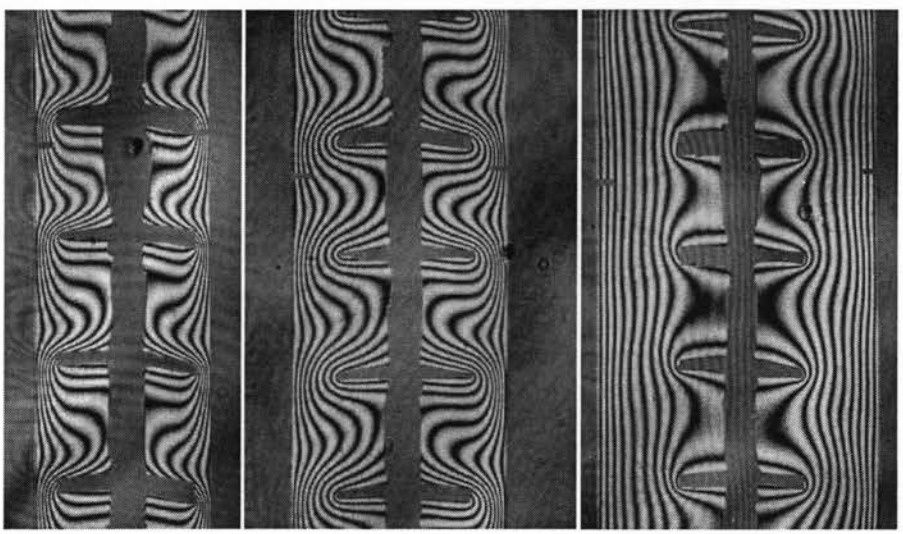

a) W = 32.7 mm b) W = 40.7 mm c) W = 56.7 mm

Figure 4.16: Infinite fringe interferogram for $\phi = 0°$, $\Delta T = 0$ °C, and $q''_B = 150$ W/m^2.

4.3 Average Convective Heat Transfer Results and Comparison with the RSL Model

The average convective heat transfer measured in the present experiment was compared to the simplified model developed by Collins et al. (2008) at the University of Waterloo. The model is called the Reduced Slat Length (RSL) model and is explained in detail in Section 1.7.

The average centre-glass convective heat flux measurements are shown in Tables 1 and 2. Due to the size of the data, only a subset of the results will be shown in this section. The complete data set is shown in Appendix D. Table 4.1 reports the results for the cold (left) wall. Table 4.2 contains the data for the hot (right) wall. In both tables, comparisons are made between the measured heat flux and the heat flux predicted using the RSL model. It can be seen that the RSL model gives very close agreement in some cases and poor agreement in others. Some of the reasons for this "mixed" performance will be discussed next.

Referring to Table 1 and Table 2, it can be seen that the RSL model performs the poorest at the widest wall spacing (W_G=56.7mm) when there is a temperature difference of 15°C across the enclosure. These are experiments "B", "C", "E" and "F" in Table 1 and Table 2. For these cases, the RSL model consistently underpredicts the convective heat flux, by as much as 40% on the hot wall and by as much as 86% on the cold wall. The main reason for the poor performance of the RSL model is almost certainly the presence of a highly unsteady (and possibly fully turbulent) flow.

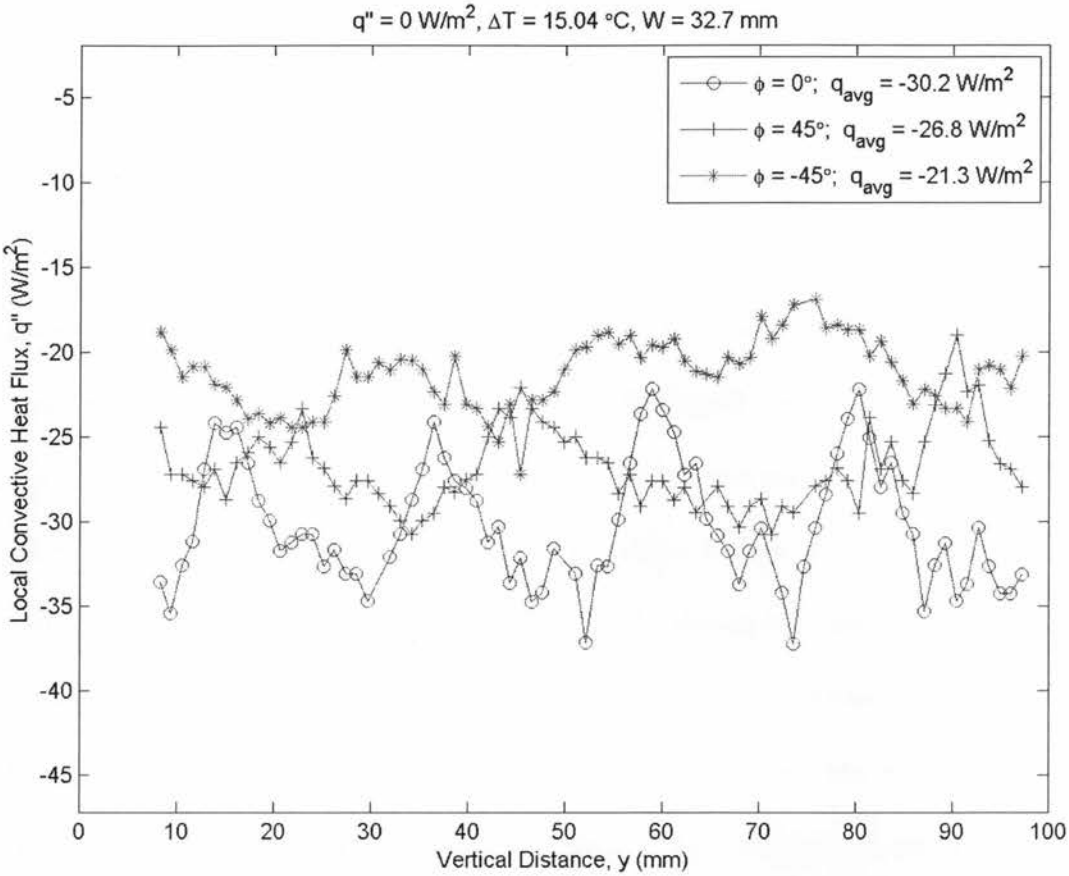

Figure 4.17: Local convective heat flux along the cold wall for $\Delta T = 15$ °C, W = 32.7 mm, and $q''_B = 0$ W/m^2.

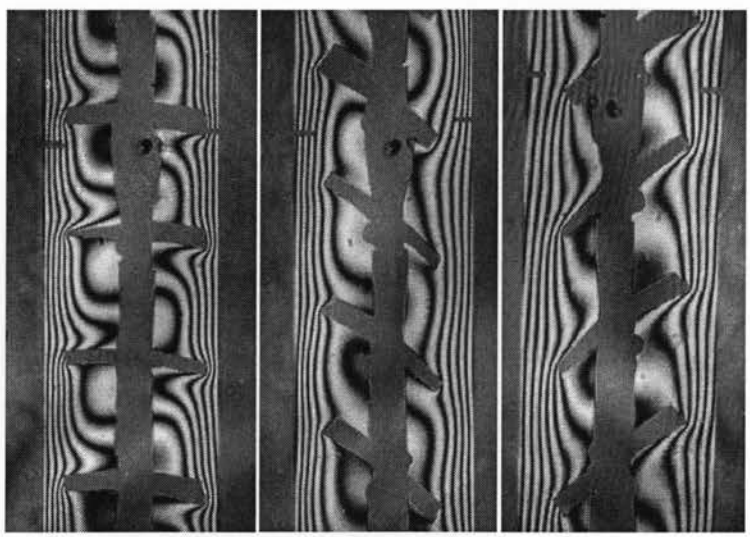

a) $\phi = 0°$ b) $\phi = 45°$ c) $\phi = -45°$

Figure 4.18: Infinite fringe interferogram for $\Delta T = 15$ °C, W = 32.7 mm, and $q''_B = 0$ W/m^2.

Table 4.1: Cold wall centre-glass heat transfer results.

Exp.	Blind Flux q''_B (W/m^2)	Slat Angle ϕ (deg.)	Glazing Spacing W_G (mm)	T_H-T_C (°C)	Blind Temp. (°C)	Exp. Heat Flux, q''_C (W/m^2)	RSL Model Heat Flux (W/m^2)	% Diff.	Sub-cavity Ra'	Sub-cavity Nu'
A	75.0	0	56.7	0.04	30.3	-12.0	-12.2	1%	6.0E3	1.09
B	0.0	0	56.7	15.07	23.0	-17.6	-11.1	37%	6.2E3	1.10
C	74.9	0	56.7	15.00	31.2	-32.5	-27.6	15%	1.2E4	1.34
D	75.0	45	56.7	0.00	28.3	-10.5	-10.2	3%	8.0E3	1.17
E	0.0	45	56.7	15.01	22.7	-17.5	-10.4	40%	8.8E2	1.21
F	75.0	45	56.7	14.99	29.5	-38.1	-24.4	36%	1.5E4	1.50
G	75.0	0	32.7	0.00	28.0	-	-19.7	-	2.5E2	1.00
H	0.0	0	32.7	15.04	22.7	-30.6	-25.4	17%	3.6E2	1.00
I	75.0	0	32.7	15.00	28.5	-52.3	-44.2	15%	5.9E2	1.00
J	75.0	45	32.7	-0.03	26.2	-16.0	-13.9	13%	5.8E2	1.00
K	0.0	45	32.7	15.01	22.2	-26.6	-17.7	34%	8.0E2	1.00
L	75.0	45	32.7	14.99	28.3	-47.3	-32.2	32%	1.4E3	1.00

Table 4.2: Hot wall centre-glass heat transfer results

Exp.	Blind Flux q''_B (W/m^2)	Slat Angle ϕ (deg.)	Glazing Spacing W_G(mm)	T_H-T_C (°C)	Blind Temp. (°C)	Exp. Heat Flux, q''_C (W/m^2)	RSL Model Heat Flux (W/m^2)	% Diff.	Sub-cavity Ra'	Sub-cavity Nu'
A	75.0	0	56.7	0.04	30.3	-12.4	-12.1	3%	6.0E3	1.09
B	0.0	0	56.7	15.07	23.0	19.1	10.4	46%	5.2E3	1.06
C	74.9	0	56.7	15.00	31.2	-	-0.85	-	4.2E2	1.00
D	75.0	45	56.7	0.00	28.3	-10.8	-10.2	6%	8.0E3	1.17
E	0.0	45	56.7	15.01	22.7	23.6	10.3	57%	7.9E3	1.17
F	75.0	45	56.7	14.99	29.5	8.5	1.23	86%	1.0E3	1.00
G	75.0	0	32.7	0.00	28.0	-19.3	-19.7	2%	2.5E2	1.00
H	0.0	0	32.7	15.04	22.7	29.9	25.5	15%	3.1E2	1.00
I	75.0	0	32.7	15.00	28.5	-	6.56	-	7.6E1	1.00
J	75.0	45	32.7	-0.03	26.2	-14.7	-13.9	5%	5.8E2	1.00
K	0.0	45	32.7	15.01	22.2	28.2	20.4	28%	8.0E2	1.00
L	75.0	45	32.7	14.99	28.3	-	5.84	-	2.2E2	1.00

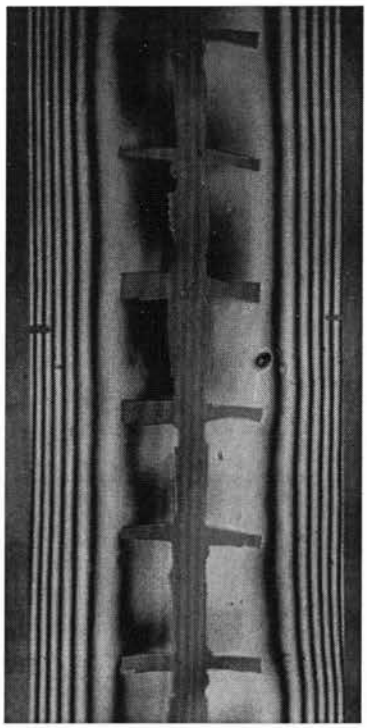

Figure 4.19: Infinite fringe interferogram for $\phi = 0$, W = 56.7mm, $q''_B = 0$ W/m^2, and ΔT = 15 °C.

For these wide wall spacings, the enclosure Rayleigh number was high (Ra=2.7x10^5) and significant temporal fluctuations were observed during the experiment in the real-time interference patterns. The interferogram in Figure 4.19 clearly shows the formation of thermal boundary layers on the enclosure walls, which are likely turbulent. This appears to be far from the conditions that are required by the RSL model. As stated by Wright et al. (2008), "the overiding point to be made is that the RSL model works well when the primary gas flow is well-behaved, i.e., laminar and largely parallel to the vertical cavity walls – free of instabilities." So, it is not surprising that the RSL predictions are poor under these conditions.

Even at the narrower glazing spacing (W_G=32.7mm), when a temperature difference of 15°C is maintained across the enclosure, there are significant departures between the

measurements and the RSL model. The corresponding experiments are labeled "H", "I", "K" and "L" in Tables 1 and 2. Again, this is likely due to flow instabilities. Even though this spacing is a more realistic geometry for an actual window, the Rayleigh is still quite high ($Ra=5.3x10^4$). So, there is likely still some instability in the flow for these conditions. As a result, the RSL model consistently under-predicts the convective heat flux -- but by not as much as for the wider spacing (typically by 15-30%).

It should be mentioned that at the narrow spacing, the presence of flow instabilities was less obvious in the real-time interference patterns. So, this conjecture remains to be confirmed by flow visualization experiments.

Perhaps the most interesting and surprising results were found for the cases where the blind was heated, and both walls of the enclosure were held at the same temperature. The corresponding experiments are labeled "A", "D", "G" and "J" in Tables 1 and 2. These experimental cases are all *very closely* predicted by the RSL model. Even at the widest glazing spacing, the RSL model predicts the heat flux to better than 6% on both walls! To understand this behavior, consider the interferogram of case ''A'' shown in Figure 4.20. In this Figure, there is no temperature difference between the glazings, and the blind heat flux is 75 W/m^2. Also, it is evident that there is much less flow. The isotherms between the glazings and the blind tips are more uniformly spaced, suggesting that conduction plays a stronger role under these conditions. This suggests that heating from the centre of the enclosure produces a weaker and more stable flow than heating from one side of the enclosure. These are precisely the conditions where the RSL model is expected to perform well.

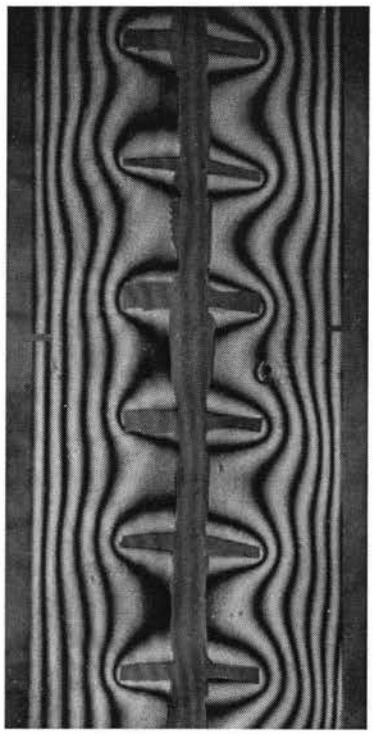

Figure 4.20: Infinite fringe interferogram for $\phi = 0$, W = 56.7mm, $q''_B = 75$ W/m^2 and $\Delta T = 0$ °C.

Another useful observation can be made by examining the last two columns in Table 1 and Table 2. These columns provide the "subcavity" Rayleigh number (Ra') and "subcavity" Nusselt number (Nu'), corresponding to the RSL model. It has been suggested by Wright et al. (2008) that these subcavity parameters might be used as an indicator of whether the RSL model can be applied. Using experimental data from a mini-blind, Wright et al. (2008) get accurate predictions with the RSL model for subcavity Rayleigh numbers up to about Ra'=1500. However, in the current experiments, we find that this parameter is, by itself, not a useful indicator. When the glazings were held at a temperature difference of 15 °C, we found that the RSL model gave consistently poor predictions at subcavity Raleigh numbers much lower than 1500. However, when the blind was heated and the glazings were held at equal constant temperature, we got excellent predictions from the RSL model even at Ra'=8000! So, it appears

that more detailed criteria are needed to predict the onset of flow instabilities (and hence, the range of applicability for the RSL model). As discussed in the Recommendations section, further research is needed to delineate the flow structures and to investigate the criteria for the onset of flow instabilities.

4.4 Reproducibility

A reproducibility test was done on one of the experiments to determine the inherent error in the experimental system and procedure. The experiment chosen had a width of W = 32.7 mm and blind angle of $\phi = 0°$, a glazing to glazing temperature difference of $\Delta T = 0$ °C and a blind heat flux of $q''_B = 150$ W/m^2. This experiment was repeated after a delay of several days. The results of the reproducibility test are shown in Figure 4.21.

Figure 4.21 shows the local heat transfer rates along the vertical glazing for the original test and the reproducibility test. The majority of the data overlaps with each other indicating good agreement. Also, the average convective heat transfer rates are very close to each other with the original test at $q''_{avg} = -42.5$ W/m^2 and the reproducibility test at $q''_{avg} = -43.1$ W/m^2. Both the peaks and valleys of the reproducibility test are slightly shifted to the left of the figure (down along the vertical glazing). This is probably due to a slight misalignment of the blinds which are difficult to set. The largest discrepancy appears to be in the valleys of the graph, which corresponds to the location of the blind slats. This is expected because, as discussed previously, the heat transfer results are sensitive to the distance between the blind tips and wall. A full experimental uncertainty analysis is performed in Appendix B. The uncertainty in the local heat flux is shown to be ±5.7%.

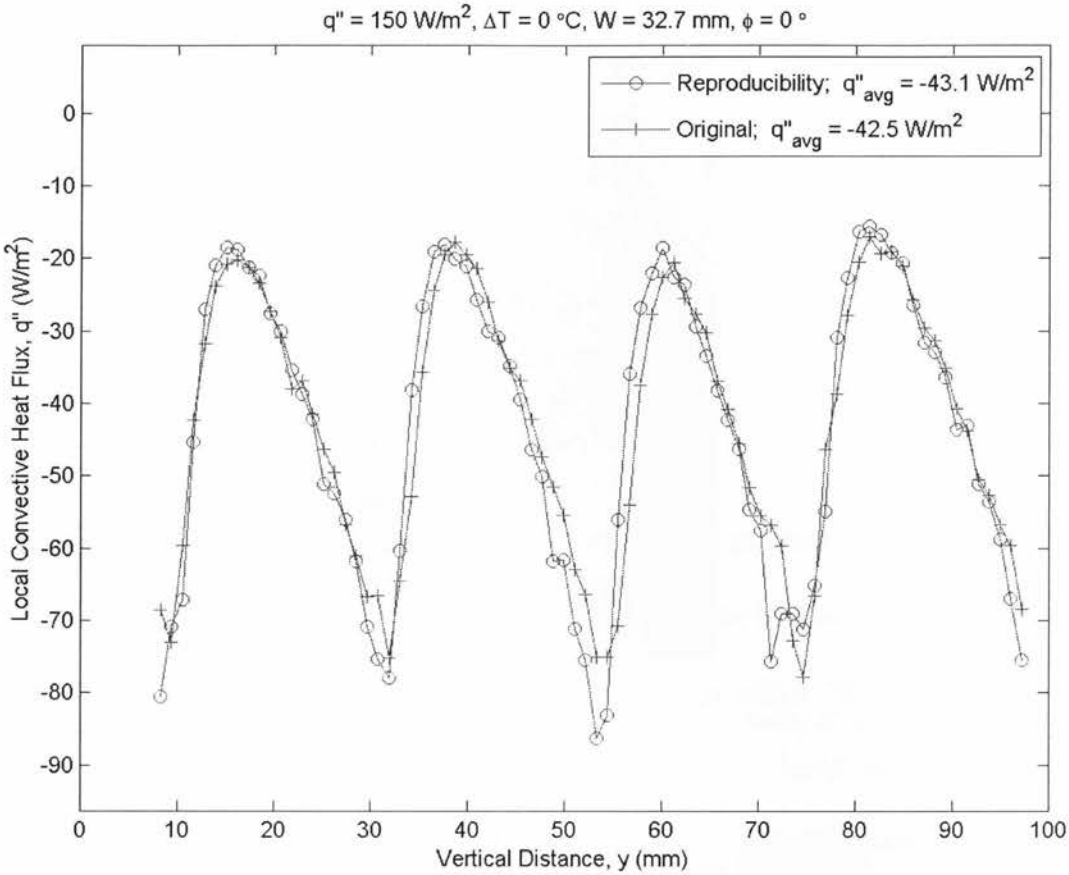

Figure 4.21: Local convective heat flux along the cold wall for $\phi = 0$, W = 32.7 mm, q''_B = 150 W/m^2 and $\Delta T = 0$ °C.

Chapter 5: Conclusions and Recommendations

5.1 Conclusions

An experimental study was performed to measure the convective heat transfer in a window with a heated between-panes venetian blind. Temperature field visualization and convective heat transfer measurements were obtained using laser interferometry. Infinte fringe interferograms were used to obtain a temperature field visualization, while finite fringe interterferograms were used for the heat transfer analysis. The results have been compared to a simplified model from the literature, the Reduced Slat Length (RSL) model. The main findings are summarized as follows:

1) The infinite fringe interferograms show that the temperature field is greatly affected by the presence of the blind in the centre-glass region.

2) The blinds themselves are highly conductive and, for most cases, the majority of the temperature change (i.e., thermal resistance) is in the wall-to-blind tip region. This indicates that the louvers act as thermal bridges, conducting heat away from the walls.

3) In many cases, especially at narrow plate spacings, there was a periodic variation of the heat flux along the plate surface. In general, the peaks of the variation correspond to the location of the louver tips. These peaks are caused by the conductive blinds.

4) In a few cases, large blind heat flux created strong internal flow recirculation between the louvers. This effect caused the peaks of the local heat flux to be at the midpoint between the louvers instead of near the louver tips.

5) Increasing the gap spacing reduced the sensitivity of the blinds on the local convective heat transfer rates along the wall. This result agrees with previous studies, which indicate that the blind tip-to-wall spacing increases the sensitivity of the heat flux along the wall.

6) Related to the above point, as the gap width between the plates increases, the effect of blind angle decreased. At the largest gap width, the blind angle had almost no effect on the local heat flux distribution along the walls.

7) For smaller gap widths, the average heat flux for the $\phi = 45^{o}$ and ϕ -45° cases were not equal due to the effect of blind curvature. The curvature of the blind makes one tip of the louver marginally closer to the wall, while the other tip is marginally further away.

8) At the widest glazing spacing, evidence of highly unsteady/turbulent flow was observed when a temperature difference of $15^{o}C$ was imposed across the enclosure. As might be expected, under these conditions, the RSL model gave poor predictions of the convective heat flux for all slat angles.

9) In constrast to the above conclusion, when the blind was heated with the glazings at the same temperature, the primary flow appeared to be laminar, steady and parallel to the glazings, even at the widest glazing spacing. Under these conditions, the lateral

convective heat transfer was dominated by conduction and the RSL model performed very well.

10) Overall, the RSL model was found to perform well, within the stated limitations of this model. However, the current results show that the main difficulty in applying the RSL model lies in determining, with confidence, whether the flow field is sufficiently stable. For the larger blind slats used in the present experiment, the model's "subcavity" Rayleigh number was found to be a poor indicator of flow stability.

5.2 Recommendations

The following recommendations are made for future studies:

1) Smoke flow visualization is needed to determine, more accurately, the flow regime for various parameters. While some evidence of turbulence was observed visually in the interferometer output, a more definite method of determining the onset of turbulent conditions would be useful. Also, smoke flow visualization would reveal the flow structure, which would aid in the basic understanding of the problem.

2) Improved and/or additional correlations would be beneficial. At present a simplified model exists (the RSL model) but it does not work in all cases.

3) A time averaged interferometric technique is needed. The present study mainly considered steady state phenomena, due to the nature of the interferometric technique used. The apparatus as designed can achieve unsteady/turbulent flow. However, accurate measurements cannot be made from a single "snap shot" under these conditions.

4) Continued improvement to the current image processing software would be useful. For example; developing a better algorithm to extract the fringe centers, incorporating a method to digitally clean erroneous data (like optical imperfections), and a better way of determining the error associated with the digital analysis.

5) It would be useful to perform the heat transfer measurements along the entire cavity. The current study only considered the center glass region. It might be useful to consider the entire cavity to see the effect of turbulence on the convective heat transfer rate of the window.

6) Moving to an all digital analysis procedure would make the analysis easier and faster. For the current study, the interferograms were captured on Polaroid film, and then scanned into the computer. Some resolution was lost and noise was added during the scanning. A digital capture system would improve the accuracy of the results.

7) During the post processing of the results, it was discovered the post which holds the blinds in place bows slightly to one wall. If the model is to be reused in future experiments, it is recommended to place a precision machined block between the post and wall, out of site of the camera.

Appendix A: Image Processing

Custom made image processing software was developed to perform the heat transfer analysis. The interferogram photographs were scanned into the computer and saved as a 8 bit grayscale TIFF image. By doing this, the image was easily manipulated by realizing that the image becomes discretized. The image can be viewed as a matrix with each pixel of the image being an element of a matrix. Within each matrix cell a grayscale value between 0 and 255 is stored to represent the light intensity (i.e., 0 is for black, 255 is for white).

For the present analysis there are two main components to the image processing software: 1) reading the image file, 2) extracting the fringe centers. These two components will be discussed next.

A.1 The read.m file

In this file, the interferogram image is filtered using a 2-D median filter to reduce noise in the data (Matlab 2008). Also, the user provides the 'x' and 'y' location of the wall, scaling pins, and location of analysis. Note that the 'x' and 'y' are in the units of pixels, with the origin being the top left corner of the image. The matlab code for this portion of the image processing is shown here.

```
function [I,expnum,wallimg]=read(expnum,wallimg,cavity)

% expnum = input('Enter experiment number [1 2 3 ... 46 47]:  ');
% wallimg = input('Enter wall label [A/B]:  ','s');
% cavity = input('Is it a cavity? [y/n]:  ','s');
% read image and display
%J=imread(['Interferograms/' files(filenum).name]);
% Apply a 2d median filter twice to reduce "point noise"
J = imread(['Exp',int2str(expnum),'/Wall',wallimg,'.tif']);
I2=medfilt2(J);
```

```
I=medfilt2(I2);
% open a figure in column 2 (in figure with 2 colums 1 row)
%subplot(1,2,1)
% show filtered image in column 2 of subplot
imshow(I)
% display filtered imaged in a tool window
imtool(I)
```

A.2 The centre.m file

Once the image is filtered and saved as a TIFF, the analysis can be performed. Due to its better accuracy, all the heat transfer results are done on the finite fringe interferograms (for a detailed explanation of finite and infinite fringe interferograms, please refer to section 3.2). For finite fringe interferograms, the analysis can be done in same manner as for infinite interferograms. By treating the TIFF image file as a matrix, then the rows of the matrix can be extracted to get the light intensity variation normal to the plate. This 'row' of intensity values will contain peaks that correspond to constructive fringes and minima that correspond to destructive fringes. This program can determine the position of the peaks by extracting its location from the matrix. With the location of the peaks known, the calculation procedure explained in chapter 3 can then be used to get the heat transfer rates.

```
function [con, des] = centre(ln)
% con = 0;
% des = 0;
countcon = 1;
countdes = 1;
avg=mean(ln);
%mean pixel intensity avI
avI=avg(1,3);
% number of rows Nx3 array ln
N=length(ln);
% initialize counters & arrays
xu=[];
xd=[];
iu=[];
id=[];
ku=0;
```

```
kd=0;
for i=1:N-1
    % check for intensity profile crossing mean upwards
    if ln(i,3)<avI & ln(i+1,3)>avI
        ku=ku+1;
        iu(ku)=i;
        xu(ku)=ln(i,1);
    end
end

for i=1:N-1
    % check for intensity profile crossing mean downwards
    if ln(i,3)>avI & ln(i+1,3)<avI
        kd=kd+1;
        id(kd)=i;
        xd(kd)=ln(i,1);
    end
end
% count the number of fringes
if xd(1)<xu(1)
    NumConst=kd-1;
    NumDest=ku;
end
if xd(1)>xu(1)
    NumConst=kd;
    NumDest=ku-1;
end

% find and print out the fringe centres w/ 1st crossing downward
%
% Destructive Interference fringe centre locations
Imin=255.;
xmin=0.0;
if xd(1)<xu(1)
    for j=1:NumDest
        for i=id(j):iu(j)
            if ln(i,3)<Imin
                Imin=ln(i,3);
                xmin=ln(i,1);
                ymin = ln(i,2);
            end
        end
        des(countdes,1) = xmin;
        des(countdes,2) = ymin;
        des(countdes,3) = Imin;
        countdes = countdes +1;
        Imin=255.;
    end

end
%
% Constructive Interference fringe centre locations
Imax=0.;
xmax=0.0;
if xd(1)<xu(1)
    for j=1:NumConst
```

```
        for i=iu(j):id(j+1)
            if ln(i,3)>Imax
                Imax=ln(i,3);
                xmax=ln(i,1);
                ymax = ln(i,2);
            end
        end

        con(countcon,1) = xmax;
        con(countcon,2) = ymax;
        con(countcon,3) = Imax;
        countcon = countcon +1;
        Imax=0;
    end
end
% find and print out the fringe centres w/ 1st crossing upward
%
% Destructive Interference fringe centre locations
Imin=255.;
xmin=0.0;
if xd(1)>xu(1)
    for j=1:NumDest
        for i=id(j):iu(j+1)
            if ln(i,3)<Imin
                Imin=ln(i,3);
                xmin=ln(i,1);
                ymin = ln(i,2);
            end
        end
        des(countdes,1) = xmin;
        des(countdes,2) = ymin;
        des(countdes,3) = Imin;
        countdes = countdes +1;
        Imin=255.;
    end
end
% Constructive Interference fringe centre locations
Imax=0.;
xmax=0.0;
if xd(1)>xu(1)
    for j=1:NumConst
        for i=iu(j):id(j)
            if ln(i,3)>Imax
                Imax=ln(i,3);
                xmax=ln(i,1);
                ymax = ln(i,2);
            end
        end
        con(countcon,1) = xmax;
        con(countcon,2) = ymax;
        con(countcon,3) = Imax;
        countcon = countcon +1;
        Imax=0;
    end
end
end
```

Appendix B: Experimental Uncertainty Analysis

B.1 Introduction

The results from the Mach-Zehnder Interferometer (MZI) have a degree of uncertainty from a variety of sources. One of the earliest works involving a MZI to make convective heat transfer measurements was the research of Machin (1997). A detailed description of probable sources of error can be found in Machin's thesis (1997).

All results were done on the finite fringe mode for the experimental case of a gap width of W = 40.7 mm, a plate to plate temperature difference of $\Delta T = 15$ °C, blind angle of $\phi = 0$ °, and a blind heat flux $q_B'' = 75$ W/m^2. This case was chosen because it represents typical experimental parameters and offers a range of variables to investigate the errors of the measurements.

In the finite fringe mode, the fringes are set in a horizontal position while the model is unheated. When the model is heated, these fringes bend up in areas of increasing temperature and bend down in areas of decreasing temperature. The accuracy of these fringe bends can be affected by any misalignment of the optics. This misalignment would create an artificial fringe gradient resulting in a fringe shift error.

The digital image processing techniques contain new kinds of errors not found in previous analog image analysis procedures. The main measurement made by the image processing software is the number of pixels between two consecutive fringe peaks. Each fringe peak could be off by one pixel giving a maximum error of two pixels. One pixel equals 0.0142

mm nominally giving the error in the peak to peak distance as 0.028 mm. By observation, due to the 'noise' in the data, there is an additional pixel worth of potential error. Thus, the total fringe peak to peak error is 0.042 mm.

To quantify the fringe shift error ($\delta\varepsilon$), the following expression was derived from the geometry of the problem:

$$\delta\varepsilon = \pm\frac{\Delta x}{d}\tan\Psi \tag{B.1}$$

Where Δx is the fringe distance between two consecutive fringes, d is the fringe spacing, and Ψ is the fringe misalignment relative to the horizontal. Before every experiment, the finite fringe interferograms were set at a spacing of d = 1 mm while the model was unheated. By inspection, it was determined that the maximum the fringe alignment could be off by is approximately $\varphi = 1°$. With all of these parameters known, the fringe shift error was calculated to be ±0.014. A summary of the uncertainties and the propagated errors are shown in Table B.1.

Table B.1 Uncertainty in measured quantities

Quantity	**Uncertainty**	$\left(\partial R/_{\partial x_1}\right)w_1$
Ambient pressure δP	±66.64 Pa	±0.0261 W/m^2
Plate surface Temp δT_{REF}	±0.02 K	±0.1097 W/m^2
Optical length of plate δZ	±0.005 m	±0.3575 W/m^2
Fringe distance $\delta\Delta x$	±0.000028 m	±2.0445 W/m^2
Fringe shift $\delta\varepsilon$	±0.014	±0.5475 W/m^2

The experimental uncertainty was determined by using the methods of Kline and McClintock (1953). This method assumes that all the uncertainties have the same odds of occurring. Given the result R is a function of n independent variables, $x_1, x_2, x_3, \ldots, x_n$ then;

$$R = R(x_1, x_2, x_3, \ldots, x_n) \tag{B.1}$$

And letting w_R be the uncertainty of R and w_1, w_2, w_3,…,w_n be the uncertainty of the independent variables, then the uncertainty of R can be expressed as follows:

$$w_R = \left[\left(\frac{\partial R}{\partial x_1} w_1\right)^2 + \left(\frac{\partial R}{\partial x_2} w_2\right)^2 + \cdots + \left(\frac{\partial R}{\partial x_n} w_n\right)^2\right]^{1/2} \tag{B.2}$$

B.2 Uncertainty in the Local Convective Heat Flux

From section 3.4, the formulation to determine the fringe temperature is given by:

$$T = \frac{T_{REF}}{1 \pm \frac{\varepsilon R \lambda T_{REF}}{GPZ}} \tag{B.3}$$

And the fringe temperature difference between two consecutive constructive or destructive fringes is given by:

$$\Delta T = T_1 - T_2 = \frac{T_{REF}}{1 - \frac{\varepsilon_1 R \lambda T_{REF}}{GPZ}} - \frac{T_{REF}}{1 - \frac{\varepsilon_2 R \lambda T_{REF}}{GPZ}} \tag{B.4}$$

In equation B.4, a negative sign was chosen in the denominator for simplicity. The negative sign assumes that the fringe temperature is hotter than the reference temperature or, in other words, the fringes are in an area of decreasing density. To further simplify the analysis, ε_1 will be assumed to be zero giving:

$$\Delta T = T_1 - T_2 = T_{REF} - \frac{T_{REF}}{1 - \frac{\varepsilon_2 R\lambda T_{REF}}{GPZ}} \tag{B.5}$$

The temperature gradient can be expressed as follows by assuming a linear interpolation:

$$\frac{dT}{dx} = \frac{\Delta T}{\Delta x} = \frac{T_{REF} - \frac{T_{REF}}{1 - \frac{\varepsilon_2 R\lambda T_{REF}}{GPZ}}}{\Delta x} \tag{B.6}$$

Substituting equation B.6 into equation 3.2, the expression for the local convective heat flux is given as:

$$q'' = -k_S \frac{dT}{dx} = -k_S \left(\frac{T_{REF} - \frac{T_{REF}}{1 - \frac{\varepsilon_2 R\lambda T_{REF}}{GPZ}}}{\Delta x} \right) \tag{B.7}$$

Using the description in section B.1, an expression for the error in the local convective heat flux can be determined. Applying equation B.2 to equation B.6 gives:

$$w_{q''} = \left[\left(\frac{\partial q''}{\partial P} \delta w_P \right)^2 + \left(\frac{\partial q''}{\partial Z} \delta w_Z \right)^2 + \left(\frac{\partial q''}{\partial T_{REF}} \delta w_{T_{REF}} \right)^2 + \left(\frac{\partial q''}{\partial \Delta x} \delta w_{\Delta x} \right)^2 + \left(\frac{\partial q''}{\partial \varepsilon_2} \delta w_{\varepsilon_2} \right)^2 \right]^{1/2} \tag{B.8}$$

The following equations are the expressions for the various partial derivatives in equation B.6. These partial derivatives were determined using Maple12 (2008).

$$\frac{\partial q''}{\partial P} = -\frac{k_S T_{REF}^2 \varepsilon_2 R\lambda}{\left(1 - \frac{\varepsilon_2 R\lambda T_{REF}}{ZPG}\right)^2 ZP^2 G\Delta x} \tag{B.9}$$

$$\frac{\partial q''}{\partial Z} = -\frac{k_S T_{REF}^2 \varepsilon_2 R\lambda}{\left(1 - \frac{\varepsilon_2 R\lambda T_{REF}}{ZPG}\right)^2 Z^2 PG\Delta x} \tag{B.10}$$

$$\frac{\partial q''}{\partial T_{REF}} = -\frac{k_S\left(1 - \frac{1}{1 - \frac{\varepsilon_2 R\lambda T_{REF}}{ZPG}} - \frac{T_{REF}\varepsilon_2 R\lambda}{\left(1 - \frac{\varepsilon_2 R\lambda T_{REF}}{ZPG}\right)^2 ZPG}\right)}{\Delta x} \tag{B.11}$$

$$\frac{\partial q''}{\partial \Delta x} = \frac{k_s\left(T_{REF} - \frac{T_{REF}}{1 - \frac{\varepsilon_2 R\lambda T_{REF}}{ZPG}}\right)}{\Delta x^2} \tag{B.12}$$

$$\frac{\partial q''}{\partial \varepsilon_2} = -\frac{k_S T_{REF}^2 R\lambda}{\left(1 - \frac{\varepsilon_2 R\lambda T_{REF}}{ZPG}\right)^2 ZPG\Delta x} \tag{B.13}$$

Using equations B.8 through B.13, the uncertainties in table B.1, and the experimental parameters discussed above, the experimental error can be determined. The uncertainty in the local convective heat flux was found to be approximately 5.7%.

Appendix C: Sample Calculation

A sample calculation is done for the finite fringe interferogram for the case of a gap width of W = 40.7 mm, plate to plate temperature difference of ΔT = 15 °C, blind angle of ϕ = 0°, and a blind heat flux of q_B'' = 75 W/m^2. A summary of the parameters used for the calculation is shown in Table C.1.

Table C.1 Given data

Parameter	Value
Gladstone-Dale constant, G	0.226 x10^{-3} m^3/kg
Wavelength of He-Ne laster, λ	6.328 x 10^{-7} m
Gas Constant, R	287 J/kg·K
Ambient pressure, P	99 945 Pa
Cold wall temperature, T_C	288.82 K
Hot wall temperature, T_C	303.36 K
length of model in light beam direction, Z	0.547 m

C.1 Air Properties

Film temperature, T_f

$$T_f = \frac{1}{2}\left[\frac{1}{2}(T_C + T_H) + T_B\right]$$

$$= \frac{1}{2}\left[\frac{1}{2}(288.82 + 303.36) + 303.3453\right]$$

$$= 299.81\ K$$

Volumetric expansion coefficient, β

$$\beta = \frac{1}{T_f}$$

$$= \frac{1}{299.81}$$

$$\beta = 0.0033 \ {}^{1}/_{K}$$

Density, ρ

Using the ideal gas law:

$$\rho = \frac{P}{RT_f}$$

$$\rho = \frac{99945}{287 \times 299.81}$$

$$\rho = 1.1615 \ kg/m^3$$

Dynamic viscosity, μ

Using Touloukian and Makita (1975) evaluated at the film temperature:

$$\mu = 1.852 \times 10^{-5} \ kg/m \cdot s$$

Thermal conductivity using the surface temperature, k_S

Using Touloukian and Makita (1975) evaluated at the film temperature:

$$k_S = 0.0253 \ W/m \cdot K$$

Specific heat, c_P

Using Touloukian and Makita (1975) evaluated at the film temperature:

$$c_P = 1.0063 \ \times 10^3 \ J/kg \cdot K$$

C.2 Heat Transfer

Scale Factor, SF

Using image processing software, the location of the scaling pins was determined in units of pixel.

$$SF = \frac{pin\ distance}{|y_{pin1} - y_{pin2}|}$$

$$SF = \frac{0.075}{|4.8826 \times 10^3 - 1.016 \times 10^4|}$$

$$SF = 1.4211 \times 10^{-5}\ m/pixel$$

First fringe, f1

The image processing software determines the fringe peaks in units of pixel.

$$f_1 = x_{pixel1} \times SF - x_{wall}$$

$$f_1 = (3.4360 \times 10^2)(1.4211 \times 10^{-5}) - 0.0029$$

$$f_1 = 0.001965\ m$$

Second fringe, f2

$$f_2 = x_{pixel2} \times SF - x_{wall}$$

$$f_2 = (4.0479 \times 10^2)(1.4211 \times 10^{-5}) - 0.0029$$

$$f_1 = 0.002835\ m$$

Fringe distance, Δx

$$\Delta x = f_2 - f_1$$

$$\Delta x = 0.002835\ - 0.001965$$

$$\Delta x = 8.6956 \times 10^{-4}$$

Fringe shift, ε

The first fringe shift (ε_1) was determined by linear interpolation:

$$\frac{\varepsilon_1}{\Delta\varepsilon} = \frac{f_1}{\Delta x}$$

$$\varepsilon_1 = \frac{0.002835}{8.6956 \times 10^{-4}}$$

$$\varepsilon_1 = \frac{0.002835}{8.6956 \times 10^{-4}}$$

$$\varepsilon_1 = 2.2599$$

$$\varepsilon_2 = \varepsilon_1 + 1$$

$$\varepsilon_2 = 2.2599 + 1$$

$$\varepsilon_2 = 3.2599$$

Fringe temperature, T_1, T_2

$$T = \frac{T_{REF}}{1 \pm \frac{\varepsilon R \lambda T_{REF}}{GPZ}}$$

$$T_1 = \frac{288.82}{1 - \frac{(2.2599)(287)(6.328 \times 10^{-7})(288.82)}{(0.226 \times 10^{-3})(99945)(0.547)}}$$

$$T_1 = 291.62\ K$$

$$T_2 = \frac{288.82}{1 - \frac{(3.2599)(287)(6.328 \times 10^{-7})(288.82)}{(0.226 \times 10^{-3})(99945)(0.547)}}$$

$$T_2 = 292.87\ K$$

Temperature gradient, dT/dx

The temperature gradient was determined by assuming linear interpolation:

$$\left.\frac{dT}{dx}\right|_{x=0} = \frac{\Delta T}{\Delta x}$$

$$\left.\frac{dT}{dx}\right|_{x=0} = \frac{1.2554}{8.6956 \times 10^{-4}}$$

$$\left.\frac{dT}{dx}\right|_{x=0} = 1.4437 \times 10^{3} K/m$$

Local convective heat flux, q″

$$q'' = -k_S \left.\frac{dT}{dx}\right|_{x=0}$$

$$q'' = -(0.0253)(1.4437 \times 10^{3})$$

$$q'' = -36.51 W/m^2$$

Average cold wall convective heat flux, q

The above process was repeated for 80 equally spaced intervals along the walls and numerically integrated using the trapezoidal rule to get the average convective heat flux.

$$q''_C = -37.74\ W/m^2$$

Appendix D: Tabulated Data

Table D.1 Summary of experimental conditions

Table D.#	q″ (W/m^2)	ϕ (°)	W (mm)	ΔT (°C)	T_C (°C)	T_H (°C)	T_B (°C)
2, 3	74.9538	0	40.7	0.02	22.78	22.76	29.4751
4, 5	155.108	0	40.7	0.08	23.25	23.17	36.2351
6, 7	0	0	40.7	15.02	15.19	30.21	23.0076
8	75.0633	0	40.7	14.92	15.67	30.59	30.1953
9	150.0761	0	40.7	14.95	15.93	30.88	36.6916
10, 11	74.9654	0	56.7	0.04	21.92	21.96	30.2979
12, 13	150.0926	0	56.7	0.05	22.52	22.47	38.3022
14, 15	0	0	56.7	15.07	15.24	30.31	22.9733
16	74.9279	0	56.7	15	15.62	30.62	31.2537
17, 18	74.9654	45	56.7	0	20.83	20.83	28.2705
19, 20	0	45	56.7	15.01	15.19	30.2	22.696
21, 22	74.9999	45	56.7	14.99	15.55	30.54	29.51
23, 24	74.9999	0	32.7	0	22.22	22.22	27.9946
25, 26	150.0926	0	32.7	0.05	22.6	22.55	33.7865
27, 28	0	0	32.7	15.04	15.15	30.19	22.7299
29	74.9999	0	32.7	15	15.45	30.45	28.5467
30, 31	75.0345	45	32.7	0.03	20.74	20.71	26.1963
32, 38	149.9907	45	32.7	0.02	21.29	21.27	32.5088
34, 35	0	45	32.7	15.01	15.16	30.17	22.2133
36	74.9971	45	32.7	14.99	15.54	30.53	28.2715
37, 38	0	-45	32.7	15	30.17	15.17	22.7994

Table D.2 Local Cold Wall Convective Heat Flux for W = 40.7mm, $\phi = 0°$, $\Delta T = 0.02°C$, and $q_B'' = 74.95\ W/m^2$

q''(W/m²)	Y (m)	q''(W/m²)	Y (m)	q''(W/m²)	Y (m)	q''(W/m²)	Y (m)
-15.9971	0.0972	-15.6677	0.0747	-10.2398	0.0522	-11.2736	0.0297
-13.2604	0.0961	-7.9531	0.0736	-8.0437	0.0511	-9.5607	0.0286
-11.7891	0.0950	-11.3224	0.0725	-6.0567	0.0500	-7.9045	0.0275
-9.1444	0.0938	-8.2929	0.0713	-5.1797	0.0488	-5.8256	0.0263
-5.4543	0.0927	-8.0946	0.0702	-7.8977	0.0477	-5.5352	0.0252
-5.2472	0.0916	-7.7988	0.0691	-6.8291	0.0466	-5.8295	0.0241
-4.7157	0.0905	-7.1933	0.0680	-6.9343	0.0455	-5.8134	0.0230
-4.8864	0.0893	-7.7474	0.0668	-5.5989	0.0443	-7.3821	0.0218
-5.2982	0.0882	-8.6003	0.0657	-7.2367	0.0432	-9.8538	0.0207
-6.5545	0.0871	-9.5511	0.0646	-9.2440	0.0421	-11.0006	0.0196
-8.1950	0.0860	-11.6375	0.0635	-10.9721	0.0410	-12.2508	0.0185
-10.2836	0.0848	-14.0028	0.0623	-14.3504	0.0398	-15.0906	0.0173
-11.5385	0.0837	-16.9460	0.0612	-16.4523	0.0387	-16.8095	0.0162
-14.3635	0.0826	-18.3993	0.0601	-17.3600	0.0376	-16.3786	0.0151
-16.3636	0.0815	-18.4513	0.0590	-17.5922	0.0365	-16.5933	0.0140
-17.9867	0.0803	-21.3117	0.0578	-18.5642	0.0353	-17.2080	0.0128
-19.1595	0.0792	-17.5968	0.0567	-17.3106	0.0342	-13.3439	0.0117
-20.3227	0.0781	-16.9546	0.0556	-17.3117	0.0331	-13.4291	0.0106
-16.1469	0.0770	-14.9856	0.0545	-15.4762	0.0320	-10.9618	0.0095
-14.5370	0.0758	-12.4891	0.0533	-13.8174	0.0308	-9.0099	0.0083

Table D.3 Local Hot Wall Convective Heat Flux for W = 40.7mm, $\phi = 0°$, $\Delta T = 0.02°C$, and $q_B'' = 74.95 W/m^2$

$q''(W/m^2)$	Y (m)	$q''(W/m^2)$	Y (m)	$q''(W/m^2)$	Y (m)	$q''(W/m^2)$	Y (m)
-22.2554	0.0972	-20.1295	0.0747	-22.0059	0.0522	-19.6570	0.0286
-19.1397	0.0961	-22.4652	0.0736	-16.7597	0.0511	-15.5724	0.0275
-16.9159	0.0950	-18.5194	0.0725	-17.2695	0.0500	-16.4023	0.0263
-15.1516	0.0938	-16.9137	0.0713	-15.1387	0.0488	-11.0645	0.0252
-13.6511	0.0927	-13.3273	0.0702	-12.3298	0.0477	-11.7583	0.0241
-10.9528	0.0916	-11.3194	0.0691	-10.3496	0.0466	-7.7247	0.0230
-8.7003	0.0905	-8.5051	0.0680	-8.7197	0.0455	-9.2703	0.0218
-6.3321	0.0893	-8.2631	0.0668	-8.6211	0.0443	-8.1908	0.0207
-6.3872	0.0882	-8.6016	0.0657	-9.1311	0.0432	-8.7419	0.0196
-5.7993	0.0871	-8.8287	0.0646	-9.3453	0.0421	-11.1166	0.0185
-7.4348	0.0860	-10.3089	0.0635	-12.7096	0.0410	-15.1593	0.0173
-8.0736	0.0848	-13.7894	0.0623	-15.5815	0.0398	-17.1695	0.0162
-10.6067	0.0837	-18.8079	0.0612	-19.0007	0.0387	-20.8537	0.0151
-14.0574	0.0826	-35.9268	0.0601	-22.9029	0.0376	-23.5913	0.0140
-17.6720	0.0815	-41.2012	0.0590	-27.7839	0.0353	-26.5458	0.0128
-21.2861	0.0803	-30.8262	0.0578	-27.2337	0.0342	-27.6054	0.0117
-23.8826	0.0792	-27.4778	0.0567	-26.9205	0.0331	-27.1480	0.0106
-25.7045	0.0781	-27.1425	0.0556	-24.1135	0.0320	-24.2914	0.0095
-27.8534	0.0770	-25.3577	0.0545	-23.6309	0.0308	-21.2759	0.0083
-24.8616	0.0758	-21.2725	0.0533	-20.5075	0.0297		

Table D.4 Local Cold Wall Convective Heat Flux for W = 40.7mm, $\phi = 0°$, $\Delta T = 0.08°C$, and $q_B'' = 155.11 W/m^2$

q"(W/m²)	Y (m)	q"(W/m²)	Y (m)	q"(W/m²)	Y (m)	q"(W/m²)	Y (m)
-35.4339	0.0972	-31.2106	0.0747	-25.2476	0.0522	-24.2095	0.0297
-32.0889	0.0961	-30.7980	0.0736	-22.8232	0.0511	-25.4521	0.0286
-25.7824	0.0950	-25.8119	0.0725	-23.6916	0.0500	-21.3114	0.0275
-20.9772	0.0938	-19.9240	0.0713	-19.8947	0.0488	-18.9356	0.0263
-18.8130	0.0927	-20.2040	0.0702	-16.7887	0.0477	-15.8689	0.0252
-20.0481	0.0916	-20.0452	0.0691	-15.7947	0.0466	-16.3262	0.0241
-14.5803	0.0905	-17.7748	0.0680	-14.1765	0.0455	-15.3646	0.0230
-15.5601	0.0893	-18.4030	0.0668	-14.8962	0.0443	-17.7982	0.0218
-15.3523	0.0882	-19.7695	0.0657	-16.9212	0.0432	-20.9496	0.0207
-16.0852	0.0871	-23.4918	0.0646	-18.4962	0.0421	-29.0654	0.0196
-17.6413	0.0860	-27.5851	0.0635	-23.9244	0.0410	-25.7775	0.0185
-24.7845	0.0848	-27.6133	0.0623	-27.3146	0.0398	-31.6233	0.0173
-26.6730	0.0837	-33.9472	0.0612	-30.4167	0.0387	-34.4579	0.0162
-31.2214	0.0826	-36.5110	0.0601	-35.9620	0.0376	-38.9697	0.0151
-37.2352	0.0815	-45.9225	0.0590	-36.6148	0.0365	-40.4389	0.0140
-37.7450	0.0803	-41.7963	0.0578	-37.1739	0.0353	-36.6197	0.0128
-39.6037	0.0792	-41.7963	0.0567	-37.1484	0.0342	-36.0530	0.0117
-40.2706	0.0781	-38.3721	0.0556	-33.4389	0.0331	-31.2575	0.0106
-35.0204	0.0770	-32.9939	0.0545	-33.4762	0.0320	-28.9814	0.0095
-34.8940	0.0758	-31.2756	0.0533	-28.9690	0.0308	-28.5498	0.0083

Table D.5 Local Hot Wall Convective Heat Flux for W = 40.7mm, $\phi = 0°$, $\Delta T = 0.08°C$, and $q_B'' = 155.11 W/m^2$

$q''(W/m^2)$	Y (m)	$q''(W/m^2)$	Y (m)	$q''(W/m^2)$	Y (m)	$q''(W/m^2)$	Y (m)
-48.9434	0.0972	-37.2509	0.0747	-42.7692	0.0522	-43.4794	0.0297
-44.3653	0.0961	-46.9513	0.0736	-35.1490	0.0511	-38.5536	0.0286
-38.5701	0.0950	-37.3016	0.0725	-34.5465	0.0500	-32.7002	0.0275
-34.6436	0.0938	-32.6884	0.0713	-30.5532	0.0488	-31.7466	0.0263
-30.1102	0.0927	-26.1735	0.0702	-23.7839	0.0477	-25.0140	0.0252
-28.3424	0.0916	-24.7434	0.0691	-22.3667	0.0466	-21.0281	0.0241
-22.4224	0.0905	-19.6045	0.0680	-18.3626	0.0455	-19.9053	0.0230
-18.5545	0.0893	-17.1851	0.0668	-16.4417	0.0443	-14.4658	0.0218
-18.0809	0.0882	-17.8453	0.0657	-17.0354	0.0432	-16.4397	0.0207
-15.7877	0.0871	-19.1374	0.0646	-21.1634	0.0421	-17.4698	0.0196
-16.5557	0.0860	-23.7400	0.0635	-26.4636	0.0410	-20.6563	0.0185
-18.4214	0.0848	-29.4271	0.0623	-33.2151	0.0398	-27.6570	0.0173
-22.6254	0.0837	-44.3653	0.0612	-39.8400	0.0387	-36.2247	0.0162
-35.7917	0.0826	-56.1392	0.0601	-45.2502	0.0376	-43.6611	0.0151
-40.5461	0.0815	-60.4788	0.0590	-54.6079	0.0365	-47.9859	0.0140
-47.0814	0.0803	-63.5569	0.0578	-56.0353	0.0353	-53.3662	0.0128
-52.1797	0.0792	-53.5341	0.0567	-54.6737	0.0342	-52.3504	0.0117
-54.7287	0.0781	-54.8058	0.0556	-53.4396	0.0331	-47.0733	0.0106
-54.6957	0.0770	-48.0792	0.0545	-47.0407	0.0320	-45.3106	0.0095
-52.2800	0.0758	-46.9837	0.0533	-44.4161	0.0308	-46.9919	0.0083

Table D.6 Local Cold Wall Convective Heat Flux for W = 40.7mm, ϕ = 0°, ΔT = 15.02°C, and q_B'' = 0 W/m^2

q"(W/m^2)	Y (m)	q"(W/m^2)	Y (m)	q"(W/m^2)	Y (m)	q"(W/m^2)	Y (m)
-21.5548	0.0972	-23.1510	0.0748	-20.0039	0.0502	-20.7554	0.0292
-22.0194	0.0965	-21.1493	0.0741	-23.1510	0.0494	-21.1876	0.0285
-20.9778	0.0957	-22.0006	0.0718	-20.7420	0.0487	-20.3260	0.0277
-20.7086	0.0950	-21.8354	0.0703	-22.0345	0.0479	-22.4593	0.0270
-20.5426	0.0942	-19.9604	0.0696	-20.9881	0.0472	-21.1702	0.0263
-20.7655	0.0935	-21.3714	0.0688	-20.7253	0.0464	-20.3116	0.0255
-21.7395	0.0927	-21.1754	0.0681	-22.7139	0.0457	-23.4174	0.0248
-21.7690	0.0920	-21.1146	0.0673	-20.7722	0.0449	-21.3643	0.0240
-20.9590	0.0912	-21.1493	0.0666	-21.1163	0.0442	-20.9778	0.0233
-20.8960	0.0905	-20.7588	0.0658	-21.3430	0.0434	-19.9418	0.0225
-21.7561	0.0898	-20.1234	0.0651	-20.1835	0.0427	-20.7353	0.0218
-22.0194	0.0890	-21.9912	0.0644	-21.3112	0.0419	-21.8058	0.0210
-21.5151	0.0883	-20.1724	0.0636	-19.0823	0.0412	-20.0194	0.0203
-19.4118	0.0875	-20.3068	0.0629	-20.3630	0.0404	-21.1284	0.0195
-20.5442	0.0868	-19.0724	0.0621	-18.4757	0.0397	-20.3663	0.0188
-20.9710	0.0860	-20.1692	0.0614	-19.7665	0.0390	-19.4706	0.0180
-20.5393	0.0845	-20.5656	0.0606	-19.9790	0.0382	-19.9480	0.0173
-19.5704	0.0830	-20.2167	0.0599	-20.3759	0.0375	-19.7970	0.0165
-19.7833	0.0823	-20.0101	0.0576	-18.8077	0.0367	-18.7830	0.0158
-19.6242	0.0815	-19.9542	0.0569	-19.9620	0.0360	-19.0993	0.0136
-20.7805	0.0808	-22.4613	0.0561	-20.7571	0.0352	-18.4651	0.0128
-20.1424	0.0800	-19.1192	0.0554	-19.6392	0.0345	-19.6647	0.0121
-21.5656	0.0793	-20.3228	0.0546	-20.5164	0.0337	-20.3469	0.0113
-20.9744	0.0785	-21.9987	0.0539	-20.5311	0.0330	-19.6512	0.0098
-20.1266	0.0778	-19.8076	0.0531	-20.3679	0.0322	-19.7757	0.0091
-21.5620	0.0771	-19.9326	0.0524	-20.7722	0.0315	-19.0979	0.0083
-20.1724	0.0763	-21.7634	0.0517	-19.7726	0.0307		
-20.8926	0.0756	-21.1545	0.0509	-20.3469	0.0300		

Table D.7 Local Hot Wall Convective Heat Flux for W = 40.7mm, $\phi = 0°$, $\Delta T = 15.02°C$, and $q_B'' = 0\ W/m^2$

$q''(W/m^2)$	Y (m)	$q''(W/m^2)$	Y (m)	$q''(W/m^2)$	Y (m)	$q''(W/m^2)$	Y (m)
21.9048	0.0972	22.2623	0.0747	22.0920	0.0522	21.6499	0.0297
21.7089	0.0961	23.0744	0.0736	21.5082	0.0511	22.6200	0.0286
21.5198	0.0950	23.9411	0.0725	21.1401	0.0500	22.2256	0.0275
21.1529	0.0938	23.2744	0.0713	22.4599	0.0488	21.5481	0.0263
22.2753	0.0927	23.8166	0.0702	22.4473	0.0477	24.0236	0.0252
22.2789	0.0916	23.4799	0.0691	23.5017	0.0466	23.3485	0.0241
22.2682	0.0905	24.0256	0.0680	23.0648	0.0455	23.3485	0.0230
23.3036	0.0893	22.9247	0.0668	22.8440	0.0443	23.3368	0.0218
23.5176	0.0882	23.7882	0.0657	22.5252	0.0432	22.6955	0.0207
24.6601	0.0871	23.3387	0.0646	24.3929	0.0421	24.2216	0.0196
24.4185	0.0860	24.9601	0.0635	23.5812	0.0410	23.5335	0.0185
23.7234	0.0848	23.7740	0.0623	25.2399	0.0398	23.7598	0.0173
24.8954	0.0837	22.0850	0.0612	23.3426	0.0387	24.4571	0.0162
23.5852	0.0826	23.4187	0.0601	23.7760	0.0376	23.9699	0.0151
26.2979	0.0815	22.5595	0.0590	22.8965	0.0365	24.9177	0.0140
22.9153	0.0803	20.9340	0.0578	21.3242	0.0353	23.2803	0.0128
24.2321	0.0792	22.0205	0.0567	21.6786	0.0342	22.7325	0.0117
23.7679	0.0781	22.5052	0.0556	19.6354	0.0331	23.3602	0.0106
22.0798	0.0770	21.9117	0.0545	21.6617	0.0320	23.3426	0.0095
23.7396	0.0758	21.8979	0.0533	22.0536	0.0308	21.5381	0.0083

Table D.8 Local Cold Wall Convective Heat Flux for W = 40.7 mm, ϕ = 0°, ΔT = 14.92°C, and q_B'' = 75.06W/m^2

q"(W/m^2)	Y (m)	q"(W/m^2)	Y (m)	q"(W/m^2)	Y (m)	q"(W/m^2)	Y (m)
-37.1381	0.0972	-36.4814	0.0747	-36.3994	0.0522	-37.0637	0.0297
-40.5813	0.0961	-33.6440	0.0736	-37.8023	0.0511	-40.4610	0.0286
-40.5242	0.0950	-34.7225	0.0725	-39.1337	0.0500	-38.3030	0.0275
-42.0786	0.0938	-38.3654	0.0713	-40.5749	0.0488	-40.5813	0.0263
-42.0445	0.0927	-38.3484	0.0702	-38.3711	0.0477	-41.3230	0.0252
-43.7201	0.0916	-39.0218	0.0691	-39.7802	0.0466	-42.0991	0.0241
-43.6906	0.0905	-39.7131	0.0680	-39.0453	0.0455	-41.2901	0.0230
-42.8270	0.0893	-39.7070	0.0668	-41.2638	0.0443	-41.2572	0.0218
-41.9900	0.0882	-36.3840	0.0657	-39.7253	0.0432	-42.0718	0.0207
-41.1982	0.0871	-37.7913	0.0646	-39.7253	0.0421	-39.7497	0.0196
-41.9832	0.0860	-37.6540	0.0635	-37.0372	0.0410	-39.7497	0.0185
-40.4231	0.0848	-36.5328	0.0623	-37.0425	0.0398	-37.0531	0.0173
-39.7009	0.0837	-35.3506	0.0612	-34.1387	0.0387	-33.1084	0.0162
-39.7009	0.0826	-34.7784	0.0601	-35.8276	0.0376	-35.2592	0.0151
-37.6485	0.0815	-33.1890	0.0590	-35.2352	0.0365	-38.3711	0.0140
-38.3030	0.0803	-33.6922	0.0578	-32.2425	0.0353	-34.6806	0.0128
-35.7880	0.0792	-33.1677	0.0567	-33.2188	0.0342	-36.4147	0.0117
-35.9419	0.0781	-32.1704	0.0556	-34.7831	0.0331	-35.7930	0.0106
-35.9320	0.0770	-34.1747	0.0545	-33.6922	0.0320	-34.7784	0.0095
-34.7597	0.0758	-35.2496	0.0533	-35.8723	0.0308	-36.5122	0.0083

Table D.9 Local Hot Wall Convective Heat Flux for W = 40.7 mm, ϕ = 0°, ΔT = 14.95°C, and q_B'' = 150.08W/m^2

q"(W/m^2)	Y (m)	q"(W/m^2)	Y (m)	q"(W/m^2)	Y (m)	q"(W/m^2)	Y (m)
-65.3283	0.0972	-58.4305	0.0747	-61.4524	0.0522	-65.1308	0.0297
-65.2623	0.0961	-51.0071	0.0736	-65.3448	0.0511	-69.4821	0.0286
-71.6048	0.0950	-61.6430	0.0725	-74.1151	0.0500	-74.1576	0.0275
-69.2960	0.0938	-65.2623	0.0713	-69.3890	0.0488	-69.3332	0.0263
-73.9668	0.0927	-69.3704	0.0702	-71.6445	0.0477	-71.5651	0.0252
-74.2639	0.0916	-67.2187	0.0691	-67.2012	0.0466	-67.1314	0.0241
-71.5058	0.0905	-61.4963	0.0680	-67.2012	0.0455	-67.1314	0.0230
-71.8035	0.0893	-65.1965	0.0668	-65.1965	0.0443	-67.1314	0.0218
-69.5195	0.0882	-65.2294	0.0657	-65.2130	0.0432	-63.2459	0.0207
-71.5255	0.0871	-59.8687	0.0646	-58.2461	0.0421	-63.2924	0.0196
-65.1472	0.0860	-55.3222	0.0635	-56.7465	0.0410	-55.2985	0.0185
-63.2769	0.0848	-51.4277	0.0623	-55.3578	0.0398	-56.7839	0.0173
-58.2461	0.0837	-51.4584	0.0612	-49.1535	0.0387	-52.6993	0.0162
-59.8965	0.0826	-48.0544	0.0601	-48.0812	0.0376	-50.2845	0.0151
-55.3696	0.0815	-46.0055	0.0590	-48.0723	0.0365	-50.2845	0.0140
-52.7316	0.0803	-50.2257	0.0578	-48.0454	0.0353	-51.4482	0.0128
-52.7316	0.0792	-51.5817	0.0567	-50.2062	0.0342	-50.1964	0.0117
-54.0241	0.0781	-55.4409	0.0556	-51.5406	0.0331	-56.9215	0.0106
-53.9902	0.0770	-58.3250	0.0545	-56.8339	0.0320	-58.3514	0.0095
-53.9225	0.0758	-63.3389	0.0533	-59.8410	0.0308	-65.2459	0.0083

Table D.10 Local Cold Wall Convective Heat Flux for W = 56.7mm, ϕ = 0°, ΔT = 0.04°C, and q_B'' = 74.97W/m^2

q″(W/m^2)	Y (m)	q″(W/m^2)	Y (m)	q″(W/m^2)	Y (m)	q″(W/m^2)	Y (m)
-12.6278	0.0972	-10.5687	0.0747	-10.7247	0.0511	-12.2977	0.0275
-12.0967	0.0961	-11.2380	0.0736	-11.8314	0.0500	-12.1641	0.0263
-13.0568	0.0950	-11.5120	0.0725	-10.6142	0.0488	-11.9096	0.0252
-13.3633	0.0938	-11.4492	0.0713	-11.8267	0.0477	-12.8458	0.0241
-12.0918	0.0927	-11.2225	0.0702	-14.4985	0.0466	-12.1569	0.0230
-11.9069	0.0916	-11.7920	0.0691	-10.5596	0.0455	-12.0907	0.0218
-11.3171	0.0905	-12.7066	0.0680	-10.1372	0.0443	-11.4288	0.0207
-10.0286	0.0893	-10.6779	0.0668	-10.6546	0.0432	-11.2005	0.0196
-10.4425	0.0882	-12.0209	0.0646	-10.7009	0.0410	-12.2166	0.0185
-11.0526	0.0871	-11.1866	0.0635	-11.5037	0.0398	-11.7749	0.0173
-9.8604	0.0860	-11.5214	0.0623	-11.2739	0.0387	-11.8324	0.0162
-8.5390	0.0848	-14.5811	0.0612	-11.5516	0.0376	-9.9285	0.0151
-9.5733	0.0837	-11.2268	0.0601	-11.5437	0.0365	-9.6344	0.0140
-14.1974	0.0826	-10.9548	0.0590	-12.2194	0.0353	-10.0568	0.0128
-9.6134	0.0815	-11.3281	0.0578	-12.4090	0.0342	-9.3183	0.0117
-10.1223	0.0803	-12.1696	0.0567	-11.8879	0.0331	-10.4191	0.0106
-9.5671	0.0792	-12.9205	0.0556	-12.5178	0.0320	-10.9700	0.0095
-11.2099	0.0781	-11.7230	0.0545	-12.4476	0.0308	-10.5600	0.0083
-10.1112	0.0770	-12.1509	0.0533	-12.2411	0.0297		
-10.8737	0.0758	-11.7168	0.0522	-12.7865	0.0286		

Table D.11 Local Hot Wall Convective Heat Flux for W = 56.7mm, $\phi = 0°$, $\Delta T = 0.04°C$, and $q_B'' = 74.97 W/m^2$

$q''(W/m^2)$	Y (m)	$q''(W/m^2)$	Y (m)	$q''(W/m^2)$	Y (m)	$q''(W/m^2)$	Y (m)
-14.3504	0.0972	-12.3151	0.0736	-13.5065	0.0500	-12.2740	0.0275
-14.7158	0.0961	-12.7923	0.0725	-12.6068	0.0488	-12.4717	0.0263
-15.5027	0.0950	-13.3047	0.0713	-14.5210	0.0477	-12.3231	0.0252
-14.8944	0.0938	-13.8576	0.0702	-13.3882	0.0466	-11.1766	0.0241
-14.2100	0.0927	-12.6329	0.0691	-14.2123	0.0455	-11.8144	0.0230
-14.8500	0.0916	-12.6938	0.0668	-13.6216	0.0443	-11.1197	0.0218
-14.0320	0.0905	-12.0242	0.0657	-12.3067	0.0432	-11.0190	0.0207
-13.6973	0.0893	-12.2791	0.0646	-11.9165	0.0421	-11.1280	0.0196
-12.9965	0.0882	-11.7719	0.0635	-10.8956	0.0410	-10.5646	0.0185
-13.1484	0.0871	-11.4773	0.0623	-12.1065	0.0398	-11.0221	0.0173
-11.8587	0.0860	-10.6184	0.0612	-12.5721	0.0387	-10.3753	0.0162
-11.2158	0.0848	-11.4744	0.0601	-12.1098	0.0376	-11.1901	0.0151
-11.4475	0.0837	-10.5691	0.0590	-11.5597	0.0365	-11.3021	0.0140
-10.5534	0.0826	-11.7596	0.0578	-11.6152	0.0353	-13.8297	0.0128
-10.9547	0.0815	-11.3450	0.0567	-12.0431	0.0342	-12.4868	0.0117
-10.8446	0.0803	-11.9334	0.0556	-11.7884	0.0331	-12.0225	0.0106
-11.1036	0.0792	-12.3713	0.0545	-11.9128	0.0320	-12.9770	0.0095
-12.0929	0.0770	-12.9983	0.0533	-12.4221	0.0308	-12.6151	0.0083
-11.8849	0.0758	-13.2092	0.0522	-13.3562	0.0297		
-12.9483	0.0747	-14.0093	0.0511	-12.9047	0.0286		

Table D.12 Local Cold Wall Convective Heat Flux for W = 56.7mm, ϕ = 0°, ΔT = 0.05°C, and q_B'' = 150.09W/m^2

q″(W/m^2)	Y (m)	q″(W/m^2)	Y (m)	q″(W/m^2)	Y (m)	q″(W/m^2)	Y (m)
-29.2250	0.0972	-22.2345	0.0747	-24.3557	0.0522	-23.3399	0.0297
-26.2307	0.0961	-23.5612	0.0736	-25.7105	0.0511	-22.8844	0.0286
-27.4871	0.0950	-26.8789	0.0725	-24.0893	0.0500	-22.2144	0.0275
-28.1557	0.0938	-23.5735	0.0713	-25.1355	0.0488	-23.1109	0.0263
-25.3756	0.0927	-22.4166	0.0702	-23.8265	0.0477	-20.4485	0.0252
-24.0507	0.0916	-23.3157	0.0691	-25.3994	0.0466	-20.6370	0.0241
-24.5722	0.0905	-24.3953	0.0680	-24.5834	0.0455	-21.5928	0.0230
-25.1098	0.0893	-24.9067	0.0668	-25.9493	0.0443	-20.0950	0.0218
-24.5722	0.0882	-23.8581	0.0657	-23.3178	0.0432	-18.8505	0.0207
-22.4240	0.0871	-26.6018	0.0646	-25.6470	0.0421	-19.4823	0.0196
-23.0912	0.0860	-25.4066	0.0635	-25.4568	0.0410	-19.9810	0.0185
-23.0892	0.0848	-25.1238	0.0623	-26.0142	0.0398	-19.2991	0.0173
-23.8013	0.0837	-25.3851	0.0612	-26.6122	0.0387	-21.6482	0.0162
-24.4085	0.0826	-27.1619	0.0601	-25.7080	0.0376	-21.2424	0.0151
-25.6446	0.0815	-26.5287	0.0590	-25.7031	0.0365	-24.1172	0.0140
-24.6573	0.0803	-24.9136	0.0578	-25.6909	0.0353	-21.8243	0.0128
-26.0417	0.0792	-25.9219	0.0567	-26.2740	0.0342	-22.8844	0.0117
-24.6281	0.0781	-26.0267	0.0556	-25.6909	0.0331	-22.2217	0.0106
-24.3623	0.0770	-27.2357	0.0545	-25.4018	0.0320	-20.0875	0.0095
-24.6147	0.0758	-25.7178	0.0533	-25.9742	0.0308	-22.2107	0.0083

Table D.13 Local Hot Wall Convective Heat Flux for W = 56.7mm, $\phi = 0°$, $\Delta T = 0.05°C$, and $q_B'' = 150.09 W/m^2$

$q''(W/m^2)$	Y (m)	$q''(W/m^2)$	Y (m)	$q''(W/m^2)$	Y (m)	$q''(W/m^2)$	Y (m)
-31.7040	0.0972	-32.2017	0.0747	-28.1707	0.0522	-26.5543	0.0297
-30.0334	0.0961	-27.5403	0.0736	-28.8800	0.0511	-25.6607	0.0286
-31.2430	0.0950	-26.5934	0.0725	-27.4927	0.0500	-25.3817	0.0275
-28.8830	0.0938	-27.2109	0.0713	-27.1644	0.0488	-26.5438	0.0263
-27.5039	0.0927	-25.9934	0.0702	-27.4899	0.0477	-24.6626	0.0252
-27.4983	0.0916	-26.2862	0.0691	-24.6671	0.0466	-26.5360	0.0241
-28.8769	0.0905	-22.8901	0.0680	-25.3745	0.0455	-26.5308	0.0230
-27.1671	0.0893	-24.8710	0.0668	-24.1543	0.0443	-26.5412	0.0218
-26.6458	0.0882	-23.8458	0.0657	-25.3769	0.0432	-25.9410	0.0207
-25.7487	0.0871	-24.8619	0.0646	-24.1500	0.0421	-28.1619	0.0196
-26.3143	0.0860	-24.3323	0.0635	-25.4845	0.0410	-30.3975	0.0185
-27.5571	0.0848	-24.8368	0.0623	-23.8837	0.0398	-28.8645	0.0173
-27.5459	0.0837	-24.6604	0.0612	-24.6379	0.0387	-30.7812	0.0162
-27.2027	0.0826	-25.1858	0.0601	-24.6290	0.0376	-30.7882	0.0151
-26.8679	0.0815	-26.3168	0.0590	-25.4294	0.0365	-30.7812	0.0140
-29.5999	0.0803	-29.6973	0.0578	-25.7071	0.0353	-31.6299	0.0128
-29.5934	0.0792	-26.9000	0.0567	-23.5861	0.0342	-35.5322	0.0117
-28.2501	0.0781	-28.5480	0.0556	-26.5778	0.0331	-31.6262	0.0106
-28.2383	0.0770	-28.5390	0.0545	-29.2386	0.0320	-32.0835	0.0095
-29.3083	0.0758	-29.2608	0.0533	-25.9635	0.0308	-30.7987	0.0083

Table D.14 Local Cold Wall Convective Heat Flux for W = 56.7mm, $\phi = 0°$, $\Delta T = 15.07°C$, and $q_B'' = 0W/m^2$

$q''(W/m^2)$	Y (m)	$q''(W/m^2)$	Y (m)	$q''(W/m^2)$	Y (m)	$q''(W/m^2)$	Y (m)
-18.8583	0.0972	-17.9767	0.0747	-17.5428	0.0522	-15.4905	0.0297
-19.9134	0.0961	-20.2706	0.0736	-17.8993	0.0511	-17.3661	0.0286
-19.0232	0.0950	-17.9592	0.0725	-17.5285	0.0500	-15.9459	0.0275
-18.3696	0.0938	-16.8340	0.0713	-16.8406	0.0488	-16.4236	0.0263
-19.0064	0.0927	-18.2557	0.0702	-17.8072	0.0477	-16.0487	0.0252
-18.2067	0.0916	-16.8307	0.0691	-16.6982	0.0466	-16.9297	0.0241
-18.5862	0.0905	-18.7233	0.0680	-17.5071	0.0455	-15.8688	0.0230
-18.5862	0.0893	-17.9267	0.0668	-16.5560	0.0443	-15.2974	0.0218
-19.0781	0.0882	-18.2247	0.0657	-17.6396	0.0432	-16.5944	0.0207
-18.5755	0.0871	-18.0656	0.0646	-20.1163	0.0421	-17.8195	0.0196
-20.5281	0.0860	-18.3643	0.0635	-18.2298	0.0410	-15.9676	0.0185
-18.4076	0.0848	-16.9799	0.0623	-17.6287	0.0398	-15.8483	0.0173
-18.3984	0.0837	-18.4326	0.0612	-17.6190	0.0387	-15.9577	0.0162
-18.8873	0.0826	-17.3755	0.0601	-17.3322	0.0376	-16.3211	0.0151
-19.7599	0.0815	-16.9642	0.0590	-17.1203	0.0365	-15.9489	0.0140
-19.0471	0.0803	-17.9404	0.0578	-17.2516	0.0353	-15.6036	0.0128
-19.3839	0.0792	-17.7863	0.0567	-16.4550	0.0342	-16.0607	0.0117
-18.2234	0.0781	-18.2311	0.0556	-16.7058	0.0331	-16.0617	0.0106
-18.3774	0.0770	-20.1053	0.0545	-17.1056	0.0320	-16.0517	0.0095
-18.3669	0.0758	-18.3735	0.0533	-16.8318	0.0308	-15.9351	0.0083

Table D.15 Local Hot Wall Convective Heat Flux for W = 56.7mm, $\phi = 0°$, $\Delta T = 15.07°C$, and $q_B'' = 0W/m^2$

$q''(W/m^2)$	Y (m)	$q''(W/m^2)$	Y (m)	$q''(W/m^2)$	Y (m)	$q''(W/m^2)$	Y (m)
16.0327	0.0972	19.4499	0.0736	19.4905	0.0511	18.3207	0.0286
16.9737	0.0961	19.4432	0.0725	18.8901	0.0500	19.9282	0.0275
18.4854	0.0950	20.2266	0.0713	22.0759	0.0488	20.5976	0.0263
17.3218	0.0938	19.4337	0.0702	19.1659	0.0477	17.5414	0.0252
18.4683	0.0927	19.3676	0.0691	19.4621	0.0466	20.4320	0.0241
17.5535	0.0916	21.5335	0.0680	18.0487	0.0455	20.2632	0.0230
17.1845	0.0905	20.3043	0.0668	17.5381	0.0443	20.1131	0.0218
17.2994	0.0893	19.1987	0.0657	17.9100	0.0432	20.7844	0.0207
18.0441	0.0882	19.1948	0.0646	20.2281	0.0421	20.9667	0.0196
17.4039	0.0871	18.4793	0.0635	18.5715	0.0410	18.6134	0.0185
17.2781	0.0860	20.2838	0.0623	18.5690	0.0398	20.7967	0.0173
18.1554	0.0848	19.6343	0.0612	18.1495	0.0387	20.9667	0.0162
18.0151	0.0837	19.1712	0.0601	18.6356	0.0376	20.2882	0.0151
18.0058	0.0826	20.9354	0.0590	19.3622	0.0365	19.4905	0.0140
17.8197	0.0815	19.4540	0.0578	18.3459	0.0353	20.8060	0.0128
19.4905	0.0803	20.0655	0.0567	18.0825	0.0342	19.2027	0.0117
18.7507	0.0792	18.2956	0.0556	18.3387	0.0331	20.6446	0.0106
19.9466	0.0781	19.8305	0.0545	17.1930	0.0320	19.5136	0.0095
18.0557	0.0770	21.5368	0.0533	19.0328	0.0308	20.6599	0.0083
18.7319	0.0758	19.9751	0.0522	18.4671	0.0297		

Table D.16 Local Cold Wall Convective Heat Flux for W = 56.7mm, $\phi = 0°$, $\Delta T = 15°C$, and $q_B'' = 74.93 W/m^2$

$q''(W/m^2)$	Y (m)	$q''(W/m^2)$	Y (m)	$q''(W/m^2)$	Y (m)	$q''(W/m^2)$	Y (m)
-30.6427	0.0972	-33.0659	0.0747	-32.4847	0.0511	-29.9066	0.0286
-28.2267	0.0961	-35.1922	0.0725	-32.9941	0.0500	-29.8824	0.0275
-27.2465	0.0950	-36.9927	0.0713	-32.0028	0.0488	-31.1631	0.0263
-29.0997	0.0938	-42.0325	0.0702	-32.4888	0.0477	-31.6122	0.0252
-29.4876	0.0927	-37.5998	0.0691	-31.2083	0.0466	-31.1255	0.0241
-29.4741	0.0916	-37.5670	0.0680	-30.3093	0.0455	-30.6645	0.0230
-27.2235	0.0905	-38.9227	0.0668	-30.3164	0.0443	-33.5196	0.0218
-27.9164	0.0893	-40.3737	0.0657	-29.4707	0.0432	-33.5066	0.0207
-29.8444	0.0882	-39.6197	0.0646	-29.0735	0.0421	-33.4935	0.0196
-29.0114	0.0871	-37.6931	0.0635	-26.8814	0.0410	-35.1300	0.0185
-29.7996	0.0860	-39.0581	0.0623	-28.6550	0.0398	-34.0083	0.0173
-30.1993	0.0848	-37.6766	0.0612	-28.2638	0.0387	-34.1433	0.0162
-29.8859	0.0837	-36.3844	0.0601	-28.6264	0.0376	-36.4511	0.0151
-32.1023	0.0826	-37.0192	0.0590	-27.8681	0.0365	-33.0744	0.0140
-31.6122	0.0815	-37.6601	0.0578	-29.3734	0.0353	-32.5544	0.0128
-34.6459	0.0803	-35.7759	0.0567	-27.5892	0.0342	-32.5626	0.0117
-35.7660	0.0792	-38.3236	0.0556	-29.0572	0.0331	-32.5626	0.0106
-32.4929	0.0781	-35.1826	0.0545	-29.4338	0.0320	-32.5503	0.0095
-35.1252	0.0770	-33.5066	0.0533	-31.1143	0.0308	-32.0545	0.0083
-36.2923	0.0758	-34.6041	0.0522	-30.6500	0.0297		

Table D.17 Local Cold Wall Convective Heat Flux for W = 56.7mm, ϕ = 45°, ΔT = 0°C, and $q_B'' = 74.97 W/m^2$

q"(W/m²)	Y (m)	q"(W/m²)	Y (m)	q"(W/m²)	Y (m)	q"(W/m²)	Y (m)
-9.5517	0.0961	-9.9120	0.0725	-9.5909	0.0477	-9.9773	0.0252
-9.1223	0.0950	-9.6926	0.0713	-9.4618	0.0466	-10.5334	0.0241
-9.8764	0.0938	-9.5648	0.0702	-9.9164	0.0455	-10.0548	0.0230
-10.6117	0.0927	-9.9391	0.0691	-10.6618	0.0443	-10.0967	0.0218
-9.9963	0.0916	-9.5950	0.0680	-9.9042	0.0432	-10.3242	0.0207
-9.6906	0.0905	-10.7374	0.0668	-10.3027	0.0421	-10.1795	0.0196
-9.3240	0.0893	-10.0940	0.0646	-11.1092	0.0410	-11.0781	0.0185
-9.7206	0.0882	-9.3409	0.0635	-10.5811	0.0398	-10.3562	0.0173
-10.3422	0.0871	-8.9979	0.0612	-10.3740	0.0387	-10.3515	0.0162
-10.0167	0.0860	-9.1037	0.0601	-10.6674	0.0376	-10.3027	0.0151
-8.8693	0.0848	-8.8517	0.0590	-10.3165	0.0365	-9.8878	0.0140
-9.6216	0.0837	-8.7776	0.0578	-10.4075	0.0353	-11.1641	0.0128
-9.6543	0.0826	-8.7724	0.0567	-10.3987	0.0342	-9.7515	0.0117
-9.5708	0.0815	-8.6043	0.0556	-10.4431	0.0331	-8.8302	0.0106
-9.0303	0.0803	-9.0141	0.0545	-10.1975	0.0320	-9.6195	0.0095
-9.6499	0.0792	-8.9009	0.0533	-10.4800	0.0308	-9.0010	0.0083
-9.2451	0.0781	-9.1853	0.0522	-10.4689	0.0297		
-9.3177	0.0770	-8.9580	0.0511	-10.4161	0.0286		
-9.2756	0.0758	-9.2112	0.0500	-10.6054	0.0275		
-8.5011	0.0747	-10.4937	0.0488	-10.0731	0.0263		

Table D.18 Local Hot Wall Convective Heat Flux for W = 56.7mm, ϕ = 45°, ΔT = 0°C, and $q_B'' = 74.97 W/m^2$

q"(W/m²)	Y (m)	q"(W/m²)	Y (m)	q"(W/m²)	Y (m)	q"(W/m²)	Y (m)
-10.6930	0.0972	-10.9837	0.0736	-9.2147	0.0511	-9.3057	0.0275
-11.2204	0.0961	-10.0000	0.0725	-9.2083	0.0500	-8.8616	0.0263
-12.6691	0.0950	-10.3137	0.0713	-9.1672	0.0488	-8.6178	0.0252
-11.6133	0.0938	-9.8591	0.0702	-9.4304	0.0477	-10.0809	0.0241
-12.3013	0.0927	-9.6437	0.0691	-8.9765	0.0466	-10.0293	0.0230
-12.4344	0.0916	-10.5894	0.0680	-9.7064	0.0455	-10.4939	0.0218
-10.7033	0.0905	-10.1546	0.0668	-9.3390	0.0443	-11.6898	0.0207
-10.0763	0.0893	-10.7803	0.0657	-9.3715	0.0432	-10.7417	0.0196
-10.9002	0.0882	-10.6286	0.0646	-9.2518	0.0421	-10.7386	0.0185
-10.7451	0.0871	-10.1868	0.0635	-8.5779	0.0410	-10.9472	0.0173
-15.1180	0.0860	-9.8660	0.0623	-9.1697	0.0398	-10.7395	0.0162
-11.2645	0.0848	-11.0787	0.0612	-9.0168	0.0387	-11.2223	0.0151
-11.0938	0.0837	-9.8997	0.0601	-9.5895	0.0376	-11.0014	0.0140
-15.7178	0.0826	-9.3586	0.0590	-8.8693	0.0365	-10.7434	0.0128
-11.6515	0.0815	-10.5851	0.0578	-9.4610	0.0353	-11.2831	0.0117
-10.1740	0.0803	-10.6282	0.0567	-9.4142	0.0342	-10.7908	0.0106
-10.5483	0.0792	-10.4274	0.0556	-9.6903	0.0331	-11.0014	0.0095
-10.5433	0.0781	-9.7853	0.0545	-9.1716	0.0320	-10.8404	0.0083
-11.2223	0.0770	-9.7824	0.0533	-10.0248	0.0308		
-11.2735	0.0758	-9.4495	0.0522	-9.5514	0.0297		

Table D.19 Local Cold Wall Convective Heat Flux for W = 56.7mm, ϕ = 45°, ΔT = 15.01°C, and q_B'' = 0W/m^2

q"(W/m^2)	Y (m)	q"(W/m^2)	Y (m)	q"(W/m^2)	Y (m)	q"(W/m^2)	Y (m)
-17.2607	0.0972	-19.4508	0.0747	-17.8378	0.0511	-14.6361	0.0286
-17.5451	0.0961	-18.2670	0.0736	-18.4707	0.0500	-16.0655	0.0275
-18.1404	0.0950	-16.4423	0.0725	-17.2700	0.0488	-15.8248	0.0263
-18.7803	0.0938	-17.9664	0.0713	-16.0927	0.0477	-15.3624	0.0252
-17.9840	0.0927	-18.2748	0.0702	-15.7452	0.0466	-17.2329	0.0241
-20.9892	0.0916	-18.5912	0.0691	-18.4774	0.0455	-15.8287	0.0230
-18.7762	0.0905	-19.4434	0.0680	-16.1058	0.0443	-17.3823	0.0218
-20.0135	0.0893	-19.2697	0.0657	-17.7012	0.0432	-16.4528	0.0207
-18.6155	0.0882	-16.4486	0.0646	-16.6061	0.0421	-16.3303	0.0196
-19.2957	0.0871	-19.4434	0.0635	-14.7666	0.0410	-17.2630	0.0185
-20.7147	0.0860	-18.5993	0.0623	-15.2938	0.0398	-16.2137	0.0173
-20.7214	0.0848	-18.6020	0.0612	-14.6570	0.0387	-16.2158	0.0162
-21.1431	0.0837	-18.1302	0.0601	-14.7666	0.0376	-15.8531	0.0151
-20.5390	0.0826	-18.1314	0.0590	-13.8039	0.0365	-16.9842	0.0140
-20.5505	0.0815	-18.6047	0.0578	-14.5556	0.0353	-16.0927	0.0128
-19.7898	0.0803	-19.8173	0.0567	-14.6562	0.0342	-16.4602	0.0117
-19.7974	0.0792	-18.1327	0.0556	-14.2595	0.0331	-15.5110	0.0106
-19.0891	0.0781	-19.4567	0.0545	-14.3488	0.0320	-16.3459	0.0095
-18.7529	0.0770	-17.6841	0.0533	-14.3456	0.0308	-15.2920	0.0083
-19.4449	0.0758	-17.9891	0.0522	-14.6378	0.0297		

Table D.20 Local Hot Wall Convective Heat Flux for W = 56.7mm, ϕ = 45°, ΔT = 15.01°C, and $q_B'' = 0 W/m^2$

$q''(W/m^2)$	Y (m)	$q''(W/m^2)$	Y (m)	$q''(W/m^2)$	Y (m)	$q''(W/m^2)$	Y (m)
22.5107	0.0972	17.5964	0.0747	27.1999	0.0522	21.8478	0.0297
21.2503	0.0961	22.8383	0.0736	25.4950	0.0511	21.8460	0.0286
23.5958	0.0950	23.8234	0.0725	27.6121	0.0500	22.4453	0.0275
21.6258	0.0938	22.8402	0.0713	25.7609	0.0488	22.0498	0.0263
23.1533	0.0927	25.0489	0.0702	26.0471	0.0477	20.7542	0.0252
21.8203	0.0916	23.7299	0.0691	25.2321	0.0466	23.3273	0.0241
22.5198	0.0905	25.8447	0.0680	26.0423	0.0455	24.4989	0.0230
22.2164	0.0893	24.9478	0.0668	25.7681	0.0443	23.1225	0.0218
22.9363	0.0882	21.8581	0.0657	23.1090	0.0432	24.5270	0.0207
21.2568	0.0871	24.2265	0.0646	25.7705	0.0421	23.8193	0.0196
22.3109	0.0860	23.7562	0.0635	23.7745	0.0410	23.5020	0.0185
21.6292	0.0848	26.0276	0.0623	23.7725	0.0398	25.5794	0.0173
22.9382	0.0837	25.7538	0.0612	24.0057	0.0387	23.3039	0.0162
21.8203	0.0826	26.3074	0.0601	23.3097	0.0376	23.7705	0.0151
22.7234	0.0815	26.3248	0.0590	23.3039	0.0365	23.7867	0.0140
21.6275	0.0803	25.4926	0.0578	22.4489	0.0353	23.5738	0.0128
23.1513	0.0792	26.0301	0.0567	20.9143	0.0342	24.7797	0.0117
22.0149	0.0781	26.0374	0.0556	22.2360	0.0331	23.5040	0.0106
23.5978	0.0770	24.9792	0.0545	20.5584	0.0320	24.2118	0.0095
22.8402	0.0758	26.0374	0.0533	21.6477	0.0308	23.3039	0.0083

Table D.21 Local Cold Wall Convective Heat Flux for W = 56.7mm, ϕ = 45°, ΔT = 14.99°C, and q_B'' = 75W/m^2

q"(W/m^2)	Y (m)	q"(W/m^2)	Y (m)	q"(W/m^2)	Y (m)	q"(W/m^2)	Y (m)
-40.3669	0.0972	-39.6397	0.0747	-38.2329	0.0522	-33.9705	0.0297
-39.6215	0.0961	-46.5562	0.0736	-38.9207	0.0511	-36.9120	0.0286
-37.5472	0.0950	-39.5911	0.0725	-38.9031	0.0500	-35.0861	0.0275
-42.6331	0.0938	-41.1540	0.0713	-40.3669	0.0488	-36.8909	0.0263
-41.0101	0.0927	-37.5363	0.0702	-39.5850	0.0477	-35.0718	0.0252
-37.4382	0.0916	-42.7815	0.0691	-37.4981	0.0466	-33.9526	0.0241
-39.5123	0.0905	-38.8972	0.0680	-41.0820	0.0455	-37.5199	0.0230
-37.4545	0.0893	-40.3543	0.0668	-38.8445	0.0443	-36.2368	0.0218
-40.2850	0.0882	-37.5363	0.0657	-41.0820	0.0432	-36.8593	0.0207
-35.5808	0.0871	-37.5363	0.0646	-40.3039	0.0421	-36.2419	0.0196
-40.3102	0.0860	-37.5363	0.0635	-40.2976	0.0410	-38.1594	0.0185
-41.0689	0.0848	-38.2216	0.0623	-40.2850	0.0398	-36.8435	0.0173
-39.5668	0.0837	-37.5581	0.0612	-38.8445	0.0387	-36.8435	0.0162
-37.4981	0.0826	-38.9383	0.0601	-39.5729	0.0376	-35.6152	0.0151
-38.1820	0.0815	-36.2979	0.0590	-38.1707	0.0365	-36.8487	0.0140
-37.5254	0.0803	-38.0918	0.0578	-35.6349	0.0353	-35.0337	0.0128
-38.1990	0.0792	-41.0297	0.0567	-36.2419	0.0342	-36.2368	0.0117
-38.9031	0.0781	-36.7856	0.0556	-35.0623	0.0331	-35.0528	0.0106
-38.2103	0.0770	-36.7804	0.0545	-35.0718	0.0320	-35.6497	0.0095
-38.2160	0.0758	-38.0861	0.0533	-33.9616	0.0308	-31.9354	0.0083

Table D.22 Local Hot Wall Convective Heat Flux for W = 56.7mm, ϕ = 45°, ΔT = 14.99°C, and q_B'' = 75W/m^2

q"(W/m^2)	Y (m)	q"(W/m^2)	Y (m)	q"(W/m^2)	Y (m)	q"(W/m^2)	Y (m)
8.3101	0.0972	7.0967	0.0736	9.1101	0.0477	5.9148	0.0252
7.7427	0.0961	6.6671	0.0725	7.9881	0.0466	6.2746	0.0241
8.7251	0.0938	5.7424	0.0713	8.9749	0.0455	11.0467	0.0230
9.3196	0.0927	5.7706	0.0702	8.4325	0.0443	6.4567	0.0218
6.7692	0.0916	4.5345	0.0668	5.7064	0.0432	4.9811	0.0207
9.6059	0.0905	8.7112	0.0657	5.7591	0.0421	5.6346	0.0196
6.7502	0.0893	7.5235	0.0635	10.0562	0.0410	5.5884	0.0185
8.4959	0.0882	5.1948	0.0623	6.2723	0.0398	6.4392	0.0162
6.9207	0.0871	7.5842	0.0612	7.0405	0.0387	6.5130	0.0151
7.2101	0.0860	5.2396	0.0601	9.4745	0.0376	7.4203	0.0140
6.8801	0.0848	7.4436	0.0590	6.4884	0.0365	7.2109	0.0128
6.3333	0.0837	5.4119	0.0578	6.0887	0.0353	6.1829	0.0117
5.9936	0.0826	6.6478	0.0567	6.5224	0.0342	4.2456	0.0106
5.7143	0.0815	4.9862	0.0556	6.4372	0.0331	4.1749	0.0095
5.3667	0.0803	8.8438	0.0545	10.8049	0.0320	6.3460	0.0083
8.1715	0.0792	6.1845	0.0533	6.3717	0.0308		
4.6832	0.0781	6.8380	0.0522	6.3065	0.0297		
7.6630	0.0770	7.5481	0.0511	6.0000	0.0286		
6.3915	0.0758	8.8133	0.0500	6.4554	0.0275		
6.9108	0.0747	7.5899	0.0488	5.8164	0.0263		

Table D.23 Local Cold Wall Convective Heat Flux for W = 32.7mm, $\phi = 0°$, $\Delta T = 0°C$, and $q_B'' = 75W/m^2$

q"(W/m²)	Y (m)	q"(W/m²)	Y (m)	q"(W/m²)	Y (m)	q"(W/m²)	Y (m)
-26.1400	0.0972	-24.5106	0.0747	-24.5397	0.0511	-28.5014	0.0286
-22.6093	0.0961	-27.3951	0.0736	-22.3829	0.0500	-21.5397	0.0275
-25.0019	0.0950	-27.8270	0.0725	-23.2182	0.0488	-22.5315	0.0263
-23.2343	0.0938	-27.1701	0.0713	-19.4805	0.0477	-14.6708	0.0252
-22.5732	0.0927	-22.9972	0.0691	-19.8247	0.0466	-18.2527	0.0241
-17.5640	0.0916	-20.9066	0.0680	-19.5018	0.0455	-16.4338	0.0230
-14.3750	0.0905	-17.8256	0.0668	-14.3758	0.0443	-12.7777	0.0218
-13.4567	0.0893	-15.4358	0.0657	-12.5025	0.0432	-11.2236	0.0207
-9.9177	0.0882	-12.1694	0.0646	-9.2723	0.0421	-6.5292	0.0196
-11.2306	0.0871	-9.3495	0.0635	-6.5881	0.0410	-9.3883	0.0185
-9.8819	0.0860	-7.4647	0.0623	-5.6481	0.0398	-8.1308	0.0173
-7.1269	0.0848	-5.7469	0.0612	-6.0574	0.0387	-7.0221	0.0162
-6.4842	0.0837	-8.4741	0.0601	-6.1072	0.0376	-5.8171	0.0151
-6.1073	0.0826	-7.4841	0.0590	-6.6523	0.0365	-7.3845	0.0140
-5.4291	0.0815	-8.5991	0.0578	-10.9362	0.0353	-7.8319	0.0128
-7.5993	0.0803	-10.7099	0.0567	-11.3504	0.0342	-12.2545	0.0117
-7.1797	0.0792	-15.4590	0.0556	-17.3112	0.0331	-20.0335	0.0106
-7.6776	0.0781	-21.7247	0.0545	-23.3474	0.0320	-24.5891	0.0095
-13.5643	0.0770	-26.1477	0.0533	-25.3540	0.0308	-26.7342	0.0083
-18.7373	0.0758	-27.1646	0.0522	-26.5147	0.0297		

Table D.24 Local Hot Wall Convective Heat Flux for W = 32.7mm, $\phi = 0°$, $\Delta T = 0°C$, and $q_B'' = 75W/m^2$

$q''(W/m^2)$	Y (m)	$q''(W/m^2)$	Y (m)	$q''(W/m^2)$	Y (m)	$q''(W/m^2)$	Y (m)
-32.6623	0.0972	-33.6887	0.0747	-40.7902	0.0522	-42.3033	0.0297
-40.7035	0.0961	-32.6264	0.0736	-40.7282	0.0511	-39.3701	0.0286
-36.1908	0.0950	-40.8710	0.0725	-31.2931	0.0500	-28.9505	0.0275
-29.6453	0.0938	-36.2692	0.0713	-24.3477	0.0488	-22.0264	0.0263
-24.0699	0.0927	-31.3517	0.0702	-25.3662	0.0477	-23.5682	0.0252
-19.7346	0.0916	-29.2601	0.0691	-22.1941	0.0466	-21.6021	0.0241
-17.7645	0.0905	-25.1166	0.0680	-17.8818	0.0455	-16.2540	0.0230
-20.2214	0.0893	-20.0685	0.0668	-15.2774	0.0443	-19.3792	0.0218
-16.1035	0.0882	-19.0839	0.0657	-13.1017	0.0432	-15.1615	0.0207
-14.7598	0.0871	-15.2756	0.0646	-12.4696	0.0421	-13.8937	0.0196
-12.5126	0.0860	-16.2135	0.0635	-14.8655	0.0410	-11.4114	0.0185
-10.7546	0.0848	-15.3517	0.0623	-12.0528	0.0398	-12.3057	0.0173
-10.7594	0.0837	-13.2350	0.0612	-10.7585	0.0387	-11.6312	0.0162
-9.5545	0.0826	-11.8096	0.0601	-10.0576	0.0376	-10.1923	0.0151
-9.1398	0.0815	-10.3709	0.0590	-10.1537	0.0365	-10.0242	0.0140
-8.5979	0.0803	-11.2372	0.0578	-10.1035	0.0353	-10.1595	0.0128
-9.4150	0.0792	-13.8064	0.0567	-12.7417	0.0342	-11.8400	0.0117
-10.2012	0.0781	-16.1083	0.0556	-15.3614	0.0331	-15.0105	0.0106
-11.0177	0.0770	-9.6235	0.0545	-19.4256	0.0320	-14.5943	0.0095
-18.3044	0.0758	-29.2569	0.0533	-28.5495	0.0308	-27.8696	0.0083

Table D.25 Local Cold Wall Convective Heat Flux for W = 32.7mm, ϕ = 0°, ΔT = 0.05°C, and q_B'' = 150.09W/m^2

q"(W/m^2)	Y (m)	q"(W/m^2)	Y (m)	q"(W/m^2)	Y (m)	q"(W/m^2)	Y (m)
-52.8945	0.0972	-62.9486	0.0747	-52.8430	0.0522	-54.0619	0.0297
-52.9872	0.0961	-61.3160	0.0736	-45.5787	0.0511	-48.4457	0.0286
-46.3951	0.0950	-49.6400	0.0725	-42.3023	0.0500	-41.5332	0.0275
-44.6650	0.0938	-51.5797	0.0713	-39.9872	0.0488	-39.2993	0.0263
-39.3793	0.0927	-45.5022	0.0702	-36.8491	0.0477	-33.1143	0.0252
-34.6777	0.0916	-39.3507	0.0691	-31.3684	0.0466	-29.7514	0.0241
-32.6017	0.0905	-30.1272	0.0680	-26.0808	0.0455	-24.1722	0.0230
-24.1852	0.0893	-26.6877	0.0668	-23.8492	0.0443	-22.0430	0.0218
-24.1246	0.0882	-24.3667	0.0657	-19.6243	0.0432	-18.2342	0.0207
-20.1435	0.0871	-18.0777	0.0646	-17.1604	0.0421	-11.6842	0.0196
-16.7936	0.0860	-14.6494	0.0635	-12.5125	0.0410	-11.5758	0.0185
-10.0137	0.0848	-14.1228	0.0623	-13.0096	0.0398	-13.4686	0.0173
-10.4307	0.0837	-16.0869	0.0612	-15.7568	0.0387	-16.7852	0.0162
-12.4593	0.0826	-23.8936	0.0601	-25.1888	0.0376	-26.0205	0.0151
-16.4352	0.0815	-29.3913	0.0590	-32.7202	0.0365	-34.6288	0.0140
-23.3959	0.0803	-42.9910	0.0578	-44.5988	0.0353	-52.9769	0.0128
-37.3550	0.0792	-55.4964	0.0567	-54.0942	0.0342	-58.1182	0.0117
-48.3939	0.0781	-58.1554	0.0556	-62.8469	0.0331	-59.7923	0.0106
-56.8186	0.0770	-59.6351	0.0545	-59.5698	0.0320	-56.8304	0.0095
-61.2747	0.0758	-61.2471	0.0533	-55.2820	0.0308	-49.5495	0.0083

Table D.26 Local Hot Wall Convective Heat Flux for W = 32.7mm, $\phi = 0°$, $\Delta T = 0.05°C$, and $q_B'' = 150.09 W/m^2$

q"(W/m²)	Y (m)	q"(W/m²)	Y (m)	q"(W/m²)	Y (m)	q"(W/m²)	Y (m)
-68.4574	0.0972	-77.8300	0.0747	-66.4607	0.0522	-66.6256	0.0297
-59.6494	0.0961	-72.7350	0.0736	-62.9448	0.0511	-61.1272	0.0286
-56.7777	0.0950	-59.5567	0.0725	-55.4317	0.0500	-56.7417	0.0275
-52.7041	0.0938	-56.6938	0.0713	-51.5522	0.0488	-49.4752	0.0263
-50.4591	0.0927	-55.4203	0.0702	-47.3743	0.0477	-46.3692	0.0252
-43.7727	0.0916	-51.5324	0.0691	-42.2062	0.0466	-41.4130	0.0241
-40.7232	0.0905	-45.4753	0.0680	-36.8400	0.0455	-36.8248	0.0230
-35.1542	0.0893	-40.6985	0.0668	-35.0714	0.0443	-37.9470	0.0218
-31.3616	0.0882	-36.8450	0.0657	-31.2847	0.0432	-30.8467	0.0207
-29.6527	0.0871	-30.1282	0.0646	-25.9999	0.0421	-27.2461	0.0196
-25.6991	0.0860	-27.5305	0.0635	-21.4186	0.0410	-23.4063	0.0185
-21.0251	0.0848	-25.4270	0.0623	-19.4481	0.0398	-21.1940	0.0173
-19.1190	0.0837	-20.4681	0.0612	-17.8026	0.0387	-20.2828	0.0162
-19.4149	0.0826	-22.4674	0.0601	-19.4524	0.0376	-20.8539	0.0151
-17.0119	0.0815	-27.5446	0.0590	-24.3627	0.0365	-23.8505	0.0140
-20.4775	0.0803	-37.4506	0.0578	-35.6101	0.0353	-31.6977	0.0128
-27.8759	0.0792	-54.0063	0.0567	-52.8391	0.0342	-42.2328	0.0117
-38.6956	0.0781	-70.6706	0.0556	-64.4996	0.0331	-59.6096	0.0106
-46.3452	0.0770	-75.0912	0.0545	-75.2384	0.0320	-72.9918	0.0095
-66.5761	0.0758	-75.1122	0.0533	-66.5101	0.0308	-68.5798	0.0083

Table D.27 Local Cold Wall Convective Heat Flux for W = 32.7mm, ϕ = 0°, ΔT = 15.04°C, and q_B'' = 0W/m^2

q"(W/m^2)	Y (m)	q"(W/m^2)	Y (m)	q"(W/m^2)	Y (m)	q"(W/m^2)	Y (m)
-33.1820	0.0972	-32.6514	0.0747	-33.1095	0.0511	-31.6549	0.0263
-34.2421	0.0961	-37.2036	0.0736	-31.6355	0.0488	-32.6307	0.0252
-34.2466	0.0950	-34.2285	0.0725	-34.1831	0.0477	-30.7542	0.0241
-32.6803	0.0938	-30.3585	0.0702	-34.7323	0.0466	-30.7652	0.0230
-30.3728	0.0927	-31.7212	0.0691	-32.1374	0.0455	-31.2396	0.0218
-33.7345	0.0916	-33.7213	0.0680	-33.6685	0.0443	-31.7251	0.0207
-34.6856	0.0905	-31.7290	0.0668	-30.3370	0.0432	-29.9728	0.0196
-31.2813	0.0893	-30.8351	0.0657	-31.2434	0.0421	-28.7886	0.0185
-32.5894	0.0882	-29.8443	0.0646	-28.7533	0.0410	-26.5484	0.0173
-35.3044	0.0871	-26.5210	0.0635	-28.0173	0.0398	-24.4349	0.0162
-30.7431	0.0860	-27.2170	0.0623	-27.5670	0.0387	-24.7333	0.0151
-29.4817	0.0848	-24.7215	0.0612	-26.2316	0.0376	-24.1732	0.0140
-26.5758	0.0837	-23.3842	0.0601	-24.1618	0.0365	-26.9010	0.0128
-27.9869	0.0826	-22.1727	0.0590	-26.8982	0.0353	-31.1867	0.0117
-25.0537	0.0815	-23.6617	0.0578	-28.6892	0.0342	-32.5894	0.0106
-22.2015	0.0803	-26.5731	0.0567	-30.7321	0.0331	-35.4158	0.0095
-23.9526	0.0792	-29.9067	0.0556	-32.0974	0.0320	-33.6027	0.0083
-25.9720	0.0781	-32.6307	0.0545	-34.7136	0.0297		
-28.3696	0.0770	-32.6059	0.0533	-33.1053	0.0286		
-30.3513	0.0758	-37.1501	0.0522	-33.1095	0.0275		

Table D.28 Local Hot Wall Convective Heat Flux for W = 32.7mm, ϕ = 0°, ΔT = 15.04°C, and q_B'' = 0W/m^2

q''(W/m^2)	Y (m)	q''(W/m^2)	Y (m)	q''(W/m^2)	Y (m)	q''(W/m^2)	Y (m)
20.5088	0.0972	50.3637	0.0747	32.3567	0.0522	25.5829	0.0297
22.7507	0.0961	23.6459	0.0736	19.0184	0.0511	18.0338	0.0286
20.1123	0.0950	32.7730	0.0725	19.3027	0.0500	22.3766	0.0275
21.5199	0.0938	22.5146	0.0713	22.5860	0.0488	22.7098	0.0263
24.5383	0.0927	22.5037	0.0702	24.0474	0.0477	24.3127	0.0252
26.1171	0.0916	24.7903	0.0691	25.5688	0.0466	25.6159	0.0241
27.9187	0.0905	26.9905	0.0680	26.9905	0.0455	25.8040	0.0230
29.6131	0.0893	28.2396	0.0668	26.1442	0.0443	29.1957	0.0218
30.7512	0.0882	26.4379	0.0657	29.2666	0.0432	27.9131	0.0207
30.0197	0.0871	29.2789	0.0646	28.9281	0.0421	28.2540	0.0196
31.1619	0.0860	29.2882	0.0635	29.6289	0.0410	29.2851	0.0185
34.1811	0.0848	29.2944	0.0623	28.9401	0.0398	29.2974	0.0173
31.1689	0.0837	30.3810	0.0612	28.2827	0.0387	28.9764	0.0162
32.8428	0.0826	30.0197	0.0601	28.2914	0.0376	27.5721	0.0151
31.5801	0.0815	34.6763	0.0590	29.6573	0.0365	27.9019	0.0140
30.6662	0.0803	31.6160	0.0578	30.2948	0.0353	30.7375	0.0128
33.1723	0.0792	34.1642	0.0567	36.1433	0.0342	30.4010	0.0117
33.6712	0.0781	44.0022	0.0556	42.5003	0.0331	32.7768	0.0106
35.1682	0.0770	46.6099	0.0545	22.9767	0.0320	39.1007	0.0095
44.8481	0.0758	49.1680	0.0533	49.3345	0.0308	49.3170	0.0083

Table D.29 Local Cold Wall Convective Heat Flux for W = 32.7mm, $\phi = 0°$, $\Delta T = 15°C$, and $q_B'' = 75W/m^2$

q''(W/m²)	Y (m)	q''(W/m²)	Y (m)	q''(W/m²)	Y (m)	q''(W/m²)	Y (m)
-46.1736	0.0972	-41.7114	0.0747	-57.1041	0.0511	-58.8070	0.0286
-55.7108	0.0961	-47.1266	0.0736	-57.2422	0.0500	-60.3757	0.0275
-55.6631	0.0950	-54.4179	0.0725	-62.2079	0.0488	-63.9504	0.0263
-60.3058	0.0938	-58.8335	0.0713	-63.9974	0.0477	-60.3338	0.0252
-65.8763	0.0927	-58.7937	0.0702	-62.1635	0.0466	-62.0747	0.0241
-64.1389	0.0916	-64.0131	0.0680	-60.4037	0.0455	-62.1043	0.0230
-64.1546	0.0905	-60.4317	0.0668	-62.1931	0.0443	-62.1191	0.0218
-63.9191	0.0893	-60.4317	0.0657	-58.7937	0.0432	-60.4457	0.0207
-63.9191	0.0882	-57.2296	0.0646	-58.8601	0.0421	-60.4877	0.0196
-62.0895	0.0871	-57.2548	0.0635	-57.1041	0.0410	-53.0753	0.0185
-63.9661	0.0860	-51.7870	0.0623	-50.4224	0.0398	-54.2591	0.0173
-57.1919	0.0848	-52.8918	0.0612	-54.3498	0.0387	-48.2449	0.0162
-55.7585	0.0837	-46.3217	0.0601	-45.2505	0.0376	-45.2663	0.0151
-51.7664	0.0826	-42.5154	0.0590	-45.3215	0.0365	-37.4340	0.0140
-47.2466	0.0815	-40.9761	0.0578	-40.1229	0.0353	-38.6856	0.0128
-45.3374	0.0803	-34.4418	0.0567	-38.7145	0.0342	-37.3692	0.0117
-41.6712	0.0792	-36.8355	0.0556	-37.3800	0.0331	-40.1478	0.0106
-42.5782	0.0781	-37.4394	0.0545	-43.3727	0.0320	-46.1162	0.0095
-37.3962	0.0770	-46.2476	0.0533	-49.2956	0.0308	-53.0428	0.0083
-42.6061	0.0758	-51.6841	0.0522	-54.4065	0.0297		

Table D.30 Local Cold Wall Convective Heat Flux for W = 32.7mm, ϕ = 45°, ΔT = 0.03°C, and q_B'' = 75.03W/m^2

q"(W/m^2)	Y (m)	q"(W/m^2)	Y (m)	q"(W/m^2)	Y (m)	q"(W/m^2)	Y (m)
-4.6431	0.0972	-5.5563	0.0747	-5.5111	0.0522	-6.7006	0.0297
-7.7775	0.0961	-9.9065	0.0736	-6.9435	0.0511	-10.4416	0.0286
-5.4073	0.0950	-8.6844	0.0725	-6.3720	0.0500	-6.9762	0.0275
-5.5283	0.0938	-8.5609	0.0713	-7.0587	0.0488	-8.8809	0.0263
-5.5425	0.0927	-9.2940	0.0702	-7.9569	0.0477	-9.8335	0.0252
-7.3785	0.0916	-12.3443	0.0691	-11.4741	0.0466	-17.0442	0.0241
-11.8989	0.0905	-17.7438	0.0680	-16.5017	0.0455	-19.8655	0.0230
-15.3704	0.0893	-20.2628	0.0668	-21.3462	0.0443	-25.1717	0.0218
-20.6345	0.0882	-24.5773	0.0657	-24.1659	0.0432	-27.6348	0.0207
-24.9447	0.0871	-24.4013	0.0646	-27.2714	0.0421	-25.7079	0.0196
-29.4989	0.0860	-20.9719	0.0635	-26.9338	0.0410	-25.4321	0.0185
-28.0140	0.0848	-23.3846	0.0623	-24.8628	0.0398	-22.6271	0.0173
-25.7830	0.0837	-23.8060	0.0612	-23.8145	0.0387	-21.1557	0.0162
-27.2630	0.0826	-23.0956	0.0601	-21.7627	0.0376	-17.8235	0.0151
-20.5433	0.0815	-22.1995	0.0590	-17.8139	0.0365	-15.8363	0.0140
-22.6406	0.0803	-17.5327	0.0578	-17.0212	0.0353	-16.7336	0.0128
-22.6852	0.0792	-14.9776	0.0567	-12.2894	0.0342	-15.7032	0.0117
-15.9361	0.0781	-12.4246	0.0556	-9.0770	0.0331	-12.4223	0.0106
-13.9659	0.0770	-10.7689	0.0545	-11.4055	0.0320	-8.3653	0.0095
-10.5763	0.0758	-7.1975	0.0533	-7.3740	0.0308	-6.1381	0.0083

Table D.31 Local Hot Wall Convective Heat Flux for W = 32.7mm, ϕ = 45°, ΔT = 0.03°C, and q_B'' = 75.03W/m^2

q"(W/m^2)	Y (m)	q"(W/m^2)	Y (m)	q"(W/m^2)	Y (m)	q"(W/m^2)	Y (m)
-18.7542	0.0972	-16.3972	0.0736	-21.3474	0.0511	-20.8101	0.0286
-18.1129	0.0961	-20.4163	0.0725	-21.1399	0.0500	-23.3208	0.0275
-20.5953	0.0950	-22.9004	0.0713	-20.3786	0.0488	-22.1787	0.0263
-20.0385	0.0938	-20.5825	0.0702	-19.8467	0.0477	-20.9546	0.0252
-18.8567	0.0927	-17.3934	0.0691	-20.3974	0.0466	-20.0310	0.0241
-19.1908	0.0916	-17.1418	0.0680	-14.6744	0.0455	-17.5487	0.0230
-17.6926	0.0905	-16.8995	0.0668	-15.1920	0.0443	-14.7947	0.0218
-15.7183	0.0893	-13.0047	0.0657	-16.1310	0.0432	-14.9598	0.0207
-13.3086	0.0882	-9.8752	0.0646	-12.6766	0.0421	-12.9161	0.0196
-11.4272	0.0871	-11.8206	0.0635	-11.5214	0.0410	-9.7838	0.0185
-12.6833	0.0860	-10.7027	0.0623	-9.5315	0.0398	-10.8470	0.0173
-10.4490	0.0848	-9.2163	0.0612	-9.2250	0.0387	-9.4078	0.0162
-9.4895	0.0837	-8.8250	0.0601	-9.4639	0.0376	-9.0393	0.0151
-8.0649	0.0826	-9.1934	0.0590	-9.6733	0.0365	-10.2021	0.0140
-7.6299	0.0815	-10.0521	0.0578	-10.4376	0.0353	-11.1129	0.0128
-7.6063	0.0803	-10.9280	0.0567	-11.9254	0.0342	-11.3466	0.0117
-9.5883	0.0792	-12.4297	0.0556	-13.1745	0.0331	-13.9246	0.0106
-10.1978	0.0781	-14.7939	0.0545	-15.3138	0.0320	-15.6960	0.0095
-14.1586	0.0758	-16.6336	0.0533	-18.0060	0.0308	-17.3299	0.0083
-16.4124	0.0747	-19.0148	0.0522	-19.5543	0.0297		

Table D.32 Local Cold Wall Convective Heat Flux for W = 32.7mm, ϕ = 45°, ΔT = 0.02°C, and q_B'' = 149.99W/m^2

q"(W/m^2)	Y (m)	q"(W/m^2)	Y (m)	q"(W/m^2)	Y (m)	q"(W/m^2)	Y (m)
-28.4971	0.0972	-30.8563	0.0747	-23.2470	0.0522	-24.2482	0.0297
-23.4988	0.0961	-24.2726	0.0736	-21.1103	0.0511	-19.8141	0.0286
-19.3165	0.0950	-16.1548	0.0725	-14.8785	0.0500	-15.5008	0.0275
-14.9838	0.0938	-17.7751	0.0713	-14.6130	0.0488	-14.6975	0.0263
-12.1126	0.0927	-14.8569	0.0702	-14.3805	0.0477	-15.6151	0.0252
-14.1954	0.0916	-17.5069	0.0691	-15.6233	0.0466	-20.7493	0.0241
-13.8107	0.0905	-23.4781	0.0680	-22.3046	0.0455	-25.9305	0.0230
-19.5043	0.0893	-29.7158	0.0668	-29.6794	0.0443	-34.5918	0.0218
-27.5017	0.0882	-38.7958	0.0657	-38.0925	0.0432	-46.8450	0.0207
-35.7888	0.0871	-47.9044	0.0646	-47.6392	0.0421	-52.1647	0.0196
-44.0244	0.0860	-54.7434	0.0635	-54.6874	0.0410	-55.9954	0.0185
-54.5420	0.0848	-56.0660	0.0623	-60.4881	0.0398	-58.8995	0.0173
-62.2226	0.0837	-62.2661	0.0612	-57.3923	0.0387	-53.3536	0.0162
-63.9675	0.0826	-56.1013	0.0601	-60.5018	0.0376	-50.9887	0.0151
-60.5704	0.0815	-46.8203	0.0590	-52.1953	0.0365	-49.9486	0.0140
-55.8898	0.0803	-43.9445	0.0578	-43.2328	0.0353	-45.7526	0.0128
-55.9719	0.0792	-46.7628	0.0567	-48.7532	0.0342	-39.4087	0.0117
-46.7874	0.0781	-39.4671	0.0556	-37.4773	0.0331	-38.7902	0.0106
-40.9320	0.0770	-33.6414	0.0545	-31.7332	0.0320	-30.4828	0.0095
-38.7169	0.0758	-31.6879	0.0533	-25.3758	0.0308	-24.0474	0.0083

Table D.33 Local Hot Wall Convective Heat Flux for W = 32.7mm, ϕ = 45°, ΔT = 0.02°C, and q_B'' = 149.99W/m^2

q"(W/m^2)	Y (m)	q"(W/m^2)	Y (m)	q"(W/m^2)	Y (m)	q"(W/m^2)	Y (m)
-22.9696	0.0972	-26.1876	0.0736	-34.0689	0.0511	-35.1270	0.0286
-32.0789	0.0961	-30.3535	0.0725	-41.5259	0.0500	-38.6797	0.0275
-33.6016	0.0950	-35.5903	0.0713	-47.6060	0.0488	-46.6330	0.0263
-38.7191	0.0938	-42.9901	0.0702	-50.7656	0.0477	-49.6885	0.0252
-40.7524	0.0927	-43.9750	0.0691	-49.6236	0.0466	-50.8141	0.0241
-43.8880	0.0916	-44.6362	0.0680	-49.6421	0.0455	-50.8626	0.0230
-51.9817	0.0905	-43.1225	0.0668	-46.6003	0.0443	-50.6980	0.0218
-44.7639	0.0893	-43.8013	0.0657	-44.7940	0.0432	-44.7413	0.0207
-43.0667	0.0882	-36.6858	0.0646	-38.6966	0.0421	-38.6909	0.0196
-41.5194	0.0871	-36.7314	0.0635	-37.9480	0.0410	-35.5570	0.0185
-39.3758	0.0860	-32.0789	0.0623	-32.0596	0.0398	-33.5085	0.0173
-34.0776	0.0848	-28.4847	0.0612	-28.1067	0.0387	-29.6129	0.0162
-32.0441	0.0837	-25.9081	0.0601	-24.4891	0.0376	-23.5017	0.0151
-28.8011	0.0826	-20.1610	0.0590	-20.3299	0.0365	-21.4383	0.0140
-24.4710	0.0815	-18.9257	0.0578	-17.5210	0.0353	-19.2841	0.0128
-21.2677	0.0803	-16.4548	0.0567	-16.5151	0.0342	-17.9221	0.0117
-18.3470	0.0792	-17.8895	0.0556	-16.8839	0.0331	-18.3775	0.0106
-16.8549	0.0781	-18.3104	0.0545	-19.4116	0.0320	-19.6505	0.0095
-16.4885	0.0770	-23.1930	0.0533	-24.5523	0.0308	-23.5349	0.0083
-18.9758	0.0758	-28.9044	0.0522	-30.8877	0.0297		

Table D.34 Local Cold Wall Convective Heat Flux for W = 32.7mm, ϕ = 45°, ΔT = 15.01°C, and $q_B'' = 0 W/m^2$

q"(W/m²)	Y (m)	q"(W/m²)	Y (m)	q"(W/m²)	Y (m)	q"(W/m²)	Y (m)
-27.9655	0.0972	-29.4734	0.0736	-25.3246	0.0500	-28.6483	0.0275
-26.9067	0.0961	-29.0715	0.0725	-24.4695	0.0488	-27.9198	0.0263
-26.5934	0.0950	-30.7449	0.0713	-24.1099	0.0477	-26.8785	0.0252
-25.2447	0.0938	-28.6740	0.0702	-23.3336	0.0466	-26.2201	0.0241
-21.9690	0.0927	-29.0550	0.0691	-22.1268	0.0455	-23.3570	0.0230
-22.3608	0.0916	-30.3043	0.0680	-23.8669	0.0443	-25.3046	0.0218
-18.9827	0.0905	-29.0583	0.0668	-23.3400	0.0432	-26.5658	0.0207
-21.2678	0.0893	-27.9137	0.0657	-24.9736	0.0421	-25.6111	0.0196
-23.1311	0.0882	-29.4802	0.0635	-27.2014	0.0410	-25.0053	0.0185
-25.3196	0.0871	-27.9381	0.0623	-27.5441	0.0398	-25.9251	0.0173
-28.3404	0.0860	-28.7061	0.0612	-28.2653	0.0387	-26.5658	0.0162
-27.5916	0.0848	-27.5916	0.0601	-27.9930	0.0376	-28.7190	0.0151
-25.2846	0.0837	-27.5856	0.0590	-29.5209	0.0365	-26.9039	0.0140
-26.8954	0.0826	-29.1045	0.0578	-29.9249	0.0353	-27.9594	0.0128
-23.8647	0.0815	-27.2303	0.0567	-30.7745	0.0342	-27.5975	0.0117
-29.5073	0.0803	-28.3184	0.0556	-29.9145	0.0331	-27.2535	0.0106
-27.5886	0.0792	-26.5521	0.0545	-29.0979	0.0320	-27.2535	0.0095
-26.8813	0.0781	-26.2281	0.0533	-28.3341	0.0308	-24.4392	0.0083
-27.5678	0.0770	-26.2416	0.0522	-27.6124	0.0297		
-27.9289	0.0758	-25.0151	0.0511	-27.6272	0.0286		

Table D.35 Local Hot Wall Convective Heat Flux for W = 32.7mm, ϕ = 45°, ΔT = 15.01°C, and $q_B'' = 0 W/m^2$

q"(W/m²)	Y (m)	q"(W/m²)	Y (m)	q"(W/m²)	Y (m)	q"(W/m²)	Y (m)
30.6068	0.0972	26.6234	0.0747	28.8463	0.0522	26.2645	0.0297
31.0224	0.0961	26.3168	0.0736	26.8462	0.0511	26.8669	0.0286
34.0619	0.0950	26.0195	0.0725	29.1050	0.0500	27.5140	0.0275
35.5653	0.0938	25.2033	0.0713	27.7797	0.0488	30.2450	0.0263
37.2126	0.0927	23.5056	0.0702	29.8242	0.0477	29.5432	0.0252
37.2425	0.0916	21.8274	0.0691	29.4743	0.0466	32.7113	0.0241
37.2625	0.0905	21.8171	0.0680	29.4711	0.0455	31.8810	0.0230
37.6951	0.0893	21.8240	0.0668	25.7647	0.0443	31.3429	0.0218
37.7002	0.0882	20.0375	0.0657	30.1956	0.0432	30.7049	0.0207
38.8995	0.0871	21.0830	0.0646	24.7207	0.0421	29.8370	0.0196
41.5361	0.0860	22.0397	0.0635	27.1813	0.0410	29.4868	0.0185
36.5727	0.0848	21.0894	0.0623	28.1046	0.0398	28.8045	0.0173
32.2383	0.0837	20.3907	0.0612	24.9530	0.0387	27.8243	0.0162
33.5494	0.0826	21.2810	0.0601	25.4774	0.0376	27.2213	0.0151
35.6155	0.0815	22.6631	0.0590	23.3014	0.0365	24.5057	0.0140
33.1824	0.0803	22.2561	0.0578	25.2193	0.0353	27.2399	0.0128
31.4601	0.0792	23.5494	0.0567	23.7560	0.0342	25.5430	0.0117
29.9109	0.0781	25.5172	0.0556	23.3151	0.0331	23.9601	0.0106
21.2589	0.0770	28.4896	0.0545	25.5078	0.0320	26.8514	0.0095
30.6068	0.0758	30.2648	0.0533	26.3642	0.0308	26.8669	0.0083

Table D.36 Local Cold Wall Convective Heat Flux for W = 32.7mm, ϕ = 45°, ΔT = 14.99°C, and q_B'' = 75W/m^2

q"(W/m^2)	Y (m)	q"(W/m^2)	Y (m)	q"(W/m^2)	Y (m)	q"(W/m^2)	Y (m)
-54.5794	0.0972	-54.7997	0.0747	-42.7401	0.0522	-54.5910	0.0297
-49.5371	0.0961	-53.2168	0.0736	-41.7571	0.0511	-53.2718	0.0286
-50.7657	0.0950	-49.4895	0.0725	-39.4693	0.0500	-50.7557	0.0275
-44.4412	0.0938	-48.4028	0.0713	-38.0823	0.0488	-48.4666	0.0263
-41.0659	0.0927	-48.4301	0.0702	-34.9782	0.0477	-45.4036	0.0252
-33.3672	0.0916	-45.3555	0.0691	-34.9877	0.0466	-46.4420	0.0241
-33.7863	0.0905	-45.3635	0.0680	-35.0020	0.0455	-44.4796	0.0230
-34.9116	0.0893	-44.4259	0.0668	-36.8000	0.0443	-45.4436	0.0218
-39.6030	0.0882	-46.3918	0.0657	-42.6622	0.0432	-46.4001	0.0207
-43.4306	0.0871	-46.3751	0.0646	-47.3803	0.0421	-42.6692	0.0196
-47.4676	0.0860	-47.4327	0.0635	-47.3455	0.0410	-47.4327	0.0185
-47.2498	0.0848	-47.4152	0.0623	-49.5180	0.0398	-49.6612	0.0173
-50.8358	0.0837	-49.6421	0.0612	-49.4895	0.0387	-48.5214	0.0162
-53.3600	0.0826	-46.3751	0.0601	-50.8458	0.0376	-50.8358	0.0151
-52.0778	0.0815	-46.3918	0.0590	-53.1728	0.0365	-49.6421	0.0140
-54.7416	0.0803	-48.4940	0.0578	-56.1967	0.0353	-52.0883	0.0128
-53.3710	0.0792	-47.4327	0.0567	-57.4741	0.0342	-52.0778	0.0117
-54.7649	0.0781	-47.4327	0.0556	-54.7532	0.0331	-50.8559	0.0106
-49.6325	0.0770	-46.4169	0.0545	-55.9772	0.0320	-52.1094	0.0095
-47.0847	0.0758	-45.4436	0.0533	-51.8995	0.0308	-50.6559	0.0083

Table D.37 Local Hot Wall Convective Heat Flux for W = 32.7mm, ϕ = -45°, ΔT = 15°C, and $q_B'' = 0 W/m^2$

$q''(W/m^2)$	Y (m)	$q''(W/m^2)$	Y (m)	$q''(W/m^2)$	Y (m)	$q''(W/m^2)$	Y (m)
25.9563	0.0972	25.3799	0.0747	28.0022	0.0522	26.5238	0.0297
31.2569	0.0961	24.9000	0.0736	25.9344	0.0511	27.1141	0.0286
31.2640	0.0950	25.1685	0.0725	27.0955	0.0500	27.4273	0.0275
30.8783	0.0938	26.8157	0.0713	27.1035	0.0488	26.8313	0.0263
32.5269	0.0927	29.3949	0.0702	28.7054	0.0477	28.0732	0.0252
30.5020	0.0916	27.1167	0.0691	29.4012	0.0466	28.7233	0.0241
34.8574	0.0905	26.2457	0.0680	25.9806	0.0455	29.0568	0.0230
35.3677	0.0893	27.0875	0.0668	28.7025	0.0443	28.0362	0.0218
33.8921	0.0882	22.7861	0.0657	27.0928	0.0432	26.2159	0.0207
33.3989	0.0871	22.5529	0.0646	23.8831	0.0421	22.9897	0.0196
28.9959	0.0860	20.8173	0.0635	21.7308	0.0410	21.1840	0.0185
23.7160	0.0848	19.3229	0.0623	19.1629	0.0398	22.7636	0.0173
21.2229	0.0837	19.1695	0.0612	18.7200	0.0387	20.1221	0.0162
19.8320	0.0826	19.6315	0.0601	19.6245	0.0376	21.1840	0.0151
18.6247	0.0815	21.7239	0.0590	20.4434	0.0365	20.3105	0.0140
19.8292	0.0803	21.9280	0.0578	21.5404	0.0353	22.9973	0.0128
23.8954	0.0792	23.1853	0.0567	23.8728	0.0342	23.2203	0.0117
20.8439	0.0781	23.6412	0.0556	22.9840	0.0331	23.9223	0.0106
20.5039	0.0770	25.3590	0.0545	22.1643	0.0320	25.9685	0.0095
23.9161	0.0758	25.3753	0.0533	25.3985	0.0308	25.7042	0.0083

Table D.38 Local Cold Wall Convective Heat Flux for W = 32.7mm, ϕ = -45°, ΔT = 15°C, and $q_B'' = 0 W/m^2$

q"(W/m²)	Y (m)	q"(W/m²)	Y (m)	q"(W/m²)	Y (m)	q"(W/m²)	Y (m)
-20.2453	0.0972	-17.2078	0.0736	-19.8802	0.0511	-21.4688	0.0286
-22.1473	0.0961	-18.3999	0.0725	-21.0518	0.0500	-19.8555	0.0275
-21.0483	0.0950	-19.2227	0.0713	-22.3720	0.0488	-22.6033	0.0263
-20.8323	0.0938	-17.9128	0.0702	-22.8456	0.0477	-24.1416	0.0252
-21.0362	0.0927	-20.3079	0.0691	-22.8395	0.0466	-24.1461	0.0241
-24.1348	0.0916	-20.7041	0.0680	-27.2310	0.0455	-24.4275	0.0230
-23.3376	0.0905	-20.2934	0.0668	-23.0827	0.0443	-24.4345	0.0218
-23.3397	0.0893	-21.5139	0.0657	-25.2823	0.0432	-23.8957	0.0207
-22.5914	0.0882	-21.2989	0.0646	-24.4112	0.0421	-24.1803	0.0196
-22.2126	0.0871	-21.0882	0.0635	-23.3333	0.0410	-23.6526	0.0185
-23.0848	0.0860	-20.4705	0.0623	-23.0869	0.0398	-23.9471	0.0173
-21.7609	0.0848	-19.1781	0.0612	-20.2260	0.0387	-22.8354	0.0162
-20.6207	0.0837	-19.7116	0.0601	-23.0869	0.0376	-22.1320	0.0151
-19.3888	0.0826	-19.5385	0.0590	-22.3642	0.0365	-21.9214	0.0140
-20.2356	0.0815	-20.2805	0.0578	-21.0344	0.0353	-20.8629	0.0128
-18.7163	0.0803	-19.0127	0.0567	-20.5164	0.0342	-20.8629	0.0117
-18.7218	0.0792	-19.5236	0.0556	-20.4296	0.0331	-21.4994	0.0106
-18.3959	0.0781	-18.8391	0.0545	-21.0431	0.0320	-19.9034	0.0095
-18.5641	0.0770	-19.0014	0.0533	-20.6356	0.0308	-18.8488	0.0083
-16.9388	0.0758	-19.6949	0.0522	-21.4688	0.0297		

References

Almeida, F., Naylor, D. and Oosthuizen, P. H. (2008). An Interferometric Study of Free Convection in a Window with a Heated Between-Panes Blind. *3rd Canadian Solar Buildings Research Network Conference,* Fredericton.

ASHRAE Fundamentals Handbook. (2005). Fenestration (F31). Atlanta, Georgia.

Avedissian, T. and D. Naylor. (2007). Free Convective Heat Transfer in an Enclosure with an Internal Louvered Blind. *International Journal of Heat and Mass Transfer*, 51 (1-2), 283 - 293.

Batchelor, G.K. (1954). Heat Transfer by Free Convection Across a Closed Cavity Between Vertical Boundaries at Different Temperatures. *Quarterly of Applied Mathematics, 12(3),* 209-233.

Chait, A., and Korpela, S. A. (1989). Secondary flow and its stability for natural convection in a tall vertical enclosure. *Journal of Fluid Mechanics, 200*, 189-216.

Collins, M., Harrison, S. J., Naylor, D., and Oosthuizen, P. H. (2002). Heat transfer from an isothermal vertical surface with adjacent heated horizontal louvers: Numerical analysis. *Journal of Heat Transfer, 124*(6), 1072-1077.

Collins, M., Harrison, S. J., Naylor, D., and Oosthuizen, P. H. (2002). Heat transfer from an isothermal vertical surface with adjacent heated horizontal louvers: Validation. *Journal of Heat Transfer, 124*(6), 1078-1087.

Collins, M. (2004). Convective heat transfer coefficients from an internal window surface and adjacent sunlit venetian blind. *Energy and Buildings, 36*(3), 309-318.

Collins, M. R., and Harrison, S. J. (2004). Estimating the solar heat and thermal gain from a window with an interior venetian blind. *ASHRAE Transactions 110(1),* 486-500.

Collins, M. R., and Wright, J. L. (2006). Calculating center-glass performance indices of windows with a diathermanous layer. *ASHRAE Transactions 112(2),* 22-29.

Collins, M., Tasnim, S., Wright, J., 2008, Determination of the Convective Heat Transfer for Fenestration with Between-the-Glass Louvered Shades, *International Journal of Heat and Mass Transfer*, vol. 51, pp. 2742-2751.

Duarte, N., (2000). An Experimental Study of Free Convective Heat Transfer from a Vertical Plate in the Presence of Heated Venetian Blinds. *M.E.Sc. Thesis, University of Western Ontario.*

Duarte, N., Naylor, D., Oosthuizen, P. H., and Harrison, S. J. (2001). An interferometric study of free convection at a window glazing with a heated venetian blind. *HVAC and R Research, 7*(2), 169-184.

Echert, E. R. G., and Carlson, W. O. (1961). Natural convection in an air layer enclosed between two vertical plates with different temperatures. *International Journal of Heat and Mass Transfer*, 2, 106-120.

Elder, J. W. (1965). Laminar free convection in a vertical slot. *Journal of Fluid Mechanics* 23(1), 77-98.

Elder, J. W. (1965). Turbulent free convection in a vertical slot. *Journal of Fluid Mechanics* 23(1), 99-111.

ElSherbiny, S. M., Raithby, G. D., and Hollands, K. G. T. (1982). Heat transfer by natural convection across vertical and inclined air layers. *Journal of Heat Transfer, 104*(1), 96-102.

Fang, X. D. (2000). A study of the U-factor of the window with a high-reflectivity venetian blind. *Solar Energy, 68*(2), 207-214.

Finlayson, E. U., Arasteh, D. K., Huizenga, C., Rubin, M. D., and Reilly, M. S. (1993). Window 4.0: Documentation of Calculation Procedures. Energy and Environmental Division. Lawrence Berkeley Laboratory, Berkeley California.

Garnet, J.M., Fraser, R. A., Sullivan, H. F., Wright, J. L. (1995). Effect of internal venetian blinds on centre-glass U-values. *Conference Proceedings, Window Innovations '95*, 273-279.

Gill, A. E. (1966). The boundary-layer regime for convection in a rectangular cavity. *Journal of Fluid Mechanics*, 26(3), 515-536.

Huang, N. Y. T., Wright, J. L., Collins, M. R., and Erell, E. (2006). Thermal resistance of a window with an enclosed Venetian blind: Guarded heater plate measurements. *ASHRAE Transactions 112(2),* 13-21.

Jin, H. (2000). Flow visualization of natural convection in a vertical cavity. M.A.Sc. Thesis. University of Waterloo, Waterloo, Canada.

Kline, S.J. and McClintock, F.A., (1953). Describing Experimental Uncertainties in Single-Sample Experiments. Mechanical Engineering, Vol. 75, 3 -8.

Korpela, S. A., Lee, Y., and Drummond, J. E. (1982). Heat transfer through a double pane window. *Journal of Heat Transfer, Transactions ASME, 104*(3), 539-544.

Lai, B., (2004). An Interferometric Study of Free Convective Heat Transfer in a Double Glazed Window with a Between-Panes Venetian Blind. *MASc Thesis, Ryerson University.*

Lee, Y., and Korpela, S. A. (1983). Multicellular natural convection in a vertical slot. *Journal of Fluid Mechanics, 126*, 91-121.

Machin, A.D., (1997), An Experimental Study of Free Convective Heat Transfer from a Vertical Flat Plate in the Presence of Louvers. MESc Thesis, University of Western Ontario.

Machin, A. D., Naylor, D., Harrison, S. J., and Oosthuizen, P. H. (1998). Experimental study of free convection at an indoor glazing surface with a venetian blind. *HVAC and R Research, 4*(2), 153-166.

Naylor, D., Duarte, N., Petryk, J., and Machin, A. D. (2000). Flow- and temperature-field visualization of a window with a heated louvered blind. *Journal of Flow Visualization and Image Processing, 7*(3), 243-253.

Naylor, D., Shahid, H., Harrison, S. J., and Oosthuizen, P. H. (2006). A simplified method for modelling the effect of blinds on window thermal performance. *International Journal of Energy Research, 30*(7), 471-488.

Naylor, D., and Collins, M. (2005). Evaluation of an approximate method for predicting the U value of a window with a between-panes blind. *Numerical Heat Transfer; Part A: Applications, 47*(3), 233-250.

Naylor, D., Lai, B., and Avedissian, T. (2006). An Interferometric Study of Free Convection in an Enclosure with an Internal Blind. *13th International Heat Transfer Conference.*

Naylor, D., and Lai, B. Y. (2007). Experimental study of natural convection in a window with a between-panes venetian blind. *Experimental Heat Transfer, 20*(1), 1-17.

Naylor, D., Avedissian, T., Almeida, F. (2007). An Empirical Correlation for Free Convection in a Double Glazed Window with a Between-Panes Blind. *Proceedings of the 21st Canadian Congress of Applied Mechanics,* 326-327.

Oosthuizen, P.H., Sun, L., Harrison, S.J., Naylor, D., and Collins, M. (2005). The effect of coverings on heat transfer from a window to a room. *Heat Transfer Engineering, 26*(5), 47-65.

Phillips, J., Naylor, D., Harrison, S.J., and Oosthuizen, P.H. (1999). Free convection from a window glazing with a venetian blind: Numerical model development. *Transactions of the Canadian Society for Mechanical Engineering, 23*(1 B), 159-172.

Phillips, J., Oosthuizen, P. H., Naylor, D., and Harrison, S. J. (2001). Numerical study of convective and radiative heat transfer from a window glazing with a venetian blind. *HVAC and R Research, 7*(4), 383-402.

Rheault, S., and Bilgen, E. (1989). Heat transfer analysis in an automated Venetian blind window system. *Transactions of the ASME Journal of Solar Energy Engineering, 111*, 89-95.

Ramanathan, S., and Kumar, R. (1991). Correlations for natural convection between heated vertical plates. *Journal of Heat Transfer, 113*(1), 97-107.

Shahid, H., and Naylor, D. (2005). Energy performance assessment of a window with a horizontal venetian blind. *Energy and Buildings, 37*(8), 836-843.

Shewen, E., Hollands, K.G.T., and Raithby, G.D. (1996). Heat transfer by natural convection across a vertical air cavity of large aspect ratio. *Journal of Heat Transfer, 118*(4), 993-995.

Tarasuk, J.D. (1968). The Theory, Design and Operation of the University of Saskatchewan 8-Inch Mirror Mach-Zehnder Interferometer. Technical Report C-3, Mechanical Engineering Department, University of Saskatchewan.

Touloukian, Y.S. and Makita, T. (1975). Specific Heat: Nonmetallic Liquids and Gases. Thermophysical Properties of Matter, Vol 6, Thermophysical Properties Research Center (TPRC), Purdue University, Plenum Publishing Corp.

Von Bristram, P. (1995). The Design, Development and Preliminary Testing of the Ryerson Mach-Zehnder Interferometer. B.Eng. Thesis, Ryerson Polytechnic University.

Wright, J.L. (1992). Glazing System Thermal Analysis. CANMET. Advanced Glazing System Laboratory. VISION3. Minister of Supply and Services Canada. University of Waterloo.

Wright, J.L. (1996). Correlation to quantify convective heat transfer between vertical window glazings. *ASHRAE Transactions, 102*(1), 940-946.

Wright, J.L., Jin, H., Hollands, K. G. T., and Naylor, D. (2006). Flow visualization of natural convection in a tall, air-filled vertical cavity. *International Journal of Heat and Mass Transfer, 49*(5-6), 889-904.

Wright, J.L., Collins, M.R., Haung, N.Y.T, (2008). Thermal Resistance of a Window with an Enclosed Venetian Blind: Simplified Model, *ASHRAE Transactions 114(1),* 471-482.

Yahoda, D. S., and Wright, J. L. (2004). Heat transfer analysis of a between-panes venetian blind using effective longwave radiative properties. *ASHRAE Transactions 110(1),* 455-462.

Yahoda, D.S., and Wright, J.L. (2004). Methods for calculating the effective longwave radiative properties of a venetian blind layer. *ASHRAE Transactions 110(1),* 463-473.

"Maple 12.0". (2008), Waterloo Maple Inc.

"Matlab R2008a". (2008) The Mathworks Inc.